FABRICATION AND THERMAL ANALYSIS OF POLYIMIDE-BASED X-RAY MASKS AT THE SYNCHROTRON LABORATORY FOR MICRO AND NANO DEVICES, CANADIAN LIGHT SOURCE

A Thesis Submitted to the College of

Graduate Studies and Research

In Partial Fulfillment of the Requirements

For the Degree of Master of Science

In the Department of Electrical and Computer Engineering

University of Saskatchewan

Saskatoon

By

Chen Shen

© Copyright Chen Shen, August 2016. All rights reserved.

PERMISSION TO USE

In presenting this thesis/dissertation in partial fulfillment of the requirements for a Postgraduate degree from the University of Saskatchewan, I agree that the Libraries of this University may make it freely available for inspection. I further agree that permission for copying of this thesis/dissertation in any manner, in whole or in part, for scholarly purposes may be granted by the professor or professors who supervised my thesis/dissertation work or, in their absence, by the Head of the Department or the Dean of the College in which my thesis work was done. It is understood that any copying or publication or use of this thesis/dissertation or parts thereof for financial gain shall not be allowed without my written permission. It is also understood that due recognition shall be given to me and to the University of Saskatchewan in any scholarly use which may be made of any material in my thesis.

Requests for permission to copy or to make other uses of materials in this thesis/dissertation in whole or part should be addressed to:

Department of Electrical Engineering

57 Campus Drive

University of Saskatchewan

Saskatoon, SK S7N 5A9

ABSTRACT

In deep X-ray lithography (DXRL), synchrotron radiation (SR) is applied to transfer absorber patterns on an X-ray mask into the photoresist to fabricate high-aspect-ratio micro and nano scale structures (HARMNST). The Synchrotron Laboratory for Micro and Nano Devices (SyLMAND) at the Canadian Light Source (CLS) is a DXRL laboratory with continuous tuning capabilities for spectrum and power of the synchrotron beam.

X-ray mask fabrication is one of the most demanding sequences associated with the entire processing chain and has always constituted a bottleneck in the DXRL technology. In this thesis, X-ray masks based on polyimide membranes are studied, including the development of a fabrication sequence as well as theoretical and experimental analyses of limitations of pattern accuracy.

A 30 μm polyimide membrane was obtained by spin-coating photo-sensitive Fujifilm Durimide 7520® polyimide on a stainless steel substrate. Subsequently, a layer of $TiO_{1.9}$ was sputtered onto the membrane as the plating base for the absorbers. On the plating base, 100 μm of UV-sensitive negative-tone resist Futurrex NR26-25000P® were spin-coated and patterned by UV-lithography. The patterned photoresist served as a template, filling the voids with 80 μm nickel by electrodeposition. These metal structures served as the mask absorbers in the test masks. Two test masks were fabricated, one with complete coverage and one with a center block absorber layout. In the next processing step, the sacrificial steel substrate was locally opened by etching with ferric chloride solution to create an X-ray transparent exposure window. The mask was finally bonded to a mask frame for support and rigidity.

Polymer-based mask membranes are often avoided in DXRL because of large thermal distortions expected during X-ray exposure as a result of the low thermal conductivity. The power tuning capabilities at SyLMAND, however, allow the beam power to be adjusted and consequently limit thermal distortions. The heat load of the polyimide masks was analyzed by numerical analysis for the thermal and thermoelastic behavior of the test masks under synchrotron beam exposure. The beam power was calculated by the software LEX-D. ANSYS FLUENT® was used for the thermal analysis by computational fluid dynamics, and ANSYS Mechanical® for thermoelastic analysis using the finite element method. The thermal simulation results indicate that the main heat dissipation mechanism is from the mask absorbers by conduction across the rarefied helium gas in the proximity gap between the mask and its cooled surroundings. In DXRL, masks are vertically scanned through the synchrotron beam. Under the given conditions, this scanning speed of 50 mm/s was faster than the heat dissipation speed, such that a steep temperature gradient is observed between the exposed and unexposed mask areas as the beam scans across the test mask. The low thermal conductivity of the polyimide membrane can cause accumulation of heat in absorber structures such as the isolated center block absorber. At SyLMAND, an intensity chopper can

effectively tune the incident beam power, thereby reducing the heat load in the mask during exposure. The temperature rises during exposure scale almost linearly with the incident beam power. Final temperatures of close to 39°C were obtained for both test masks at an incident beam power of about 14.5 W.

To verify the numerical analysis, the actual temperature rises in the test masks during exposure were experimentally measured. Five thermocouples were bonded to the surface of the absorber to measure the local temperature. By comparing the recorded temperatures at different beam power settings, the temperature rises in the test masks were found to be proportional to the beam power, which verifies the numerical findings. Furthermore, the shape and size of the absorbers have a significant impact on the physics of the thermoelastic behavior. However, the increased power absorption associated with larger absorbers almost completely compensate the increased heat transfer capability along the higher conductivity mask absorbers in the examined cases. The experiments verified the simulations to a large extent. Deviations typically amount to 5°C at an overall temperature of approximately 40°C, which is mainly attributed to the size of the proximity gap varying in reality, and therefore differing from the model assumption of a constant gap.

Finally, the thermal and thermoelastic behavior of the test masks was evaluated by an extended numerical analysis model for different typical exposure scenarios used for the DXRL exposure of 250 µm and 500 µm PMMA resist coated onto a silicon wafer substrate. In these simulations, the resist and substrate were also modeled. For a 25% duty cycle chopper setting, and spectral tuning as required for exposure, about 14 W to 20 W of incident beam power gets absorbed. A maximum mask temperature of 25.4°C is observed for 250 µm PMMA, and 31.0°C for 500 µm PMMA. While the resist deforms on the nanometer level, mask deformations in the lateral plane amount to approximately 2.3 µm for 250 µm PMMA, and to approximately 4 µm for 500 µm PMMA. These are worst-case values without further beam power reduction, and integrated over 6 cm large absorbers. Local deformations would be significantly lower. Such deformations are therefore deemed acceptable. The results prove that polyimide masks can be applied with acceptable thermal deformations under the conditions found at SyLMAND.

ACKNOWLEDGEMENTS

Foremost, I would like to express my sincere gratitude to my advisor Dr. Sven Achenbach for the continuous support of my Master's degree and research, for his patience, motivation, enthusiasm, and immense knowledge. His guidance helped me in all the time of research and writing of this thesis. I could not have imagined having a better advisor and mentor for my Master's degree study.

I would like to take this opportunity to express my gratitude to my committee members Dr. David Sumner, Dr. Robert Johanson, and Dr. Ann Dinh for their time and consideration in reviewing my thesis.

I would like to thank Garth Wells and Banafsheh Moazed at the Synchrotron Laboratory for Micro and Nano Devices (SyLMAND), and Brian Yates of the Canadian Light Source. This project could not have been completed without their sincere help with processing, fabrication, inspection, and testing capabilities.

In addition, I would like to thank Stewart Griffiths, Sandia National Labs, USA, for leading the development of and granting access to LEX-D, and Pascal Meyer, Institute of Microstructure Technology, Karlsruhe Institute of Technology, Germany, for the development of and granting access to DoseSim.

I acknowledge the financial assistance for this project provided by the Department of Electrical and Computer Engineering, as well as Dr. Sven Achenbach.

Finally, I would like to thank my parents, Shen Yunong and Zhang Weimin, for their love, patience and support throughout the time I studied at the U of S. This thesis is dedicated to them.

TABLE OF CONTENTS

Page

PERMISSION TO USE ... **i**
ABSTRACT ... **ii**
ACKNOWLEDGEMENTS ... **iv**
TABLE OF CONTENTS ... **v**
LIST OF TABLES ... **ix**
LIST OF FIGURES ... **x**
LIST OF ABBREVIATIONS ... **xv**
CHAPTER 1: INTRODUCTION ... **1**

1.1 Overview of X-Ray Lithography Technology ... 1
1.2 Review of X-Ray Lithography Mask Fabrication ... 4
1.3 Review of Thermal and Mechanical Analyses of X-ray Exposure ... 10
1.4 Experimental Setup in the Synchrotron Laboratory for Micro and Nano Devices (SyLMAND) ... 11
1.5 Motivation and Research Objectives ... 16
1.6 Thesis Organization ... 17

CHAPTER 2: POLYIMIDE MATERIALS SELECTION AND FABRICATION PROCESS DEVELOPMENT OF TEST MASKS ... **19**

2.1. Review of Material Properties of Polyimide as a Potential Mask Membrane Material ... 19

2.1.1 Thermal and Mechanical Properties ... 19
2.1.2 Radiation Stability ... 20

2.2 Review of Polyimide Mask Membranes used in X-ray Lithography ... 20
2.3 Process Development for an Integrated Polyimide Membrane ... 21

2.3.1 Fabrication Concept Alternatives ... 22
2.3.2 Polyimide Material Selection and Membrane Fabrication ... 23
2.3.3 Selection of the Sacrificial Substrate and Development of the Release Process ... 24

2.4 Layout of the Test Masks ... 25
2.5 Fabrication of the Test Masks ... 26

2.5.1 Processing of the Polyimide Membrane ... 26
2.5.2 Patterning of the Mask Absorber Templates ... 28
2.5.3 Electroplating of the Mask Absorber Structures ... 28

2.5.4 Etching of the Exposure Window and Gluing of the Mask Frame 30
2.5.5 Integration of the Individual Fabrication Steps into a Process Sequence 32
2.6 Chapter Summary 33
CHAPTER 3: THERMAL AND THERMOELASTIC ANALYSIS OF THE POLYIMIDE MEMBRANE MASK 35
3.1 Modeling of the X-ray Exposure under Synchrotron Radiation 35
3.1.1 Simplifications and Assumptions in the Models 35
3.1.2 Governing Equations and Boundary Conditions 39
3.2 Simulations 43
3.2.1 Meshing of the Model 43
3.2.2 Thermal Simulations 45
3.2.3 Thermoelastic Simulations 50
3.3 Discussion 55
3.4 Chapter Summary 60
CHAPTER 4: THERMAL MEASUREMENTS OF POLYIMIDE MEMBRANE MASKS AND VERIFICATION OF THERMAL SIMULATIONS 62
4.1 Experimental Design and Setup 62
4.1.1 Properties of the Synchrotron Beam 62
4.1.2 Exposure Parameters 63
4.1.3 Experimental Setup with Thermocouples 63
4.2 Experimental Results 65
4.2.1 Test Results for the Complete Coverage Mask 66
4.2.2 Test Results for the Center Block Mask 67
4.3 Interpolation of the Temperature Rise as a Function of the Incident Beam Power 68
4.4 Discussion 69
4.5 Chapter Summary 72
CHAPTER 5: SIMULATION OF DXRL EXPOSURES 73
5.1 Simulation for the Complete Coverage Test Mask under DXRL Exposure 74
5.2 Simulation for the Center Block Test Mask under DXRL Exposure 75

5.3 Thermoelastic Simulation for the Center Block Mask and PMMA Resist 79

5.3.1 Exposure of 250 µm PMMA 81

5.3.2 Exposure of 500 µm PMMA 83

5.3.3 Summary of Simmulation Results 85

5.4 Discussion 85

5.5 Chapter Summary 86

CHAPTER 6: SUMMARY AND CONCLUSION 88

6.1 Summary and Conclusion 88

6.2 Future Work 90

APPENDIX A: TECHNICAL INFORMATION FOR POLYIMIDE MATERIALS 91

A.1 Polyimide Solution P84® 91

A.2 Photoresist Durimide 7520® 91

APPENDIX B: SURFACE ROUGHNESS MEASUREMENTS FOR POLYIMIDE MASK FABRICATION 93

APPENDIX C: CALCULATIONS OF 100 MBAR HELIUM GAS PROPERTIES AND DIMENSIONLESS NUMBERS 102

C.1 Calculation of the Knudsen Number K_n of 100 mbar Helium at 18°C : 102

C.2 Calculation of the 100 mbar Helium Density ρ at 18°C : 103

C.3 Calculation of the Dynamic Viscosity μ and Kinematic Viscosity v of 100 mbar Helium at 18°C : 103

C.4 Calculation of the Thermal Conductivity k of 100 mbar Helium Gas at 18°C : 103

C.5 Calculation of the Prandtl Number Pr and the Thermal Diffusivity α of 100 mbar Helium at 18°C : 103

C.6 Calculation of the Reynolds Number Re_D and the Rayleigh Number Ra_D of 100 mbar Helium at 18°C : 103

C.7 Determination of the Time Step τ for Transient Thermal Simulation: 104

C.8 Determination of the Heat Transfer Coefficient h of the Polyimide Membrane: 104

APPENDIX D: LEX-D CALCULATION FOR THE POWER ABSORPTION IN DIFFERENT MATERIAL LAYERS 106

APPENDIX E: USER DEFINED FUNCTIONS (UDF) IN THE ANSYS FLUENT SIMULATION 108

E.1 UDF for the Thermal Simulation in Chapter 3: 108
E.2 UDF for the DXRL Exposure Thermal Simulation in Chapter 5: 109

APPENDIX F: TEMPERATURE MEASUREMENTS FOR THE TEST MASKS 111

F.1 Measurements for the Complete Coverage Test Mask 111
F.2 Measurements for the Center Block Test Mask 114

BIBLIOGRAPHY 118

LIST OF TABLES

Table Page

Table 1.1: The characteristics of X-ray mask membrane materials ... 7

Table 2.1: Mechanical properties and etching features of potential substrates ... 24

Table 2.2: Titanium sputtering parameters for thin film coating of the plating base on polyimide. ... 27

Table 3.1: Overview of mesh sizes and properties. ... 44

Table 3.2: Thermal and mechanical material properties used in the simulations ... 45

Table 3.3: Maximum temperature at different thermocouple positions from thermal simulation ... 50

Table 4.1: Exposure parameters for the complete coverage mask ... 66

Table 4.2: Maximum temperatures measured by thermocouples on the complete coverage mask ... 66

Table 4.3: Exposure parameters for the center block mask ... 67

Table 4.4: Maximum temperatures measured by thermocouples on the center block mask. ... 67

Table 5.1: Thermal properties of PMMA X-ray resist and silicon wafer ... 74

Table 5.2: Synchrotron beam parameters for DXRL exposures ... 77

Table 5.3: Mechanical properties of PMMA and silicon ... 80

Table 5.4: Results of the thermoelastic simulations for DXRL exposure ... 85

Table A.1: Mechanical properties of P84® compiled from vendor information ... 91

Table A.2: Mixture of P84® and NEP ... 91

Table A.3: Mechanical properties of Durimide 7520® ... 91

Table A.4: Processing parameters of Durimide 7520® ... 92

Table B.1: Measured surface roughness at selected mask fabrication steps ... 94

Table C.1: Modelling parameters for helium gas calculations ... 102

Table D.1: LEX-D results for power absorption in different material layers ... 107

LIST OF FIGURES

Figure Page

Figure 1.1: The LIGA process 1

Figure 1.2: Artistic view of DXRL exposure 2

Figure 1.3: Lithographic patterning of positive and negative tone resists 2

Figure 1.4: Local exposure dose values relevant for determining the optimum exposure conditions 3

Figure 1.5: Absorption of synchrotron radiation in the substrate leading to isotropic emission of secondary electrons 4

Figure 1.6: X-ray attenuation length [µm] of different mask absorber materials for photon energies from 1 to 15 keV 5

Figure 1.7: Spectral transmission of different mask membrane materials at the thicknesses from Table 1.1. 6

Figure 1.8: Fluorescence radiation from the X-ray mask membrane 8

Figure 1.9: Thermal expansion during X-ray exposure 9

Figure 1.10: Typical fabrication sequences for X-ray masks 10

Figure 1.11: Schematic of the SyLMAND beamline 12

Figure 1.12: Schematic of the intensity chopper disk 13

Figure 1.13: SyLMAND spectral power 14

Figure 1.14: SyLMAND beam power impinging onto the sample 14

Figure 1.15: SyLMAND scanner stage with assembly of mask and mask holder as well as the substrate holder in the opened position. 15

Figure 1.16: Cooling plate of the SyLMAND mask holder 16

Figure 2.1: Artistic view of molecule chain disorientation due to increased film thickness. 19

Figure 2.2: Fabrication process for the polyimide X-ray mask by Optnics Precision 20

Figure 2.3: Micrographs of a test structure with 10 µm nominal line width. 21

Figure 2.4: Optical micrograph of a typical P84® polyimide membrane surface after mixing, spin-coating and curing 24

Figure 2.5: Layout of the center block test mask 25

Figure 2.6: Optical micrograph of a Durimide 7520® polyimide membrane........ 27

Figure 2.7: Scanning Electron Micrographs of the sputtered titanium layer on polyimide 28

Figure 2.8: Setup of nickel electroplating 30

Figure 2.9: Image of a processed mask. 31

Figure 2.10: Complete coverage test mask seen from the front side 31

Figure 2.11: Center block test mask seen from the front side. 32

Figure 2.12: Fabrication sequence developed for polyimide X-ray masks at SyLMAND. 33

Figure 3.1: Schematic of the simplified model for thermal simulations 36

Figure 3.2: X-ray transmission of the X-ray mask components from 1 to 15 keV 38

Figure 3.3: Schematic of the simplified mask model for thermoelastic simulations 38

Figure 3.4: Schematic of the DXRL exposure model used in the simulation of the complete coverage mask. 39

Figure 3.5: Thermal balance of the model 40

Figure 3.6: Components of stress in three dimensions. 41

Figure 3.7: Left: FEM mesh of the complete coverage mask for the thermoelastic simulation; Right: details of the elements used in the mesh. 44

Figure 3.8: Simulated temperatures with respect to flow time at the locations where the five thermocouples are placed in the experiments for the complete coverage mask. 46

Figure 3.9: Simulated temperature distribution when the beam is at the location of the top thermocouple (#2) and the temperature reaches its highest values in that location. Simulation for the complete coverage mask. 47

Figure 3.10: Simulated temperature distribution when the beam is at the location of the center thermocouple (#5) and the temperature reaches its highest values in that location. Simulation for the complete coverage mask. 47

Figure 3.11: Simulated temperatures with respect to flow time at the locations where the five thermocouples are placed in the experiments for the center block mask 48

Figure 3.12: Simulated temperature distribution when the beam is at the location of the top thermocouple (#2) and the temperature reaches its highest values in that location. Simulation for the center block mask. 49

Figure 3.13: Simulated temperature distribution when the beam is at the location of the center thermocouple (#5) and the temperature reaches its highest values in that location. Simulation for the center block mask. 49

Figure 3.14: Simulated total (3-dimensional) deformations (in micrometers) for the complete coverage mask 50

Figure 3.15: Simulated deformations (in micrometers) in the lateral plane along the x-axis (orthogonal to the incident synchrotron beam) for the complete coverage mask 51

Figure 3.16: Simulated deformations (in micrometers) in the lateral plane along the y-axis (orthogonal to the incident synchrotron beam) for the complete coverage mask 51

Figure 3.17: Simulated deformations (in micrometers) along the z-axis (along the beam direction, orthogonal to the lateral plane) for the complete coverage mask 52

Figure 3.18: Simulated equivalent stress distributions (in MPa) for the complete coverage mask 52

Figure 3.19: Simulated total (3-dimensional) deformations distributions (in micrometers) for the center block mask 53

Figure 3.20: Simulated deformations (in micrometers) along the x-axis (orthogonal to the incident synchrotron beam) for the center block mask 53

Figure 3.21: Simulated deformations (in micrometers) along the y-axis (orthogonal to the incident synchrotron beam) for the center block mask 54

Figure 3.22: Simulated deformations (in micrometers) along the z-axis (along the beam direction, orthogonal to the lateral plane) for the center block mask 54

Figure 3.23: Simulated equivalent stress distributions (in MPa) for the center block mask 55

Figure 3.24: 3D schematic of the center block absorber deformation when the beam is at the location of the center thermocouple (#5) (deformation scaled by 200). 58

Figure 3.25: Simulated temperature distribution after 19.0 seconds when the beam is at the location of the center thermocouple (#5) and the temperature reaches its highest values in that location. Simulation for the complete coverage mask, exposure without intensity chopper implementation. 59

Figure 3.26: Simulated deformations (in micrometers) for the complete coverage mask, exposure without intensity chopper implementation 60

Figure 4.1: Vertical beam profile scanned with the fly-wire photocurrent measurement system at the mirror entrance 62

Figure 4.2: Schematics of the positioning of the five thermocouples on the test masks 64

Figure 4.3: Experimental setup of the complete coverage mask, mask holder, scanner adapter, and five thermocouples. 64

Figure 4.4: Experimental setup of the center block mask, mask holder, scanner adapter, and 5 thermocouples. 65

Figure 4.5: Maximum temperatures at the center thermocouple (#5) measured for various computed incident beam powers with the complete coverage mask 68

Figure 4.6: Maximum temperatures at the center thermocouple (#5) measured for various computed incident beam powers with the center block mask 69

Figure 4.7: Simulated (solid line) and measured (dotted line) temperature with respect to time at the location of the center thermocouple (#5) for the complete coverage mask. 70

Figure 4.8: Simulated (solid line) and measured (dotted line) temperature with respect to time at the location of the center thermocouple (#5) for the center block mask. 70

Figure 4.9: Schematic of the tilted substrate holder during the measurements 71

Figure 5.1: Extended DXRL exposure simulation model with PMMA-wafer assembly: cross-sectional view of the synchrotron beam impinging onto the modeled layers. 73

Figure 5.2: Simulated temperatures with respect to flow time at the location of the center thermocouple (#5) for the complete coverage mask using the intensity chopper with 25% open duty cycle 74

Figure 5.3: Simulated mask temperature distribution when the beam is at the location of the center thermocouple (#5) and the temperature reaches its highest values in that location. Simulation for the nickel absorber in the complete coverage mask. 75

Figure 5.4: Simulated resist temperature distribution when the beam is at the location of the center thermocouple (#5) and the temperature reaches its highest values in that location. Simulation for the PMMA resist on the silicon wafer behind the complete coverage mask. 75

Figure 5.5: Beam power density distribution in the various layers of the extended DXRL exposure model for the center block mask 76

Figure 5.6: Simulated temperature distribution when the beam is at the location of the center thermocouple (#5) and the temperature reaches its highest value in that location. Simulation for the center block mask in front of 250 µm PMMA. 78

Figure 5.7: Simulated resist temperature distribution when the beam is at the location of the center thermocouple (#5) and the temperature reaches its highest value in that location. Simulation for 250 µm PMMA resist on the silicon wafer behind the center block mask. 78

Figure 5.8: Simulated temperature distribution when the beam is at the location of the center thermocouple (#5) and the temperature reaches its highest value in that location. Simulation for the center block mask in front of 500 µm PMMA. 79

Figure 5.9: Simulated resist temperature distribution when the beam is at the location of the center thermocouple (#5) and the temperature reaches its highest value in that location. Simulation for 500 µm PMMA resist on the silicon wafer behind the center block mask. 79

Figure 5.10: Schematic of the PMMA-wafer assembly model 80

Figure 5.11: Simulated deformations (in micrometers) for the center block mask in front of 250 µm PMMA 81

Figure 5.12: Simulated deformations (in micrometers) for the 250 µm thick PMMA layer behind the center block mask 82

Figure 5.13: Simulated deformations (in micrometers) for the center block mask in front of 500 µm PMMA. 83

Figure 5.14: Simulated deformations (in micrometers) for the 500 µm thick PMMA layer behind the center block mask 84

Figure A.1: Relationship between spin speed and cured film thickness for Durimide 7520®. 92

Figure B.1: Positions of surface roughness measurements for the titanium layer. 93

LIST OF ABBREVIATIONS

CLS	Canadian Light Source
DMSO	Dimethyl Sulfoxide
DXRL	Deep X-Ray Lithography
LIGA	German acronym for lithografie, galvanoformung, and abformung
MEMS	Microelectromechanical Systems
NEP	N-ethyl-pyrrolidone
PMMA	Polymethyl Methacrylate
PVD	Physical Vapor Deposition
SEM	Scanning Electron Microscope
SR	Synchrotron Radiation
SyLMAND	Synchrotron Laboratory for Micro and Nano Devices
TMAH	Tetramethyl Ammonium Hydroxide
XRL	X-Ray Lithography

CHAPTER 1

INTRODUCTION

1.1 Overview of X-Ray Lithography Technology

X-ray lithography (XRL) has been developed since the 1970s with further developments still being made today. It utilizes high energy photons within the spectrum of X-rays to transfer absorber patterns on an X-ray mask into a photosensitive layer coated onto a substrate [1][2]. In the 1980s, deep X-ray lithography (DXRL) using hard X-rays of 2 to 15 keV became a vital step in the LIGA process. LIGA is a German acronym for lithography, electroplating, and replication. The technology was developed by Forschungszentrum Karlsruhe, Germany (FZK/IMT) [3][4]. Combined with subsequent electroplating and molding steps, mass production of microstructures becomes possible (see Figure 1.1).

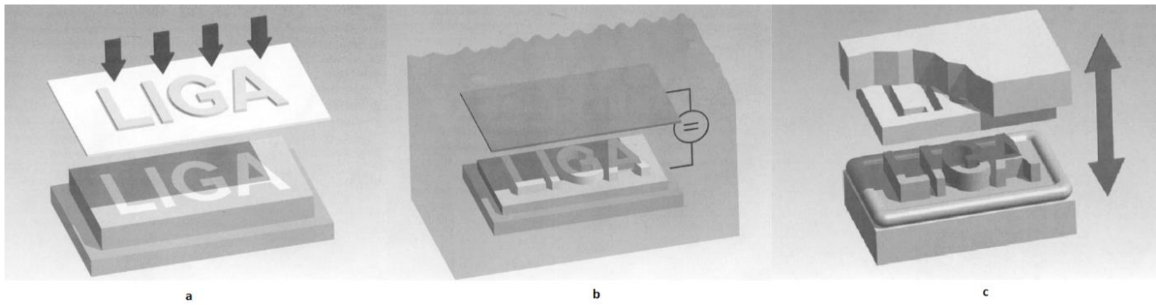

Figure 1.1: The LIGA process: (a) *Lithography:* X-ray lithography using synchrotron radiation to expose a thick resist layer through an X-ray mask; (b) *Electroplating:* Electrodeposition of metal in the resist template fabricated in step (a); (c) *Replication:* Molding of a polymer using the metallic molding tool fabricated in step (b). [5]

LIGA technology enables fabrication of high aspect ratio micro structures (the ratio between height and width of the structures, up to some hundreds) with high lateral accuracy, and optically smooth, vertical sidewalls [6][7]. The exposure process typically involves synchrotron radiation (SR) [8]. Synchrotron radiation is produced when electrons orbit almost at the speed of light, e.g. in an electron storage ring. The centripetal acceleration of the charged particles in bend magnets leads to the emission of electromagnetic radiation. Due to relativistic effects, the radiation is highly collimated as it proceeds down the X-ray beamline. On its way to the sample, the beam passes the X-ray mask. Where the X-rays impinge onto mask absorbers made of high atomic number Z elements, such as gold, they get completely absorbed. In mask areas without absorber patterning, the X-rays pass the mask membrane and a small proximity gap to impinge onto the photoresist on a substrate, causing local photo-chemical reactions. Thus, an image of the lateral mask absorber pattern is formed by shadow projection. The chemical properties of the exposed photoresist get locally modified, which turns the exposed photoresist to be selectively soluble or insoluble,

depending on the resist type, in a subsequent wet-chemical development step. The synchrotron beam usually covers the entire width of the sample to be exposed. In the vertical direction, the collimation limits the exposure height to a few millimeters. Homogeneous exposure of several centimeter large samples can only be achieved if the stack of mask and sample is vertically oscillated through the synchrotron beam. This task is accomplished in an X-ray scanner, which precisely controls the motion, ensuring constant mechanical mounting and constant velocities during each stroke (see Figure 1.2).

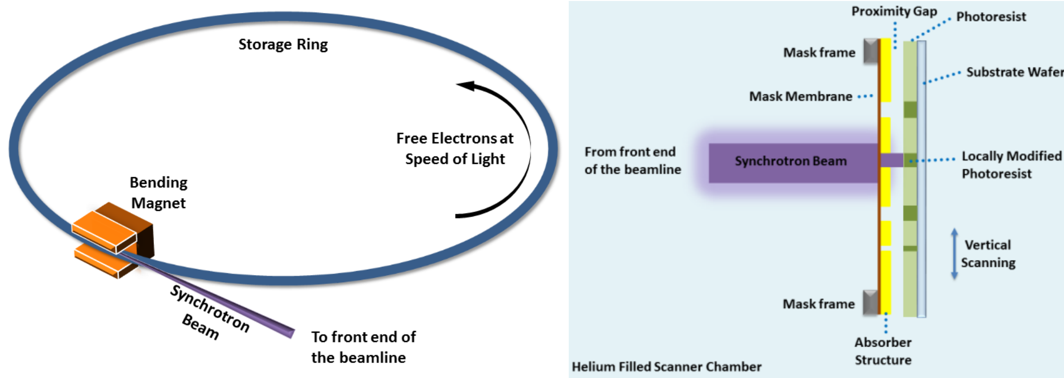

Figure 1.2: Artistic view of DXRL exposure: Left: Bend magnet accelerating the electron trajectory, leading to tangential emission of photons (synchrotron radiation); Right: Side view inside the vacuum chamber of an X-ray scanner for DXRL. The X-ray mask (consisting of mask frame, mask membrane, and mask absorber structures) and the sample (consisting of photoresist and silicon wafer) is vertically oscillated (scanned) through the incident synchrotron beam (Dark areas of the photoresist represent exposed resist).

Photoresists can be divided into two types: positive tone and negative tone resists. For positive tone resists, exposed regions will get soluble in the developer. For negative tone resists, exposed regions become insoluble in the developer (see Figure 1.3). The most commonly used positive tone resist in DXRL is Polymethyl Methacrylate (PMMA, $[C_5H_8O_2]_n$) [9]. A typical negative tone resist is SU-8 which was developed by IBM in the 1990s [10].

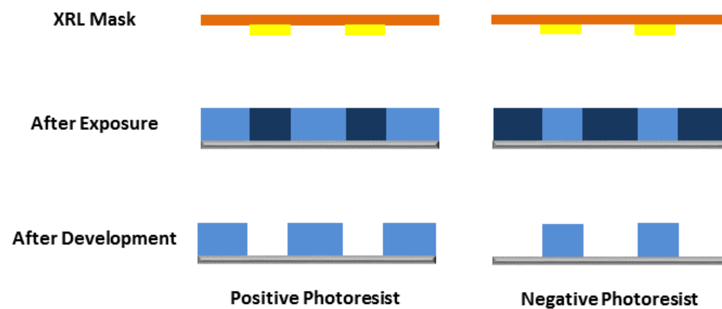

Figure 1.3: Lithographic patterning of positive and negative tone resists (Dark areas of the photoresist represent exposed resist).

A vital parameter in lithographic exposure is the power density of the radiation absorbed in the resist, referred to as the exposure dose. In DXRL, the exposure dose is a volumetric quantity. It is impacted by the radiation spectrum as well as the absorber and resist material properties and layer thicknesses. Three target dose values are typically defined: the dose deposited at the top of the exposed photoresist (D_{top}); the dose deposited at the bottom of the exposed photoresist (D_{bottom}); and the dose unintentionally deposited at the top of the nominally unexposed photoresist ($D_{unexposed}$) due to finite mask absorber contrast and secondary effects [11][12] (see Figure 1.4). For positive-tone resist, the dose deposited at the top of the exposed resist, D_{top}, may not exceed an upper limit since the photoresist would massively foam if too much energy was absorbed. This could damage the adjacent unexposed resist areas or even the mask. The dose deposited at the bottom of the exposed resist, D_{bottom}, has a minimum threshold to ensure residual-free development at a chosen overall development time [13]. These restrictions result in a top-to-bottom dose ratio for the exposed resist with an optimum value for different resist types and layer thickness. To meet these dose requirements, the spectral distribution of the synchrotron beam and the exposure time must be adjusted for each individual exposure.

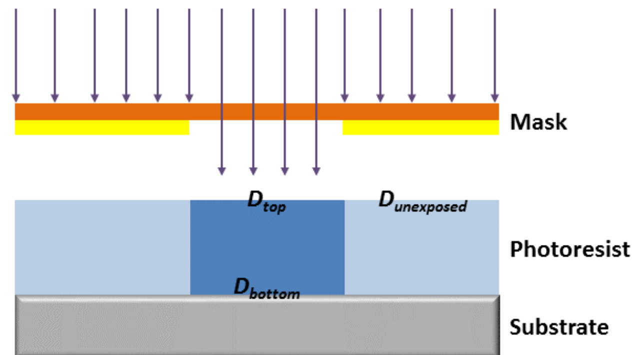

Figure 1.4: Local exposure dose values relevant for determining the optimum exposure conditions. (Dark areas of the photoresist represent exposed resist).[14]

For the positive tone photoresist PMMA, the maximum allowed dose is 20 kJ/cm^3, while typically a safer dose value of 12 kJ/cm^3 is chosen for the top of the exposed resist. The minimum exposure dose deposited at the bottom of the exposed PMMA is usually assumed to be about 3 kJ/cm^3. The dose deposited in the unexposed PMMA under the absorber structures must remain less than 0.1 kJ/cm^3 [15]. For the negative photoresist SU-8, the required dose deposition is only 50-100 J/cm^3 [16].

As previously mentioned, these dose requirements are met by spectral adjustment. Both, low and high energy photons may need to be filtered from the incident beam spectrum. The soft spectral contributions can be reduced by low-atomic number pre-absorbers, such as beamline vacuum windows or X-ray filters to be introduced into the beamline. In both cases, low energy contributions of the spectrum are filtered most,

delivering a spectrum with a higher photon energy and finally a decreased top-to-bottom dose ratio. High energy photons can be selectively filtered using grazing incidence X-ray reflecting mirrors or a central beam-stop. These techniques result in a softer remaining spectrum increasing the top-to-bottom dose ratio in a given resist [17][18]. When dose requirements previously stated are met, softer spectra are also preferred to avoid excess secondary radiation from the sample substrate: high energy photons are preferably absorbed in higher atomic number substrates, leading to the isotropic emission of secondary electrons. These will unintentionally expose the resist at the interface to the substrate, reducing the resist adhesion after development [19] (see Figure 1.5).

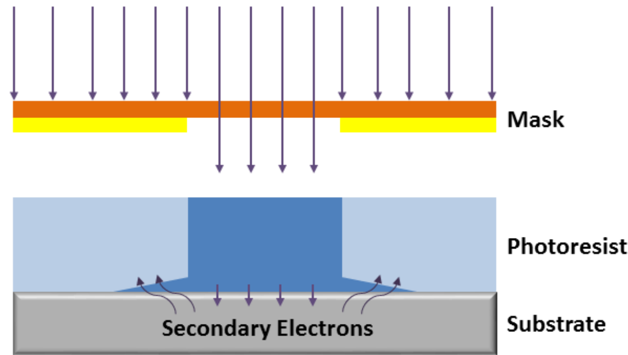

Figure 1.5: Absorption of synchrotron radiation in the substrate leading to isotropic emission of secondary electrons. This process deposits energy in the resist-substrate-interface, reducing the adhesion after development. (Dark areas of the photoresist represent exposed resist).

1.2 Review of X-Ray Lithography Mask Fabrication

X-ray masks are a critical and indispensable component of the DXRL process. X-ray masks consist of three basic components: the absorber structures representing the designed two-dimensional lateral layout; the mask membrane that supports the absorber structures and provides efficient cooling from absorbers to the frame; and the mask frame to mount the mask into the scanner and to provide thermal contact from the mask to the cooled mask support structure in the scanner.

The absorber structures are made of a high atomic number material, typically gold. The absorber thickness depends on the spectral distribution and the involved materials and their respective thickness [20][21]. A typical gold absorber thickness in DXRL is approximately 20 µm. Alternative materials for absorbers are nickel, copper, lead, and tungsten. The attenuation length of a material is used to define the effectiveness of the absorption of radiation. Penetrating one absorption length into a given material, the radiation retains $1/e$ of the original intensity (see Figure 1.6).

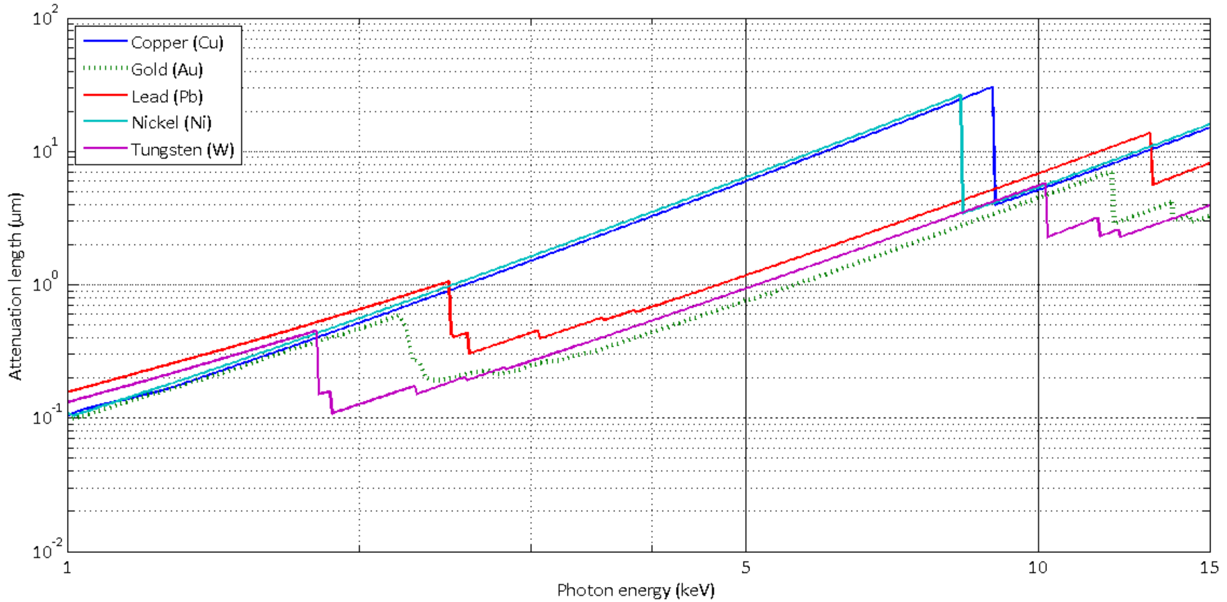

Figure 1.6: X-ray attenuation length [μm] of different mask absorber materials for photon energies from 1 to 15 keV. [22]

The mask membrane supports the absorber structures, defining their exact position. It also dissipates heat in the absorbers to the supporting frame. The membrane should meet the following criteria: 1) lowest possible X-ray absorption to allow for good transmission (ratio of transmitted to incident power) of X-rays to the resist to be exposed and a good contrast when compared to the transmission through absorbers; 2) highest possible mechanical strength to safely support the mask absorbers even under thermal stress and to allow for larger mask formats; 3) sufficient electrical conductivity to allow for electroplating of the metal absorbers during the mask fabrication process; 4) good adhesion of the mask absorbers to avoid delamination during use; 5) constant thickness to avoid uneven absorption in the membrane (e.g., absence of pinholes, little or no wedge-error in membrane thickness, limited roughness); 6) good availability and economic affordability; 7) non-toxic materials to allow for a broad fabrication process selection; 8) sufficient stability when exposed to X-rays; and 9) optical transparency to allow for aligned exposure.

A variety of materials have been explored and used for mask membrane applications, such as silicon nitride, silicon carbide, silicon, beryllium, graphite, glass, titanium, and polyimide. Some selected characteristics of the most frequently used materials are compiled in Table 1.1. It shows that none of the materials is a perfect mask membrane material. While beryllium, for instance, has outstanding thermal properties and is sufficiently X-ray transparent to allow for mechanically stable membrane thicknesses, it is toxic, hard to machine to the required specifications, optically not transparent, and both expensive as well as with limited availability from only one vendor world-wide. Polyimide, on the other hand, is optically transparent, cheap, non-toxic, and reasonably stable as far as mechanical properties are concerned, but only

features limited stability against X-rays, and has very poor thermal properties. The spectral transparencies of the mask membrane materials mentioned in Table 1.1 are presented in Figure 1.7. The transmission is defined as the ratio of the transmitted power to the incident power. The values are calculated based on the membrane thickness from Table 1.1.

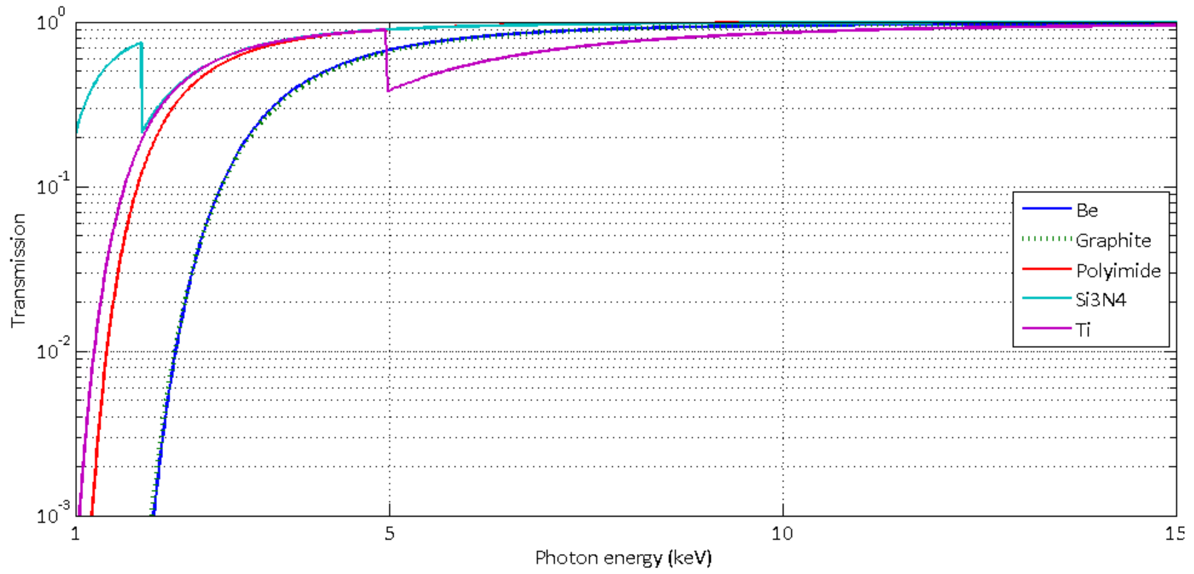

Figure 1.7: Spectral transmission of different mask membrane materials at the thicknesses from Table 1.1. [22]

Table 1.1: The characteristics of X-ray mask membrane materials [14][23]

Material	Density (g/cm^3)	Young's Modulus (GPa)	Type of Membrane	Typical Substrate Thickness (µm)	Thermal Conductivity (W/m/K)	Thermal Expansion Coefficient (10^{-6}/K)	Typical Fabrication Technique	Cost	Surface Roughness (nm)
Beryllium	1.85	300	Self-supported	>250	200	12.3	Machining	High	500
Graphite	1.7-1.8	N/A	Self-supported	>100	95	8.1	Machining	Low	<1000
Silicon Nitride	2.4	160-390	Suspended	1	16-33	0.8-2.7	CVD	High	N/A
Titanium	4.5	120	Suspended	2.8	20-30	9	PVD	High	N/A
Polyimide	1.2	>3	Suspended	50	0.12	55	Spin coating	Low	N/A

Selected mask membrane materials have further disadvantages beyond those apparent in Table 1.1, causing secondary effects [19]. First, some mask membrane materials will, during exposure to high energy photons as found in synchrotron radiation, emit secondary fluorescence radiation. This fluorescence radiation has energies characteristic of the membrane material and is emitted isotropically (i.e. without preferred direction), leading to an extra dose deposition at the top corners of the nominally unexposed resist areas. After development, bevelled edges can be observed (see Figure 1.8). For example, titanium has the K-shell absorption edge at 4.97 keV, which is within the synchrotron spectrum used for DXRL exposure [24]. Such secondary fluorescence can penetrate the resist up to several hundred micrometers deep. To reduce the impact of the fluorescence radiation, low atomic number X-ray filters such as polyimide foils can be inserted between the mask and substrate during exposure. A more fundamental approach is changing the membrane material: lower atomic number materials, such as beryllium, do not exhibit noticeable fluorescence.

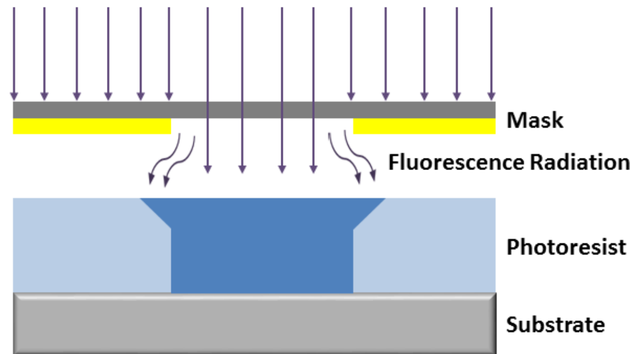

Figure 1.8: Fluorescence radiation from the X-ray mask membrane. (Dark areas of the photoresist represent exposed resist).

A major concern for selecting mask membrane materials is the thermal conductivity: the beam power absorbed in the X-ray mask is primarily dissipated as heat, which can lead to increased temperatures in mask and sample, resulting in non-uniform thermal expansion and ultimately in thermal deformations of the mask and sample (see Figure 1.9) [19]. To control the temperature rise in the X-ray mask, it is critical to provide sufficient cooling through the mask frame to the cooled scanner adapter, and to allow good heat transfer from the mask absorbers to the mask frame by using thermally well conducting membranes. Where this is not possible, the incident beam power must be reduced to limit the temperature rise. This power reduction can be achieved by decreasing the electron current in the storage ring; by using an intensity chopper; or by insertion of pre-absorber in front of the mask [19]. These thermal effects will be further discussed in Section 1.5.

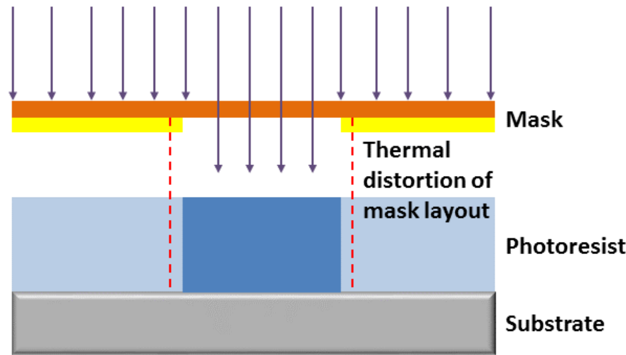

Figure 1.9: Thermal expansion during X-ray exposure: deformations of the mask absorbers from the ideal dimensions (broken red lines) and ultimately to reduced accuracy of the exposed resist area (dark area).

During fabrication, the mask absorbers are generated by filling the voids in a polymer template, using an electroplating process. This process requires an electrically conductive layer. If the mask membrane is not conductive, an intermediate thin film plating base is required. A typical plating base material in DXRL is gold, while another is TiO_x. The latter has X-ray optical advantages over gold, but requires to avoid the formation of the natural oxide TiO_2 which is a dielectric. A complex compound must be formed by partial oxidization of the titanium layer [25]. This ensures high electrical conductivity and a passivated surface to protect from further oxidization. Furthermore, the slightly rough surface structure of the TiO_x promotes the adhesion between mask membrane and absorber structures by mechanical interlocking.

The mask frame of an X-ray mask supports the mask membrane, facilitates mounting of the mask in the scanner, and provides efficient cooling of the entire mask when a good contact is established to the cooled scanner. Mask frames are available in a variety of formats. One of them is laid out for a round mask of 4-inch diameter. A manufacturing standard for this format was developed by APRA-NIST in the 1990s [26][27]. It offers a 4” outer diameter (101.6 mm) and an exposable net diameter of 83 mm as the exposure window. The material of this mask frame is an aluminum alloy or stainless steel.

Besides the materials for the three main components, and the involved dimensions, micro patterning of the mask absorbers is also important. The sidewalls of the absorbers must be vertical and straight to provide a sharp contrast between transparent and opaque mask areas [28]. Typical absorber thicknesses of approximately 20 µm gold are sufficient in many cases. Since XRL is based on shadow projection, the lateral absorber dimensions are identical with the exposed sample. Mask absorbers must therefore have vertical walls, relatively large thickness, and small lateral resolution. No standard fabrication technique satisfies all these requirements simultaneously. Highest resolution patterning using electron beam writers, for instance, allows to fabricate a few micrometer deep resist templates, but not 20 µm thick [29]. Optical patterning using UV lithography, on the other hand, can provide sufficiently deep structures, but only at

significantly reduced lateral resolution. X-ray masks are therefore typically fabricated in a more or less complex sequence of various patterning and copying steps, often involving thinner intermediate and full-height X-ray masks. Typical fabrication sequences for X-ray masks are presented in Figure 1.10. X-ray masks obtained from different sequences vary with respect to achievable minimum resolution, which is as also referred to as the critical dimension (CD). Figure 1.10 also presents some rough estimates for the CD associated with different sequences. The cost of fabrication varies with equipment and material expenses, and also increases with the number of steps.

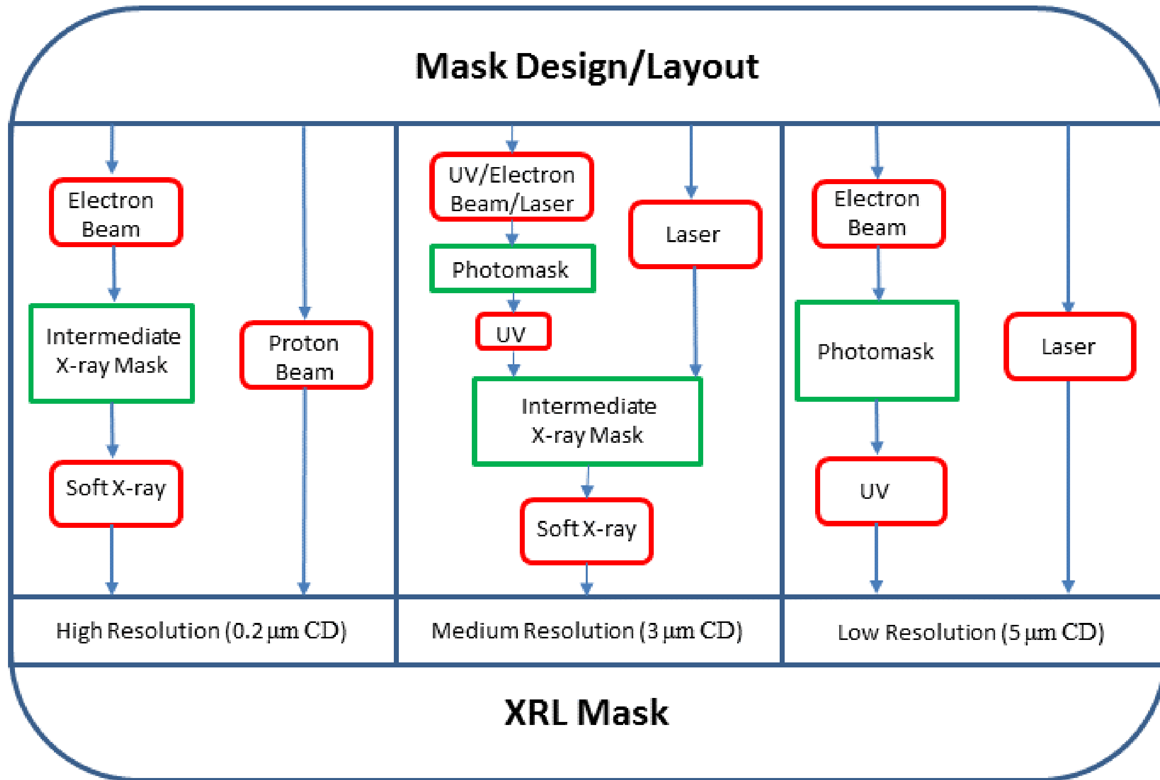

Figure 1.10: Typical fabrication sequences for X-ray masks [14]

The research presented in this thesis focuses on the thermal and thermoelastic behavior of X-ray masks rather than the patterning accuracy of the absorbers. The most cost-effective and fastest patterning approach has therefore been chosen, referred to as the ‘low resolution’ sequence: the layout of a UV mask is copied into the resist of the X-ray mask. Ultimately, this research is meant to contribute to the development of an integrated, new, high resolution patterning sequence in which a laser writer will be applied to pattern a thin intermediate mask based on an economic mask membrane.

1.3 Review of Thermal and Mechanical Analyses of X-ray Exposure

DXRL involves synchrotron radiation, and physical and chemical processes during exposure and development are affected by a huge variety of dependant parameters. Complicated equations describe the

exact properties of synchrotron radiation, and these can be extended to model components of the exposure and development process and the resulting structure accuracies. Thermal and mechanical properties constitute key technical issues, and their analysis has been an ongoing part of DXRL research. Various mathematical models and numerical analyses of the lithographic exposure process have been reported [30][31][32][33]. These studies include several exposure parameters and conditions that determine the temperature rise in the model, such as the spectral and beam power parameters, the beam geometry, the sample geometry, including the proximity gap distance between mask and sample as well as the scanning parameters, and the involved materials properties like the mask absorbers, the membrane, the surrounding gas, and the resist and substrate. The possible heat transfer mechanisms include conduction, convection, and radiation. Thermal conduction from absorbers through the mask membrane, across the proximity gap and photoresist, to the cooled substrate has been identified to dominate the heat dissipation from the X-ray mask to the scanner.

Various approaches have been applied to measure the temperature of the X-ray mask during exposure in real time. One way is to monitor the temperature distribution in the mask during exposure using an infrared camera, as a resolution of 0.1°C can be achieved [34][35]. Another way is to fabricate metal structures on the X-ray mask as a built-in thermistor (thermal resistor), converting a temperature change into a resistance change, with a sensitivity of up to 0.02°C [36]. Last but not least, thermocouples are applied by researchers to measure the temperature of the X-ray mask [37]. A drawback of adding any metal sensor is that they can only be reliably applied behind mask absorbers. They cannot deliver accurate data for the temperature distribution in the open mask membrane, as the metal sensors themselves would strongly absorb radiation, and consequently further heat up the system.

Many studies analyzed thermoelastic deformations of the X-ray mask during exposure [38][39][40]. Thermal expansion of the mask frame can usually be neglected since it is normally made of a thermally well conducting metal, and is in close or direct contact to scanner parts which are often water-cooled, keeping the mask frame at ambient temperatures. The deformations in the mask membrane can be divided into out-of-plane deformations (along the incident beam) and in-plane deformations (within the mask plane) [41]. [42][43] also studied the buildup of the internal stress in the mask membrane and the absorber structures caused by the initial mask fabrication were experimentally verified.

1.4 Experimental Setup in the Synchrotron Laboratory for Micro and Nano Devices (SyLMAND)

The Canadian Light Source (CLS) in Saskatoon, Saskatchewan, is a 3rd generation synchrotron light source with an electron energy of 2.9 GeV and a stored current of up to 250 mA. The bend radius is 7.1428 m, delivering a critical energy of the radiation spectrum of 7.6 keV [44]. This energy divides the broad-band, continuous spectrum, which ranges from infrared to hard X-rays, into two halves of equal beam power.

The Synchrotron Laboratory for Micro and Nano Devices (SyLMAND) at the CLS is Canada's only dedicated DXRL facility, applying an adjustable synchrotron spectrum between approximately 1 keV and 15 keV. The total length of the beamline from the bending magnet to the X-ray scanner is 16.91 m (see Figure 1.11). The beamline can be divided into the front end section, the optics section, and the experimental section or 'end station'. Most of the beamline sections are kept in an ultra-high vacuum, with typical pressure below $5\cdot10^{-9}$ mbar. The major beamline components are an intensity chopper for beam power adjustment, a double mirror system for spectral beam adjustment, and an X-ray scanner (DEX04, manufactured by Jenoptik GmbH; Jena, Germany) for homogeneous sample exposure under an inter gas atmosphere.

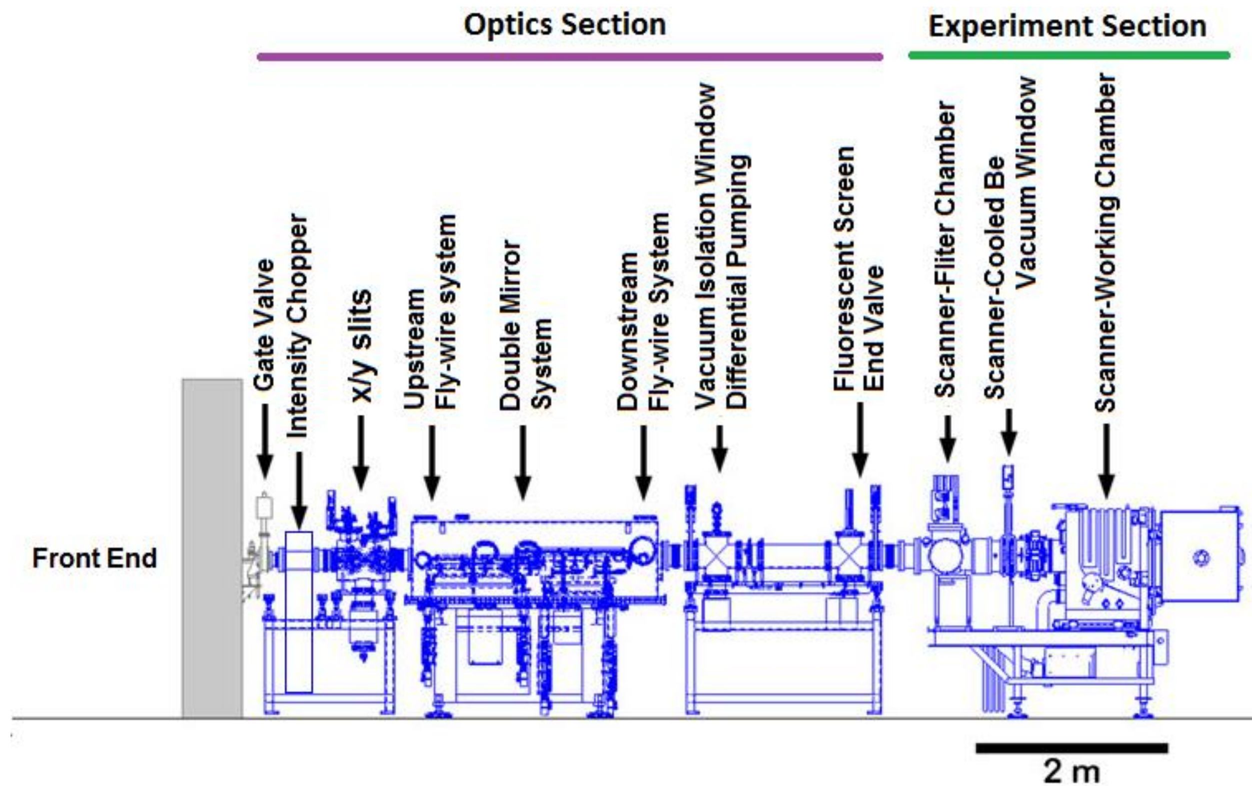

Figure 1.11: Schematic of the SyLMAND beamline. [45]

The synchrotron radiation is generated in the bend magnet in the storage ring, guided through the front end and through the radiation protection wall (grey block in Figure 1.11), and then enters the optics section.

The intensity chopper the first major component of the optics section. It adjusts the beam power by varying the duty cycle of completely transparent ('beam on') and completely opaque ('beam off') time periods. The intensity chopper is a rotating invar steel disk with 31 periodically arranged openings. In a final stage, these openings can continuously be adjusted. In the current implementation, each opening has two defined widths (see Figure 1.12). The duty cycle is determined by the width of these slots, resulting in

either 10% or 25% time-averaged transparency. The intensity chopper is mounted orthogonally to the synchrotron beam, intercepting the beam by rotating at a constant speed of 400 rpm. The rotation speed is fast enough to avoid resonance phenomena between the scanned sample and rotating intensity chopper. The intensity chopper can also be moved out of the beam to deliver the full beam power to the subsequent components [45].

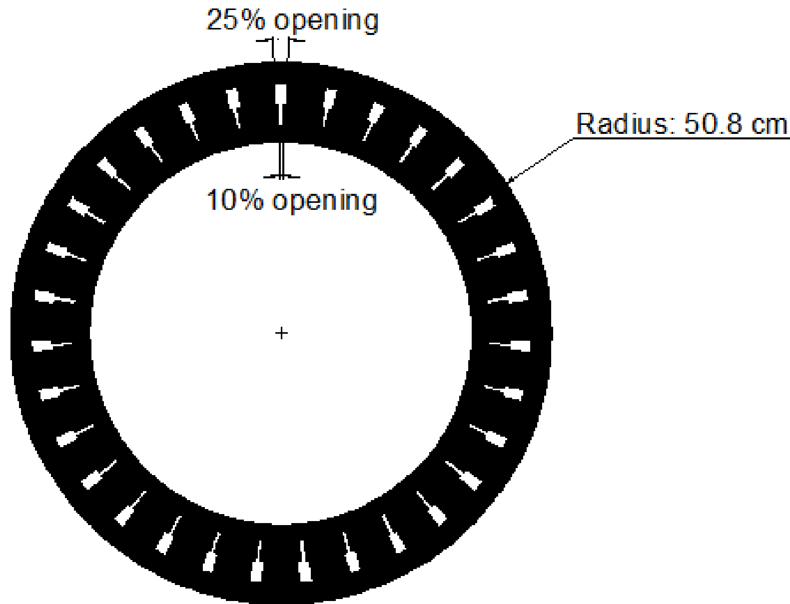

Figure 1.12: Schematic of the intensity chopper disk. (connection beam to the center rotation shaft not included) [45]

The x/y slits can collimate the beam width and height. The four fly-wire systems allow the beam intensity to be measured in both vertical and horizontal direction, both at the entrance and exit of the double mirror system. The double mirror system can be applied to adjust the spectrum of the synchrotron beam by absorption of high energy photons. Both grazing incidence mirrors are cooled and coated with chromium. The mirror angles can be changed individually to tune the spectral adjustment: photons with energies exceeding the angle-dependent cut-off energy are absorbed, while the rest are reflected down the beamline (see Figure 1.13 and Figure 1.14) [49].

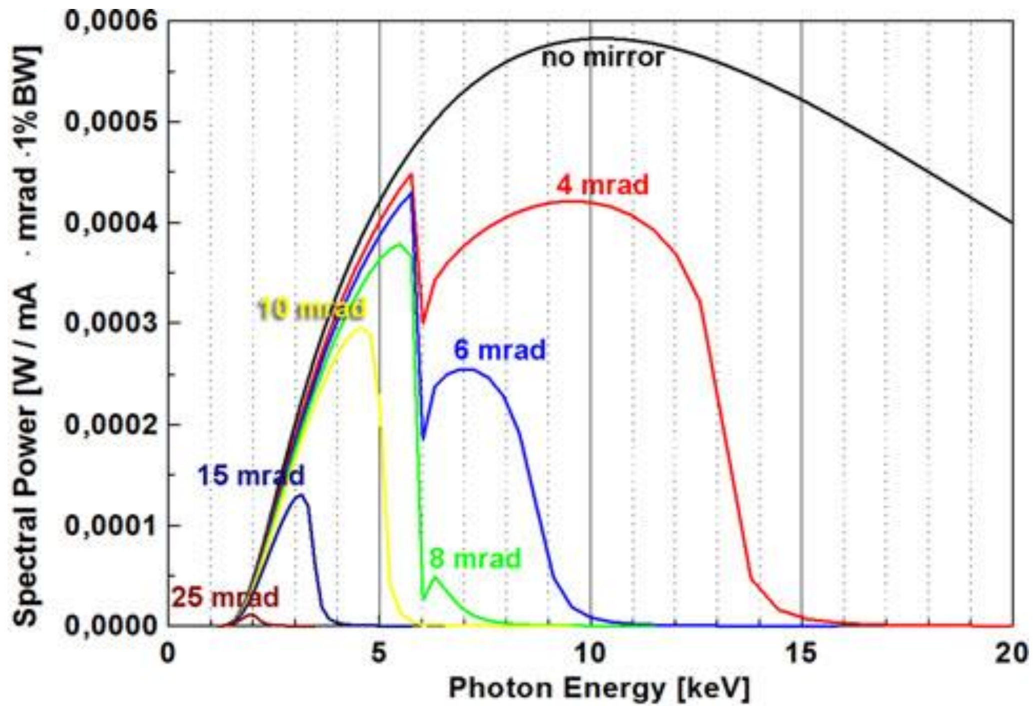

Figure 1.13: SyLMAND spectral power: after 110 μm beryllium vacuum windows; without and with double mirror system at various grazing incidence angles between 4 and 25 mrad. [45]

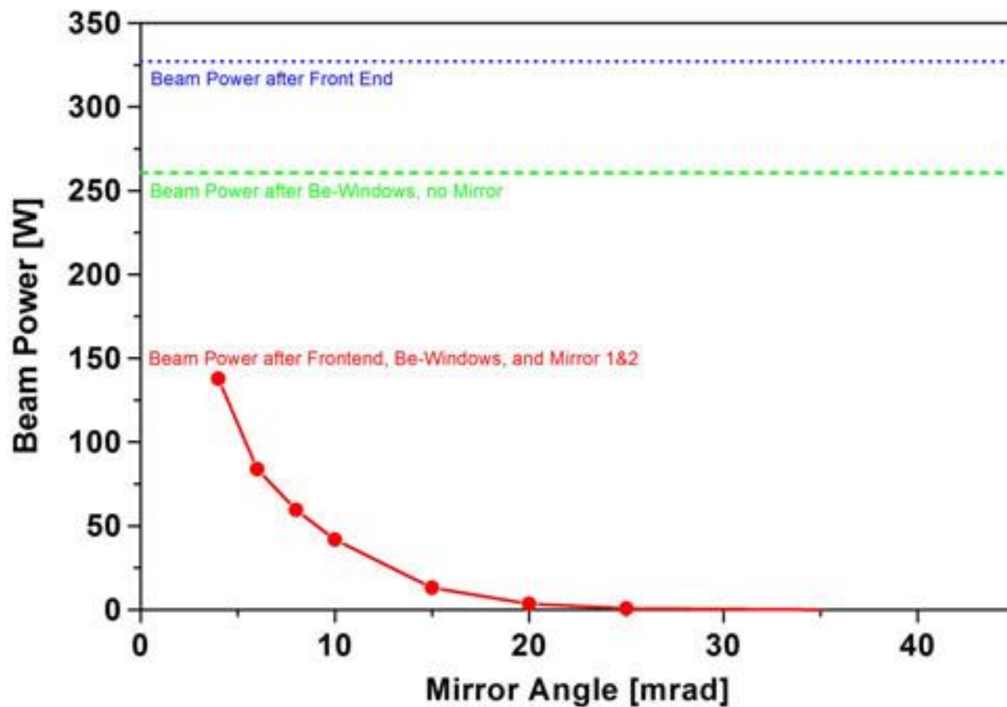

Figure 1.14: SyLMAND beam power (at 250 mA) impinging onto the sample: after the front end; after front end and 110 μm beryllium vacuum windows (261 W); and after frontend, vacuum windows and double mirror system as a function of various grazing incidence angles between 4 and 45 mrad. [45]

Finally, the synchrotron beam passes the filter chamber for additional spectral adjustment and the second vacuum window to the scanner end station where it impinges onto the mask and sample. Two pairs of apertures in vertical and horizontal directions will define the beam size in width and height, which can be adjusted for special exposure requirements.

During exposures, the scanner chamber is filled with 100 mbar helium gas as a buffering environment. Helium provides better heat dissipation than ultra high vacuum would, and at the same time limits the unwanted X-ray absorption at higher gas pressure or ambient air [47]. It also prevents the scanner form corrosion, avoiding the transformation of oxygen into reactive ozone under the impact of X-rays [48].

Figure 1.15 shows a photograph of the SyLMAND scanner stage in the opened position. The assembly of mask and mask holder is seen in its vertical position, while the substrate holder is currently flapped down to a horizontal position for mask and sample loading. When lifted and pushed against the mask, the proximity gap between sample and mask is controlled by proximity shims of typically 50 or 100 μm thickness [49]. During the exposure process, the complete stage assembly is vertically oscilated by an electric motor, scanning the stack of mask and sample through the synchrotron beam.

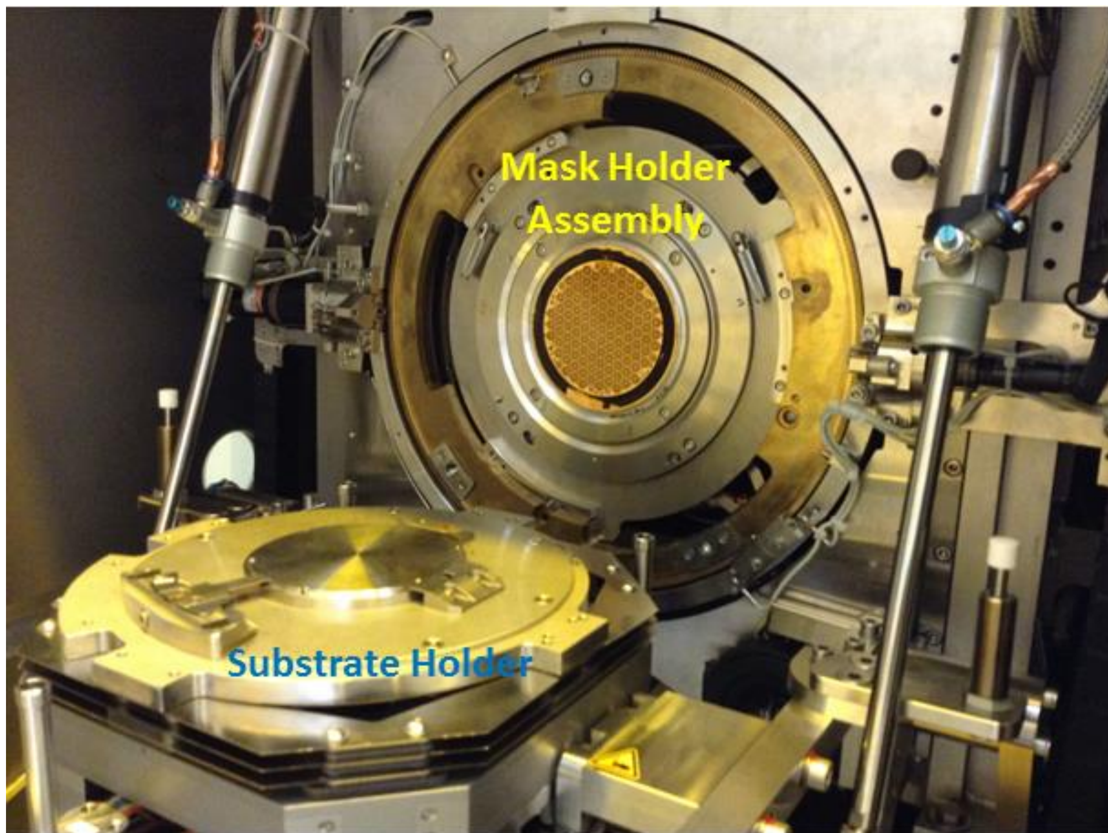

Figure 1.15: SyLMAND scanner stage with assembly of mask and mask holder as well as the substrate holder in the opened position.

The mask holder and substrate holder are both water-cooled. A copper plate with a cooling water tube is brazed to the upstream side of the mask holder to dissipate heat (see Figure 1.16). The substrate holder is internally cooled.

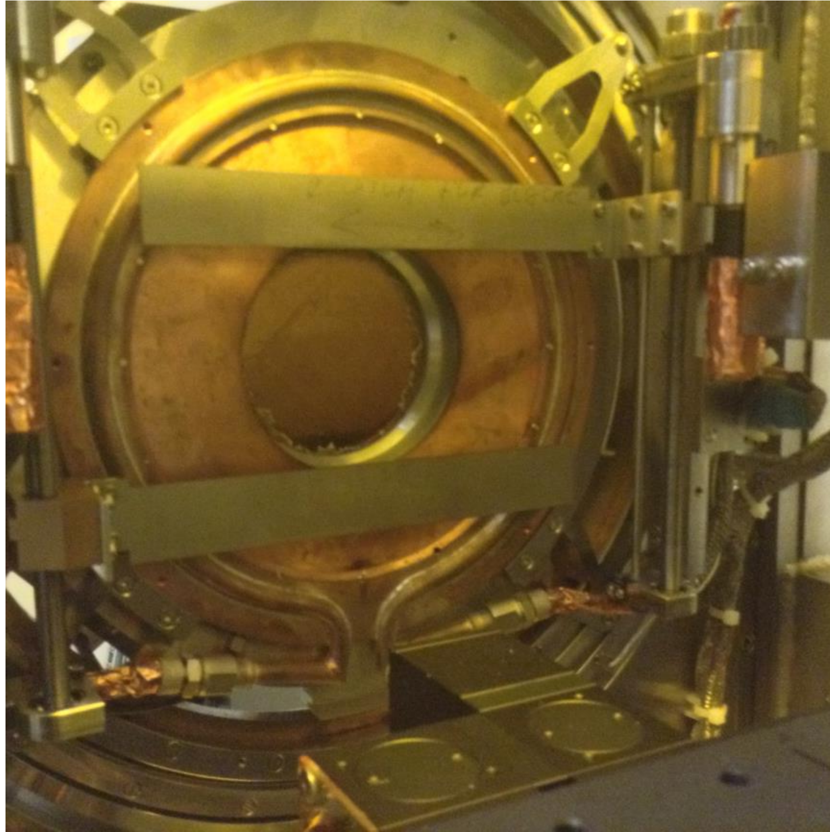

Figure 1.16: Cooling plate of the SyLMAND mask holder (view from the upstream side of the scanner).

1.5 Motivation and Research Objectives

DXRL can be applied to produce polymer or metal microstructures with high aspect ratios and outstanding structure quality. However, it is a particularly expensive MEMS (Microelectromechanical Systems) fabrication technology [50]. Besides cost of exposure, cost associated with mask fabrication is the main reason. Availability and timelines to delivery are also quite limited. Finally, all of the mask fabrication concepts available to date suffer from drawbacks associated with the materials selection or patterning technology. At SyLMAND, a novel masking approach is currently getting developed, merging high resolution patterning by a laser writer as a rapid fabrication approach with other cost and time saving options. A key role plays establishing a polymer mask membrane that is robust, affordable, available, as well as process compatible. Polyimide might be a promising membrane material for good X-ray transmission, absence of fluorescence effects that could reduce the structure accuracy, and outstanding thermal and chemical stability. Thermal deformations during synchrotron exposure, however, have

previously ruled out successful implementation. The continuous tuning capabilities at SyLMAND allow to revisit thermal issues and adjust the process parameters for optimized conditions.

The purpose of this thesis is to investigate whether polyimide could successfully be applied as an X-ray mask membrane material at SyLMAND, what the thermal boundary conditions would be, and how a fabrication process could get implemented.

Specific objectives of this research are to:

1. Identify the properties of polyimide as a potential mask membrane material in DXRL, and determine which kind of polyimide material should be further pursued.
2. Develop a numerical model for a polymer-based mask with different absorber structures to study the impact of different exposure conditions accessible at SyLMAND, and the thermal/thermoelastic behaviour of the test masks during exposure.
3. Develop a fabrication sequence for polymer mask membranes and their integration with a plating base and a suitable mask frame.
4. Integrate such a mask with basic absorber structures to fabricate a complete test mask used to experimentally determine the thermal conditions during exposure and to verify the numerical model.
5. Apply the numerical and experimental results to model thermal deformations under exposure conditions to be expected at SyLMAND for practical applications, and determine intensity chopper settings to limit the deformations to an acceptable level.

1.6 Thesis Organization

This thesis is organized into six chapters.

In Chapter 2, the polymer mask membrane material is further pursued, and fabrication techniques for the polyimide X-ray test mask are developed. This includes patterning of basic absorber structures, delivering a detailed fabrication process for two test masks: one is completely covered with nickel absorber, while the other one has an isolated center block absorber layout.

In Chapter 3, numerical analyses of the thermal and thermoelastic behavior of the test masks are carried out. A numerical model is developed by computational fluid dynamics to simulate the temperature distributions in the two test masks during X-ray exposure. The resulting thermal deformations in the test masks are evaluated at selected time steps during the exposure by finite element analysis.

Chapter 4 provides experimental verification of the thermal simulation. The temperature distributions in the two test masks are measured by thermocouples during synchrotron beam exposure. Different beam

parameters are applied in the experiments in order to obtain a variety of beam powers. In addition, the relationship between temperature in the test masks and incident beam powers is discussed.

Chapter 5 merges the results of the preceding numerical analysis, presenting a prediction of the thermal and thermoelastic behaviors of the test masks and PMMA resist in typical DXRL exposure scenarios, which are based on different resist thicknesses.

Chapter 6 consists of the summary and conclusion of the research, along with suggestions for future work.

CHAPTER 2

POLYIMIDE MATERIALS SELECTION AND FABRICATION PROCESS DEVELOPMENT OF TEST MASKS

2.1. Review of Material Properties of Polyimide as a Potential Mask Membrane Material

Polyimide is a polymer which has been widely applied in various industrial fields since it was first synthesized in 1908 [51]. It has excellent thermal stability and good mechanical and chemical properties to serve as membranes in various technological contexts [52]. Various grades of polyimide have been industrially developed, e.g. Kapton® manufactured by DuPont. Among different types of polyimides, photo-definable ones, such as the HD series by HD microsystems and the Durimide® series by Fujifilm, have been applied in the semiconductor industry because of their excellent thermal and chemical stabilities and their low dielectric constants [53][54].

2.1.1 Thermal and Mechanical Properties

Polyimide has a thermal conductivity of about 0.12 W/m/K. This is a very low value when compared to other membrane materials, including many polymers. A closer look reveals that the exact thermal conductivity of polyimide varies with the thickness and the orientation of the material. An anisotropy of the thermal conductivity has been reported for polyimide thin films of 0.5 to 2.5 µm thickness [55]. A significant disparity between lateral and vertical thermal conductivity was observed, which decreases as the film thickness increases. The degree of cross-linking increases as the material becomes less reduced in the vertical dimension, and the long chain molecules will be more disoriented with less molecule planarity as they are highly cross-linked (see Figure 2.1). [56]

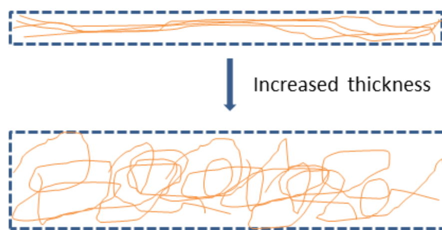

Figure 2.1: Artistic view of molecule chain disorientation due to increased film thickness, leading to reduced anisotropy.

Many factors have influence on the mechanical properties of polyimides: molecular structure, molecular weight (M_w), preparation procedure, and heating history [57]. In general, polyimides exhibit modulus values of 1.5 to 3.0 GPa. Mechanical properties of polyimides strongly depend on the molecular weight and the glass transition temperature. The Young's modulus and shear modulus are mainly affected by temperature, with decreasing modulus values at rising temperature [58]. The other membrane materials discussed are

generally more brittle, which in comparison increases the robustness of polyimide against potential damage by handling.

2.1.2 Radiation Stability

High energetic radiation can cause changes in the properties of polymer materials. The radiation stability of polyimides has been analyzed, revealing that increased dose deposition decreases the tensile strength [59][60]. However, the dose deposition in the polyimide membrane during a single, typical X-ray exposure is far below the threshold dose that leads to a noticeable change of the tensile strength. At the electron stretcher accelerator ELSA of Bonn University, Germany, for instance, polyimide membranes were applied as vacuum windows for up to ten DXRL exposures before they were replaced [61][62].

2.2 Review of Polyimide Mask Membranes used in X-ray Lithography

Polyimide has been considered as a potential mask membrane material since the early days of XRL [63] [64]. The initial development focused on the soft X-ray domain, where both the absorber and the membrane are thin. In DXRL, polyimide was not a frontrunner, particularly because of the low thermal conductivity. Recent development in DXRL has refocussed the attention on polyimide. Optnics Precision from Japan has developed a low-cost, polyimide mask technology for DXRL [65] (see Figure 2.2).

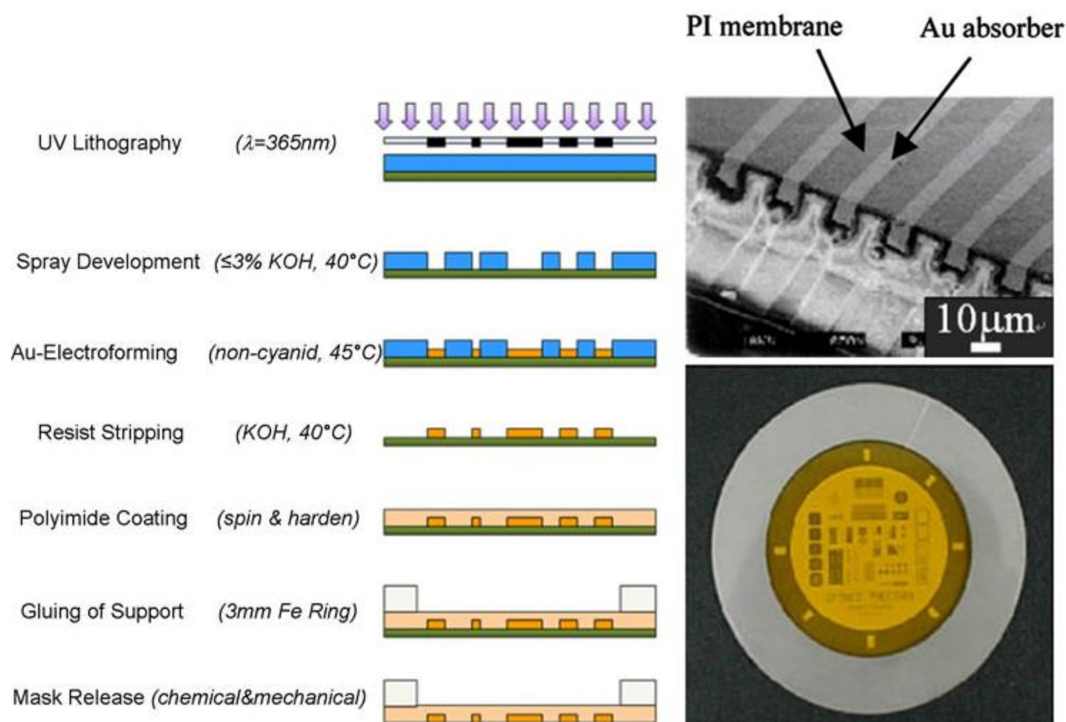

Figure 2.2: Fabrication process for the polyimide X-ray mask by Optnics Precision (Japan): process flow (left), scanning electron micrograph of selected absorber cross sections (top right), and overview of the entire mask (bottom right). [65]

The major drawback when applying the polyimide mask membrane is thermal deformation during exposure [66] (see Figure 2.3). The thermal conductivity of polymer is about 0.12 W/m/K, which is lower than many other polymers, metals or ceramics. Meanwhile, the specific heat capacity is comparatively high (1090 J/kg). This leads to a very low thermal diffusivity of polyimide, i.e. a low heat conduction capacity at a high storage ability. This means heat will be difficult to dissipate by conduction through the polyimide membrane.

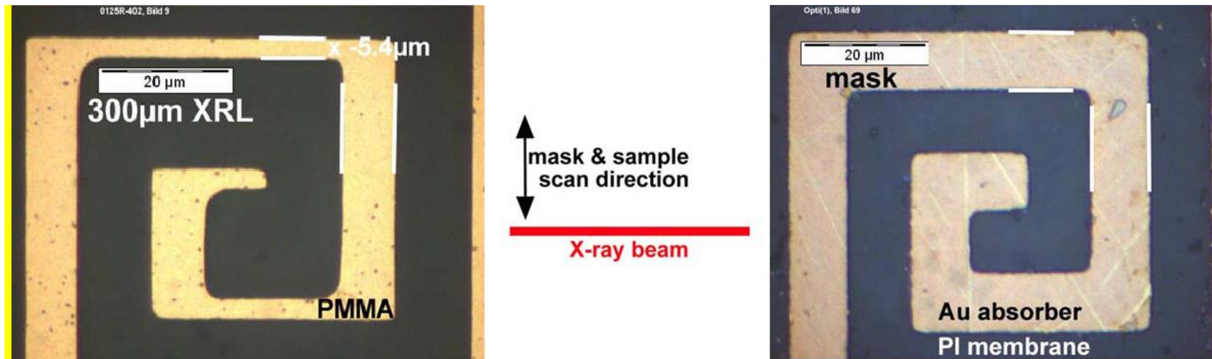

Figure 2.3: Micrographs of a test structure with 10 µm nominal line width. Right: Optnics Precision polyimide mask. Left: Sample exposed at ANKA, beamline Litho2. 300 µm PMMA, dose deposition 9.6:3.5 kJ/cm^3, dip-development in GG developer at 21°C for 7 hours. [66].

The micrographs show that the mask layout with 10 µm nominal feature size was significantly distorted when exposing the mask at the ANKA synchrotron (2.5 GeV electron storage ring) in Karlsruhe, Germany. Thermal deformations in 300 µm thick PMMA amount to about 5 µm orthogonal to the incident synchrotron beam. This is the direction in which the collimated beam constantly locally heats the mask and pushes an expanded mask membrane up and down during each scan, resulting in a relative vertical movement of absorber and resist, reducing the unexposed linewidth of the positive tone PMMA resist in this direction.

Considering all these properties, polyimide is the most promising candidate for a polymer-based mask membrane technology. It will be further pursued in this thesis, developing an initial fabrication process for a demonstrator mask. Such a mask will utilize the beam power tuning capabilities at SyLMAND mentioned in Chapter 1 to limit thermal deformations and demonstrate the overall patterning capabilities. A focus will be on addressing issues of thermal deformations encountered in previous research.

2.3 Process Development for an Integrated Polyimide Membrane

For the test mask to get developed, the target thickness of the polyimide membrane was chosen to be 30 µm, based on X-ray optical performance at the SyLMAND beamline. As an initial lateral dimension, compatibility with 4” wafer standards was preferred. The mask will eventually have an outer membrane

diameter of 100 mm and be freely suspended over 83 mm, using the NIST standard mask frame size described in Chapter 1.

2.3.1 Fabrication Concept Alternatives

In the first step, a fabrication concept, along with strategic selections of different materials, best involved in the polyimide mask needs to be identified.

Polyimide can be purchased as a commercial grade foil, e.g. Kapton® by DuPont. Such a commercial grade offers the advantage of high quality standards with least material deviation between individual samples, good availability in a variety of thicknesses and formats, and significant cost advantage over any membrane fabricated in the laboratory. The challenge would be to attach the highly flexible membrane to a supporting mask frame with homogenous, pre-determined tensile stress to avoid relaxation during operation. Another even more challenging task would be the lithographic patterning of the mask absorber on a membrane suspended in a frame rather than on a massive substrate that can be vacuum-chucked to the patterning tool. These two challenges led to the decision to not further pursue this option in the context of this study.

Alternatively, a dissolved polymer can be spin-coated onto a substrate to achieve a homogeneous layer of the desired thickness. In the following step, the wet polymer layer is heated to remove the solvent, turning the polymer layer into a solid film. Some of those films are photosensitive, such they can subsequently get patterned like a photoresist. Photosensitive as well as non-photosensitive options were investigated, and the consequences on the entire subsequent processing sequence, using one selected material from either group: P84® by Evonik, as a polyimide solution; and Durimide 7520® by Fujifilm, as a negative-tone polyimide resist.

After patterning of the absorbers, the membrane must get attached to a mask frame, and get released from the sacrificial substrate on which the membrane was fabricated. During operation, the membrane cannot be on a rigid substrate as it would unwantedly absorb the entire synchrotron radiation.

The selection of the sacrificial substrate has some important consequences for the entire processing sequence: substrate and membrane can be separated by an intermediate film, and this intermediate film can get dissolved, or serve as a low adhesion strength separation layer. Alternatively, the sacrificial substrate can get completely dissolved from the back side, or dissolution can be performed in just those areas where the polyimide membrane will later have to be freely suspended.

Towards the end of the fabrication sequence, the mask frame gets bonded to the otherwise completed mask, using an epoxy-based two-component glue. Depending on the concept, the mask frame can either be bonded to the membrane side away from the sacrificial substrate, or the substrate gets removed afterwards.

Alternatively, the sacrificial substrate can get locally etched to deliver a freely suspended membrane while still maintaining mechanical support along the edges, and the mask frame then gets glued to the side of the sacrificial substrate. The latter approach was selected and is described later.

2.3.2 Polyimide Material Selection and Membrane Fabrication

The selected two polyimide materials, P84® and Durimide 7520®, were tested to verify the compatibility of spin-coating on silicon wafer and stainless steel substrate.

For the industrial grade P84® polyimide solution, the solid content in the solution is about 25%, which is highly viscous, cannot be spin-coated on the substrate. To reduce the viscosity of the solution, it is diluted with the solvent N-ethyl-pyrrolidone (NEP). To guarantee the homogeneity of the mixture property, the two components need to be mixed through steady vibration for 24 hours. The mixture of acceptable viscosity was found to be 70% P84® and 30% NEP in volume, or 17% and 83% in weight. At this ratio, the viscosity is reduced to a low level that allows spin-coating.

The time for spin-coating is 30 seconds, with the spinning speed set at 500 RPM. After spinning, the substrate should be left on the spincoater for 10 seconds to allow sufficient binding with the substrate surface. The curing steps are same as suggested by Evonik: 30 minutes at 80°C then steadily ramping up until 250°C for 60 minutes.

The quality of the polyimide membrane was investigated by optical microscope, showing a high amount of air bubbles inside (see Figure 2.4). These trapped air pockets reduced the structural homogeneity of the membrane, as it became porous. This problem is caused by the vibration mixing, trapping air inside the mixture. Mixing cannot be performed at reduced pressure to eliminate formation of air bubbles as the highly volatile NEP would evaporate.

Durimide7520®, on the other hand, does not require processing before spin-coating, and thus avoids trapping of air bubbles. It also offers the advantage of a commercial-grade, industrial product with guaranteed quality and manufacturer-suggested processing parameters. It was therefore selected for further testing, revealing the need for some modifications from the manufacturer-recommended procedures to meet the processing needs and capabilities at SyLMAND. The processing sequence for Durimide 7520® is discussed in detail in Section 2.5.

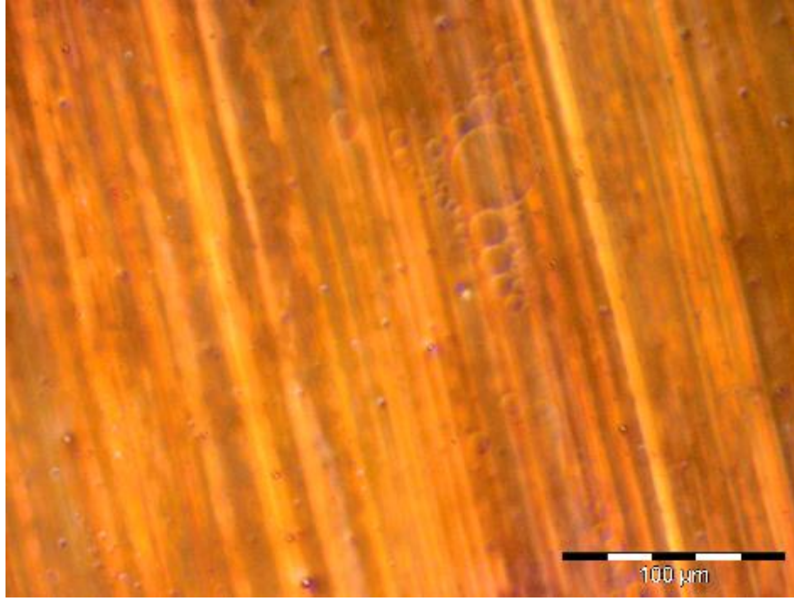

Figure 2.4: Optical micrograph of a typical P84® polyimide membrane surface after mixing, spin-coating and curing: Several air bubbles are visible, particularly in the center of the image.

2.3.3 Selection of the Sacrificial Substrate and Development of the Release Process

The early versions of polyimide X-ray masks were developed on glass or silicon substrates. To obtain a freely suspended membrane, the sacrificial substrates were etched completely or partially in the final processing steps [63][64]. Chemical etching was applied to release the membrane, using an etching agent compatible with the polyimide membrane.

Considering the limitations imposed by equipment available for this research and fabrication costs incurred, stainless steel was chosen as the sacrificial substrate for this research. Important advantages of stainless steel include its high stiffness and ductility. The bending of the substrate in the lateral plane caused by residual stress of the polyimide membrane depends on the modulus of the substrate material, and becomes smaller as the modulus increases [41]. A comparison of mechanical properties and etching process details for the three substrates mentioned above is presented in Table 2.1.

Table 2.1: Mechanical properties and etching features of potential substrates [67]

Substrate Material	Young's Modulus (GPa)	Poisson's ratio	Etching Agent	Etching Selectivity
Glass	66	0.23	HF	Isotropic
Silicon	130	0.28	KOH	Anisotropic
Stainless Steel	193	0.31	$FeCl_3$	Isotropic

2.4 Layout of the Test Masks

Besides the fabrication sequence and the materials involved, the lateral layout of the absorber plays an important role in the planning of the test masks. They will not only be applied to demonstrate the fabrication sequence of polyimide membrane, but also to study the thermal behavior of the masks. Rather than aiming for high resolution test patterns, the masks are therefore laid out to constitute heat load worst-case scenarios. If thermal analysis will deliver acceptable deformations for these cases, all other layouts should be feasible as well.

The first test mask is completely covered with nickel as a consistent absorber layer, resulting in the total absorption of beam power, which is the worst heat load scenario. Heat can dissipate through the nickel layer, where the thermal conductivity is much higher than polyimide.

The second test mask is designed to investigate the lateral thermal conductivity of the polyimide membrane. While a massive absorber is required for significant absorption, no metal conduction path shall support the heat transfer. Thus, a large absorber in the shape of square block, of 42.4 mm side length, is isolated in the center of the mask (see Figure 2.5). The absorber covers one third of the entire layout area. A small extension of the metal absorber is designed between the center block and the mask frame to shield the thermocouples (to be added for temperature measurement in Chapter 4) from incident synchrotron beam.

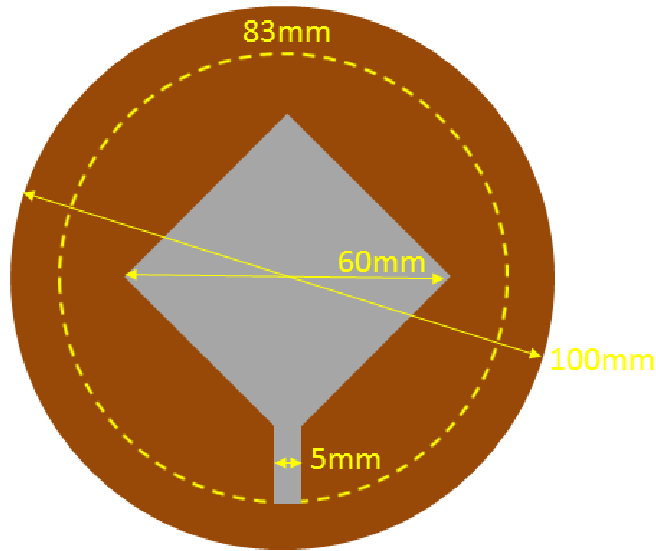

Figure 2.5: Layout of the center block test mask: the center absorber block covers 1/3 of the exposed area, the remaining transparent area of the polyimide is not covered by metal. The membrane is freely suspended on an 83-mm-diameter exposure window.

2.5 Fabrication of the Test Masks

2.5.1 Processing of the Polyimide Membrane

Stainless steel substrates were applied as the sacrificial substrate. They are 4” in diameter, 1.0 mm in thickness, and have a surface roughness of R_a = 1.6 μm (surface roughness grade N7 based on ISO 1302:1992). This roughness promotes adhesion of the spin-coated polyimide by mechanical interlocking.

The steel substrate was cleaned with isopropanol (IPA) and de-ionized water (DI) in order to ensure no chemicals or particulates remain on the surface of the substrate. Then, the steel substrate was cleaned by oxygen plasma etching (5 min at 200 W) to remove potential organic contaminants on the coating surface.

The polyimide membrane is fabricated by spin-coating of Durimide 7520® from Fujifilm. Excerpts from the data sheet are compiled in Appendix A. Spinning parameters include a spread cycle at 500 RPM for 15 seconds, followed by a spinning cycle at 1000 RPM for 30 seconds. Subsequently, the sample is soft-baked on a hotplate at 100°C for 3 minutes. This removes most of the solvent in the resist, partially solidifying the resist with a membrane thickness of approximately 30 μm.

According to the negative resist properties of the Durimide film, the entire sample is then flood-exposed with a UV light source applying a mercury vapor lamp (i-line, wavelengths of 365 nm to 436 nm). The exposure dose recommended for 30 μm Durimide on silicon wafer substrates is 200 mJ/cm^2 [68]. The comparably rough steel surface has a relative low reflectivity and requires an increased dose. 300 mJ/cm^2 were successfully applied to achieve complete exposure.

After exposure, further processing is paused, referred to as a post exposure delay (PED) of 30 minutes, which allows the photo-chemical reaction initiated by the exposure to complete. The final membrane fabrication step is to cure the polyimide at a temperature of 300°C for 60 minutes. This curing temperature is lower than the 350°C suggested by the manufacturer, limited by the hotplate available at SyLMAND and also by the build-up of thermal stress in the assembly of resist and steel. The curing temperature is still high enough to remove most residual solvent in the polyimide. It is important to avoid thermal shocks and keep the temperature rising and later falling at a small, constant gradient in order to control and partially relax the internal stress in the polyimide membrane. Air flow around the sample should be avoided. The hotplate was therefore operated under an enclosure. This way, the heat transfer to cool fresh air can be reduced, limiting the temperature difference within the steel substrate which could else lead to bending problems.

The curing process and the surface roughness of the substrate have significant impact on the membrane quality. The membrane fabricated according to above parameters is transparent and has few defects as observed by optical microscopy (see Figure 2.6). The actual thickness was measured with a stylus surface profiler (Model P11 from Tencor) and well compares to the target thickness of 30 μm.

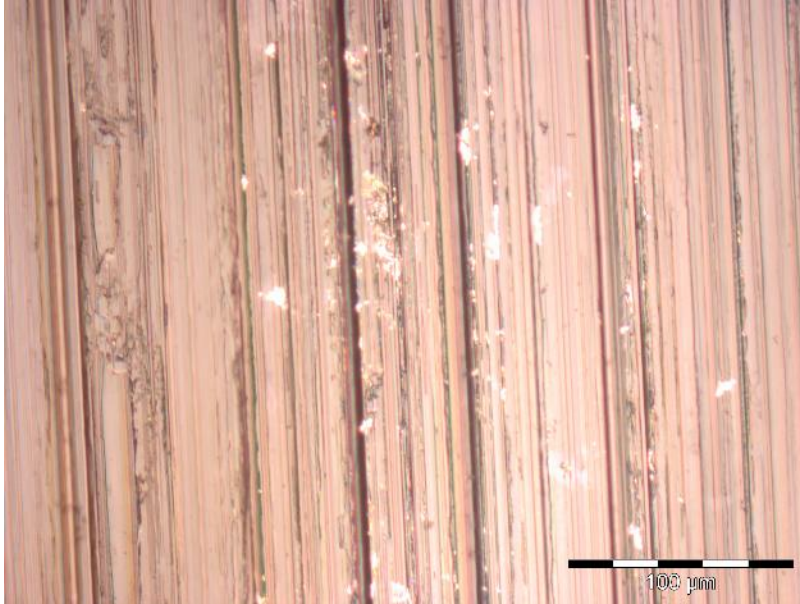

Figure 2.6: Optical micrograph of a Durimide 7520® polyimide membrane.

Electroplating of the mask absorber requires a conductive base layer. Since polyimide is a dielectric, a conductive thin film must be added to the polymer surface. Using sputtering, a physical vapor deposition (PVD) approach, a titanium layer can be added on the cured polyimide membrane. The deposition parameters of PVD process for an approximately 3 µm thick film are presented in Table 2.2.

Table 2.2: Titanium sputtering parameters for thin film coating of the plating base on polyimide.

Base Pressure (mTorr)	7
Argon Gas Pressure (mTorr)	5
DC Power (W)	450
Temperature (°C)	60
Time (Hour)	2.5
Rotation Speed (RPM)	10

The quality of the titanium layer is inspected with a scanning electron microscope (see Figure 2.7). Apparently, the sputtered film is uniform, and adheres well to the polyimide layer underneath. This is, to a large extent, attributed to the PVD process being run at elevated temperatures [69]. The roughness of the titanium layer was determined with an optical profiler, and amounts to approximately 1.4 µm (see Appendix B). The polyimide membrane roughness is close to other mask membrane materials, such as beryllium (1.4 µm) and graphite (0.8 µm) [70][14].

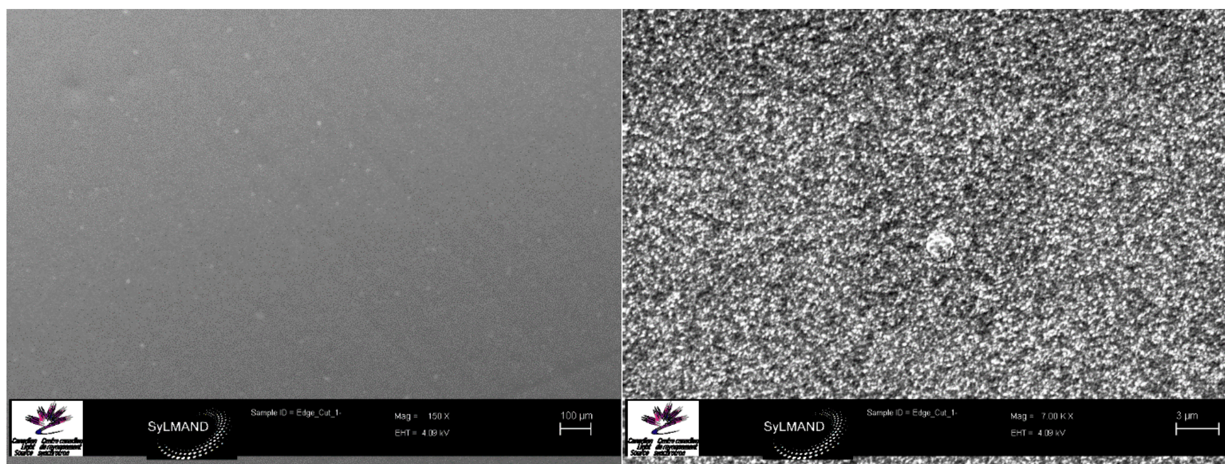

Figure 2.7: Scanning Electron Micrographs (SEMs) of the sputtered titanium layer on polyimide. Left: overview at low magnification (the scale corresponds to 100 µm); Right: detailed close-up (the scale corresponds to 3 µm).

The titanium layer is deliberately partially oxidized to prevent the natural dioxide from forming, which is a dielectric. Formation of $TiO_{x,\ x=1.9}$ is achieved by immersing the processed sample into an aqueous alkali solution of sodium hydroxide (NaOH) and hydrogen peroxide (H_2O_2) at a temperature of 50°C. Experiments have been performed to find an optimized process time of 25 seconds. If the oxidization time is longer than designated, the titanium layer completely delaminates from the polyimide membrane. The optimized finished sample appears as dark black, with a low electrical resistance of less than 3 Ω from center to rim of the substrate.

2.5.2 Patterning of the Mask Absorber Templates

To fabricate the absorber structures on the polyimide membrane, a photoresist is spin-coated on the titanium oxide layer, gets lithographically patterned by ultraviolet radiation, and the voids get filled with metal structures using an electroplating process. A second spin-coating step is required to deposit 100 µm of NR26-25000P® negative tone UV resist (Futurrex; Franklin, NJ). Spinning is performed at 720 RPM for 40 seconds. The resist is soft baked on a hotplate at 150°C for 450 seconds. The center block absorber layout is transferred into the resist using a plastic film based UV mask and a mercury vapor lamp light. The exposure dose was 2200 mJ/cm^2. After a post-exposure bake of 90°C, the sample gets developed in 2.38% tetramethyl ammonium hydroxide (TMAH) for 13 minutes at room temperature.

2.5.3 Electroplating of the Mask Absorber Structures

Based on the processing technology available in the laboratory at the time of the experiments, nickel was selected as the absorber material for the test mask. Compared to gold absorber typically applied, thicker

absorber is required to guarantee complete absorption of the incident beam in the absorber. The nickel layer target thickness is 80 μm.

The nickel electroplating bath SN-10 manufactured by Transene at Danvers, MA, consists of nickel pellets in a titanium basket as the anode, and 4 liters of acidic sulfamate electrolyte containing organic additives and wetting agents. The sample is immersed into the electrolyte as the cathode, maintaining a parallel orientation and constant distance relative to the titanium basket. Using a precision constant current source, nickel gets deposited onto the sample surface.

The electroplated nickel surface usually shows pitting. Pitting can be caused by many factors, such as adhesion of air or hydrogen bubbles to the electroplating surface. Air bubbles should be removed from the electrolyte by stirring. Pitting from adherent hydrogen bubbles can result from a solution that is chemically out of balance, or is inadequately agitated. Further potential causes of pitting are low concentration of wetting agents, the presence of organic contaminants and/or inorganic impurities, and incomplete cleaning of the sample. By maintaining the composition of the electrolyte within specified limits, controlling the pH value and temperature, and by preventing contaminations from entering the solution, pitting can be avoided or reduced [71].

To deposit the nickel layer on the polyimide membrane, the sample is first cleaned with deionized water. The electrolyte needs to be pre-heat to the working temperature of 50°C . A pH value of 4.2 to 4.8 is maintained. The current density is set to 1 A/dm^2, resulting in a deposition rate of 0.2 μm per minute. The plating time for an 80 μm thick nickel layer therefore amounts to 400 minutes. The setup of the electroplating bath is presented in Figure 2.8.

After electroplating, the NR26-25000P® resist template is entirely removed to increase the X-ray transparency of the transparent mask areas. This stripping process is performed in Dimethyl Sulfoxide (DMSO) for 5 minutes at 100°C.

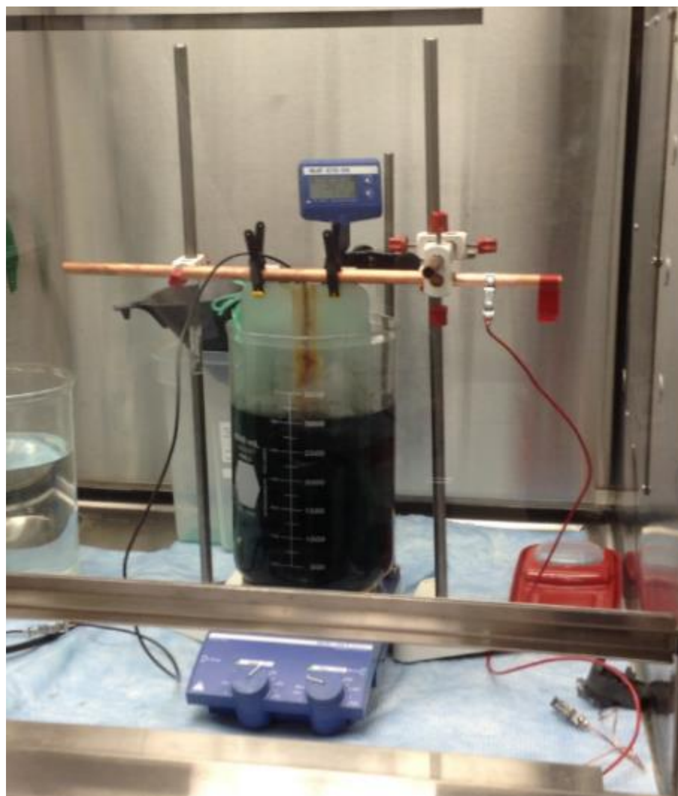

Figure 2.8: Setup of nickel electroplating.

2.5.4 Etching of the Exposure Window and Gluing of the Mask Frame

The polyimide membrane is now patterned with absorber structures. It, however, could not be applied as a mask yet since the steel substrate would absorb all incident X-rays. It needs to be removed as a sacrificial substrate. In this case, rather than removing the entire wafer, an exposure window of 83 mm in diameter was etched as this is regarded as the useful layout area. The outer rim of the steel substrate remains as a support structure.

To create this 83 mm exposure window in the steel substrate, the wafer is chemically etched from the backside. The etchant applied in this study is a 30% ferric chloride ($FeCl_3$) solution. The outer backside rim beyond the 83-mm-diameter is protected against unintentional etching by gluing on a self-adhesive tape. At the edges of the tape, paraffin wax (ScholAR Chemistry; Rochester, NY) is used as a sealant. The melting point of this wax is about 55°C , which is very close to the typical ferric chloride etchant temperature of 50°C [72]. To avoid detachment of the sealant, the etching temperature is reduced to 40°C , at the cost of an increased etch time of 10 hours. 750 ml of fresh etchant are used for each process. After etching of the window, turning the polyimide layer into a freely suspended membrane, the tape is removed and the paraffin wax is dissolved in hot water. The remaining steel ring on the back side (see Figure 2.9) is used as the interface to glue the mask frame.

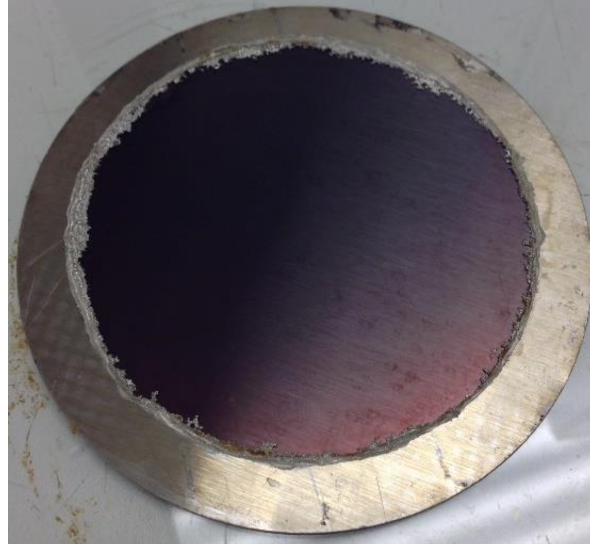

Figure 2.9: Image of a processed mask (before gluing of the mask fame, view from the back side): the steel ring (outer diameter 100 mm, inner diameter 83 mm, thickness 1.0 mm) remains after etching the exposure window into the steel substrate. The orange-red color in the center stems from the polyimide membrane.

The mask frame is attached using a glue for metal bonding. This ensures best thermal contact and good bond strength even at high temperatures. The glue applied is a two-component epoxy (J-B Weld; Atlanta, GA), which takes one day to cure. The mask frame is 101.6 mm wide (4” format), while the mask membrane is only 100 mm wide. Thus, the membrane will not get damaged when mounting in the scanner. At the bottom side, the mask frame extends to 5” for precise mounting in the scanner mask adapter. The final products of test masks are presented in Figure 2.10 and Figure 2.11.

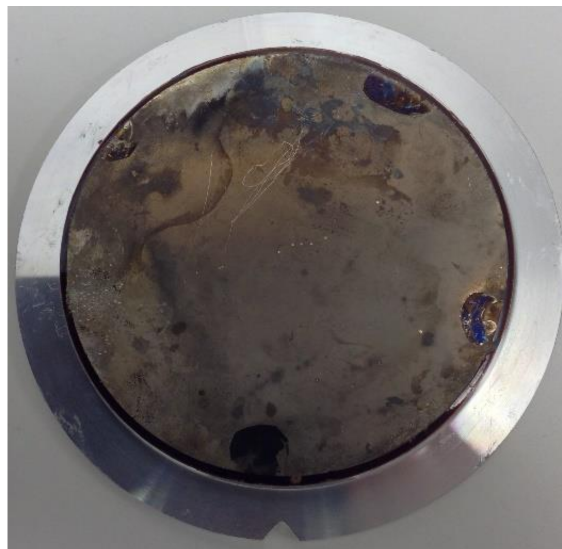

Figure 2.10: Complete coverage test mask seen from the front side: the 80 μm thick nickel absorber covers the entire mask area. The 5” outer diameter mask frame on the back side extends beyond the 4” mask area.

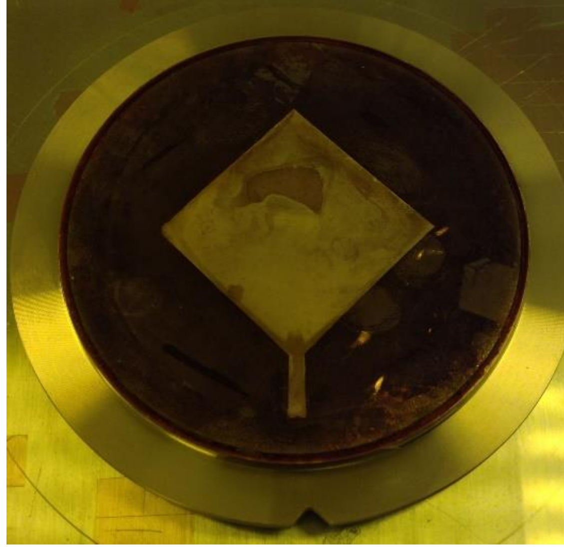

Figure 2.11: Center block test mask seen from the front side: the 80 μm thick nickel absorber covers the square center block and the thin extension strip to protect the wires of the thermocouples (to be mounted later) from X-ray exposure. The 5” outer diameter mask frame on the back side extends beyond the 4” mask area.

2.5.5 Integration of the Individual Fabrication Steps into a Process Sequence

The fabrication steps discussed above can be integrated into a complete processing sequence:

1. Cleaning the stainless steel substrate with isopropanol and de-ionized water followed by an oxygen plasma etch step;

2. Spin-coating of 30 μm Durimide 7520® polyimide resist on the steel substrate;

3. Soft baking of the polyimide resist;

4. Flood exposure of the polyimide resist with ultra-violet light, followed by post-exposure delay;

5. Curing of the polyimide resist;

6. Adding a 3 μm layer of titanium on the polyimide membrane by PVD;

7. Oxidizing the titanium layer to $TiO_{1.9}$;

8. Spin-coating 100 μm NR26-25000P® negative tone UV-resist on the $TiO_{1.9}$ layer;

9. Patterning the absorber template by UV-exposure with a film mask and development in 2.38% TMAH;

10. Electroplating of the absorber pattern with nickel sulafamate;

11. Stripping of the remaining NR26-25000P® resist in DMSO;

12. Etching of the exposure window from the backside of the steel substrate in 30% $FeCl_3$ until the membrane becomes freely suspended;

13. Bonding the test mask to mask frame using 2-component epoxy glue.

The critical steps are illustrated in the process flow diagram in Figure 2.12.

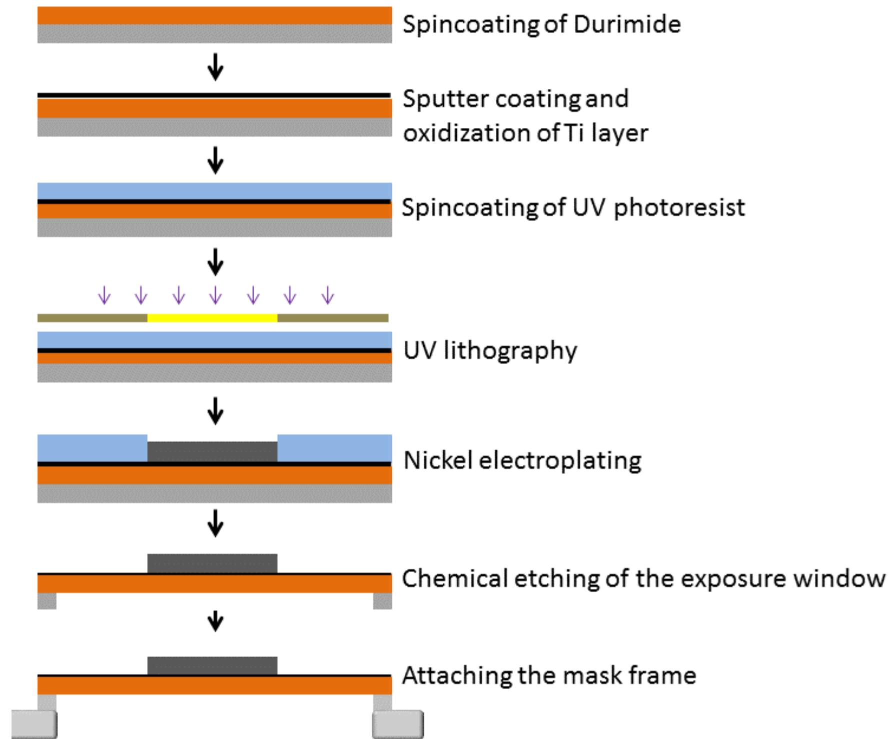

Figure 2.12: Fabrication sequence developed for polyimide X-ray masks at SyLMAND.

2.6 Chapter Summary

In this chapter, the selected properties of polyimide are further reviewed to determine the suitability of the material as an X-ray mask membrane. Two polyimide products were experimentally studied: 1) P84® polyimide solution from Evonik has been diluted with NEP solvent into a spincoatable polymer; 2) Durimide 7520® is a photo-definable polyimide from Fujifilm. Both have been spincoated to examine the quality of a thin film to eventually be used as the mask membrane. In the case of P84®, poor homogeneity caused by air pockets prevented further use. For Durimide 7520®, a detailed fabrication sequence has been developed to reliably produce polyimide thin films with the equipment available at SyLMAND. Stainless steel wafers were selected as the sacrificial base substrate due to the high modulus in order to minimize bending of the test mask during fabrication process. A 30 μm thick Durimide 7520® film was spincoated onto the sacrificial substrate. $TiO_{1.9}$ was then sputter-coated onto the polymer to be later used as the plating base for electroplating the absorbers. On the plating base, 100 μm of UV-sensitive negative-tone resist

Futurrex NR26-25000P® were spin-coated and patterned by UV-exposure. The voids in this microstructure were filled with 80 µm thick nickel, serving as the absorber in test masks. The polyimide film was finally turned into a freely suspended membrane by locally removing the sacrificial steel wafer. An exposure window of 83-mm-diameter was opened by etching the steel wafer with a 30% ferric chloride solution. As the last fabrication step, the mask shim was bonded to a rigid mask frame using epoxy glue. Two test masks were fabricated with this same fabrication sequence, but different layouts: one mask is completely covered by absorbers; the second has an absorber layout of 42.4 mm side length square at the center, while the remaining exposure window is transparent. The two test masks provided the basis for further experimental and numerical studies.

CHAPTER 3

THERMAL AND THERMOELASTIC ANALYSIS OF THE POLYIMIDE MEMBRANE MASK

The heat load during X-ray exposure will determine the feasibility of a polyimide membrane X-ray mask technology at SyLMAND. SyLMAND is equipped with an intensity chopper, which allows to reduce the incident beam power, so that heat load in the mask and resist can be kept at acceptable levels. As a result, the temperature rises in the mask as well as the thermal deformations will be reduced. In this chapter, thermal and thermoelastic behavior of the test masks are studied by numerical methods, predicting the temperature distributions and thermal deformations in the masks during exposure.

3.1 Modeling of the X-ray Exposure under Synchrotron Radiation

3.1.1 Simplifications and Assumptions in the Simulation Models

To simulate the heat load, the geometry of the exposure model is simplified as presented in Figure 3.1. Photoresist and silicon wafer are not included in this model. The assembly of the test mask and the substrate holder is reduced to a space of 140 mm × 140 mm × 18.2 mm. The helium-filled control volume is limited to the proximity gap between substrate holder and mask holder, and to the exposure window of the mask holder. The complex geometries of mask holder and substrate holder (compare with Figure 1.15) are reduced to flat walls, with the proximity gap of 1.4 mm in-between. This a larger than typical proximity gap distance, but will be necessary for subsequent experimental verification when thermocouples are placed through the proximity gap. The extension segment protecting the thermocouple wires in the center block mask is neglected for the simulations. The mask is simplified to a layer of nickel absorber on a polyimide membrane, attached to the steel ring and aluminum mask frame. The x-y plane is the lateral plane, and z-axis is the propagation direction of synchrotron beam. (see Figure 3.1)

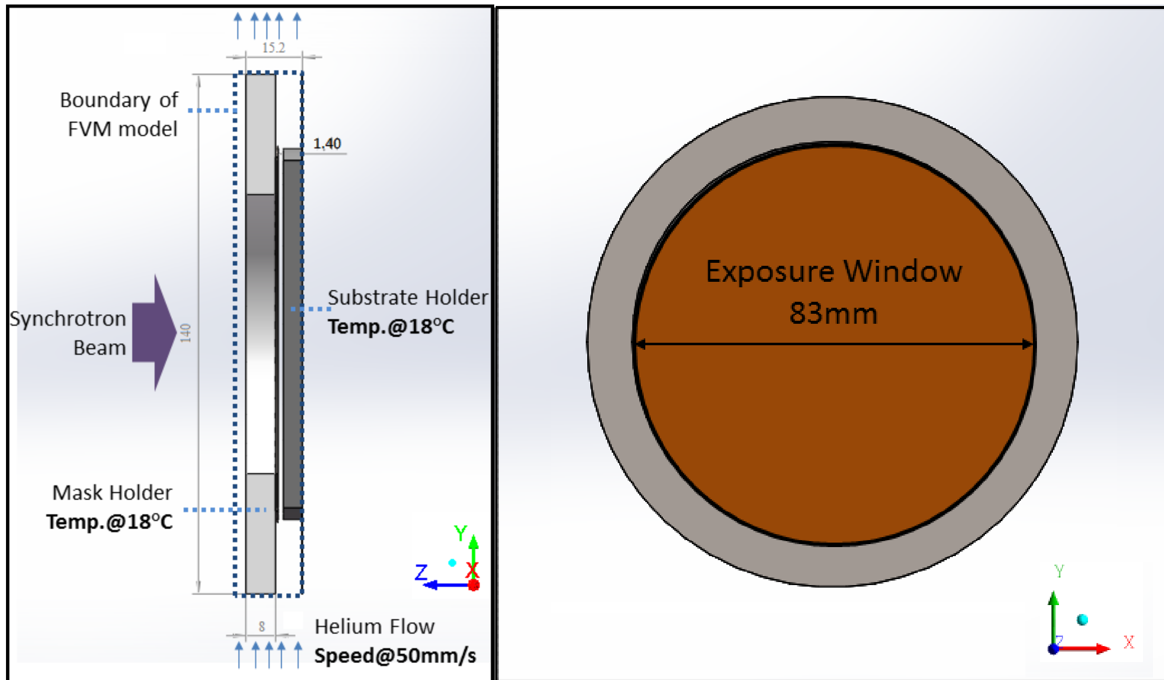

Figure 3.1: Schematic of the simplified Finite Volume Method (FVM) model for thermal simulations: Left: cross sectional view; Right: front view of the test mask, which is simplified to a layer of nickel absorber on the polyimide membrane.

The helium pressure in the scanner working chamber during the exposure is 100 mbar. As the stage scans through the chamber, the helium gas has a relative velocity with respect to the scanning stage, flowing in the proximity gap between the X-ray mask and the substrate holder. The impact of this gas flow, resulting dimensionless numbers, and a suitable boundary condition are derived based on the calculations of the fluid dynamic properties for the helium in Appendix C. Continuum fluid mechanics with slip flow boundary conditions where the relative velocity at the channel wall is non-zero would best be applied in the model. However, the calculations of dimensionless numbers show that convection is not significant as the helium gas flow is at a low velocity. Thus, not convection associated with the helium gas flow, but rather thermal conduction is the dominant mode of heat dissipation in the proximity gap. To simplify the thermal simulation, the slip flow condition is therefore neglected. Also, the reciprocating flow direction of helium is simplified to be single directional.

The effective vertical beam height at the scanner is about 8.8 mm. The maximum width of the synchrotron beam is 150 mm. It can be collimated by different slits in the beamline. In the case of the test mask described in the previous chapter, the beam would get collimated to 83 mm by the mask frame, if not cut upstream. It is therefore assumed that diligent sample preparations will ensure that the beam power is not dissipated into the mask frame, but that slits upstream in the beamline collimate the beam to the useful

width. An incident beam width of 83 mm is therefore assumed as the worst case scenario, from a heat load perspective, associated with the dimensions of the test mask.

The incident beam power is constant across the beam width, but varies with a Gaussian power profile in the vertical direction. During exposure, the scanning process evens this vertical profile out to a homogeneous energy deposition across the entire sample. In the simulations, the vertical power distribution is therefore not modeled, but is represented by the corresponding incident power averaged over the 8.8 mm by 83 mmm beam size. The incident beam power density is calculated using the software LEX-D developed by Sandia National Laboratory, Livermore, USA (see Appendix D). It takes into account the storage ring and beamline conditions, the stored electron current, as well as absorption in all beamline optical components, the mask, and the sample. The data fed into the numerical model therefore deliver the values for absorbed energies as the local heat sources in all relevant layers of the model. Figure 3.2 presents the transmission of the mask components for the given spectral range: the polyimide membrane allows for good transmission beyond 90% for relevant photon energies beyond 3 keV, and close to 100% for photon energies of 5 keV and above. The nickel absorber, on the other hand, is almost entirely opaque to the photons within the spectrum. It allows transmission of less than 10^{-3} for the energy spectral range, and a maximum of 1% to 6% at selected spectral peaks. In blank membrane areas where there are no absorbers, less than 10% of the locally incident beam power is deposited into the polyimide membrane, depending on the exact exposure conditions. The remaining beam power gets transmitted through the membrane into the sample and substrate holder where it is absorbed. Considering the heat transfer in the entire model, most of the beam power gets absorbed in the mask absorber, from where it gets dissipated as heat through the entire model. The model takes into account the various heat sources due to deposited beam power, regardless of the location in the model.

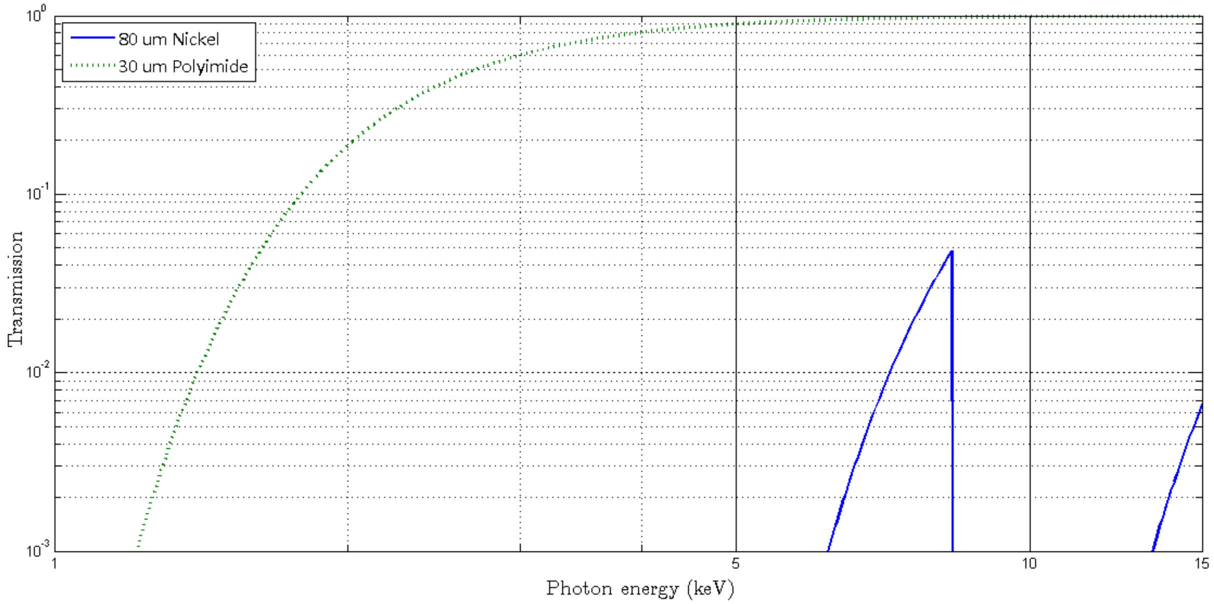

Figure 3.2: X-ray transmission of the X-ray mask components from 1 to 15 keV [22].

The temperature distribution is simulated using the comprehensive model explained above, including mask and substrate holders which impact the mask temperature. Thermal deformations are based on this temperature distribution. Deformations of the holders, however, are neither expected in the cooled scanner components, nor would they have an immediate impact onto the microstructures. The thermoelastic model is therefore further reduced to the X-ray mask structure (see Figure 3.3). The bonds between the polyimide membrane, nickel absorber, and the steel ring are considered to be rigid so that relative slip or twist will not appear.

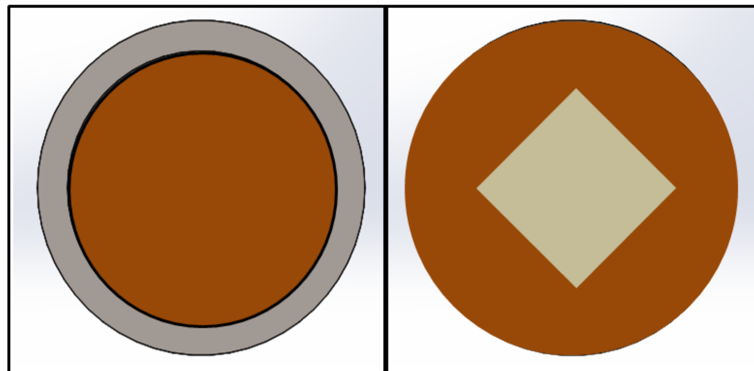

Figure 3.3: Schematic of the simplified mask model for thermoelastic simulations: Left: Back view of the test mask, the steel ring constrains the polyimide membrane; Right: Front view of the simplified center block mask.

3.1.2 Governing Equations and Boundary Conditions

A. Thermal simulation

To describe heat diffusion in a solid, the governing equation in a Cartesian system is

$$k\left(\frac{\partial^2 T}{\partial x^2}+\frac{\partial^2 T}{\partial y^2}+\frac{\partial^2 T}{\partial z^2}\right)+Q(x,y,z,t)=\rho c\frac{\partial T(x,y,z,t)}{\partial t} \tag{3.1}$$

where k is the thermal conductivity of the solid, ρ is the material density, c is the specific heat of the material, Q is the heat generation rate, and T is the temperature [73].

The X-ray mask under synchrotron beam irradiation will be heated locally as energy gets deposited in the absorber and in the membrane. In the case of the entirely nickel-covered mask, all beam power is absorbed in the absorber (see Figure 3.4). To describe the heat diffusion in the X-ray mask, the governing equations are

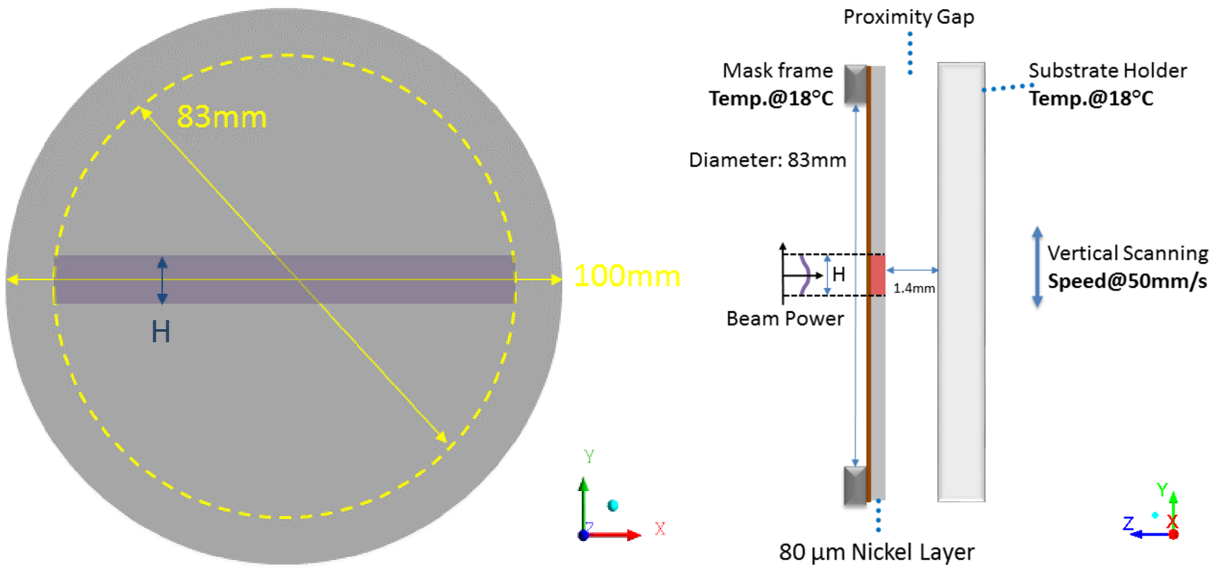

Figure 3.4: Schematic of the DXRL exposure model used in the simulation of the complete coverage mask: Left: Exposure of the X-ray mask under synchrotron beam; Right: Heat generation in the absorber during exposure.

$$
\begin{aligned}
&-k_{PI}\left(\frac{\partial^2 T}{\partial x^2}+\frac{\partial^2 T}{\partial y^2}+\frac{\partial^2 T}{\partial z^2}\right)+\rho_{PI}c_{PI}\frac{\partial T}{\partial t}=0 \\
&-k_{Ni}\left(\frac{\partial^2 T}{\partial x^2}+\frac{\partial^2 T}{\partial y^2}+\frac{\partial^2 T}{\partial z^2}\right)+\rho_{Ni}c_{Ni}\frac{\partial T}{\partial t}=q(x,y,t)A_{beam} \\
&q(x,y,t)=\begin{cases} P_{beam}(-41.5\le\sqrt{x^2+y^2}\le 41.5\text{mm},-4.4\le y\le 4.4\text{mm}) \\ 0 \end{cases} \\
&A_{beam}=HL
\end{aligned}
\tag{3.2}
$$

where P_{beam} is the internal heat generation rate in the exposed absorber by the synchrotron beam, A_{beam} is the projected area of the synchrotron beam, H is the height of the beam (8.8 mm), and L is the width of the beam (83 mm).

To describe the thermal balance of the model, a schematic is presented in Figure 3.5.The temperature in the lumped heat capacity system of the mask depends on the absorbed beam power as well as the heat dissipation mechanism to the various cooled scanner parts. The system is divided into three zones: 1. mask; 2. helium gas; 3. substrate holder. The heat dissipation of the mask can comprise contributions of convection, conduction, and radiation into the surrounding environment. The thermal balance among the zones is expressed by the following equations:

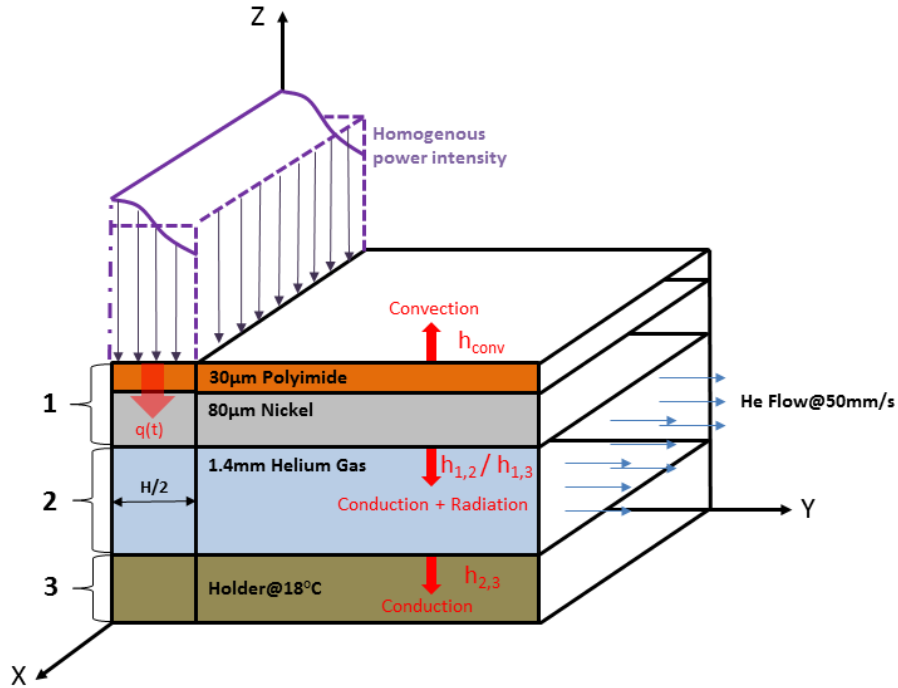

Figure 3.5: Thermal balance of the model (cross-sectional view of the modeled layers and the incident synchrotron beam).

$$
\begin{aligned}
&\rho_1 c_1 V_1 \frac{dT_1}{dt} = q(t)A_{beam} - Ah_{1,3}(T_1 - T_3) - Ah_{1,2}(T_1 - T_2) - Ah_1(T_1 - T_0) \\
&\rho_2 c_2 V_2 \frac{dT_2}{dt} = Ah_{1,2}(T_1 - T_2) + Ah_{2,3}(T_3 - T_2) \\
&\rho_1 = \begin{Bmatrix} \rho_{PI} \text{ @ uncovered area} \\ \rho_{Ni} \text{ @ covered area} \end{Bmatrix}, c_1 = \begin{Bmatrix} c_{PI} \text{ @ uncovered area} \\ c_{Ni} \text{ @ covered area} \end{Bmatrix} \\
&h_1 = h_{conv}, h_{1,2} = \frac{k_{Ni}k_{He}}{k_{Ni}D_2 + k_{He}D_1}, h_{1,3} = F_{13} \cdot 4\varepsilon_1 \sigma T_0^3, h_{2,3} = \frac{k_{He}k_{Steel}}{k_{He}D_3 + k_{Steel}D_2}
\end{aligned}
\tag{3.3}
$$

where A is the area of exposure, D is the thickness for each layer, h is the heat transfer coefficient for each layer (h_1 is between the mask and helium gas in the exposure window, $h_{1,2}$ is between the mask and helium gas in the proximity gap, $h_{1,3}$ is between the mask and the substrate holder, $h_{2,3}$ is between helium gas in the proximity gap and the substrate holder), F is the view factor of radiation (in this case F_{13} is 1), ε is the emissivity of absorber (0.11 for nickel [74]), σ is the Stefan-Boltzmann constant ($5.67 \cdot 10^{-8}$ W/m^2/K^4), and T_0 is the background temperature of 18°C [75].

B. Thermoelastic simulation

The basic equations of elasticity for the homogenous and isotropic material per unit volume under the internal body forces are (see Figure 3.6)

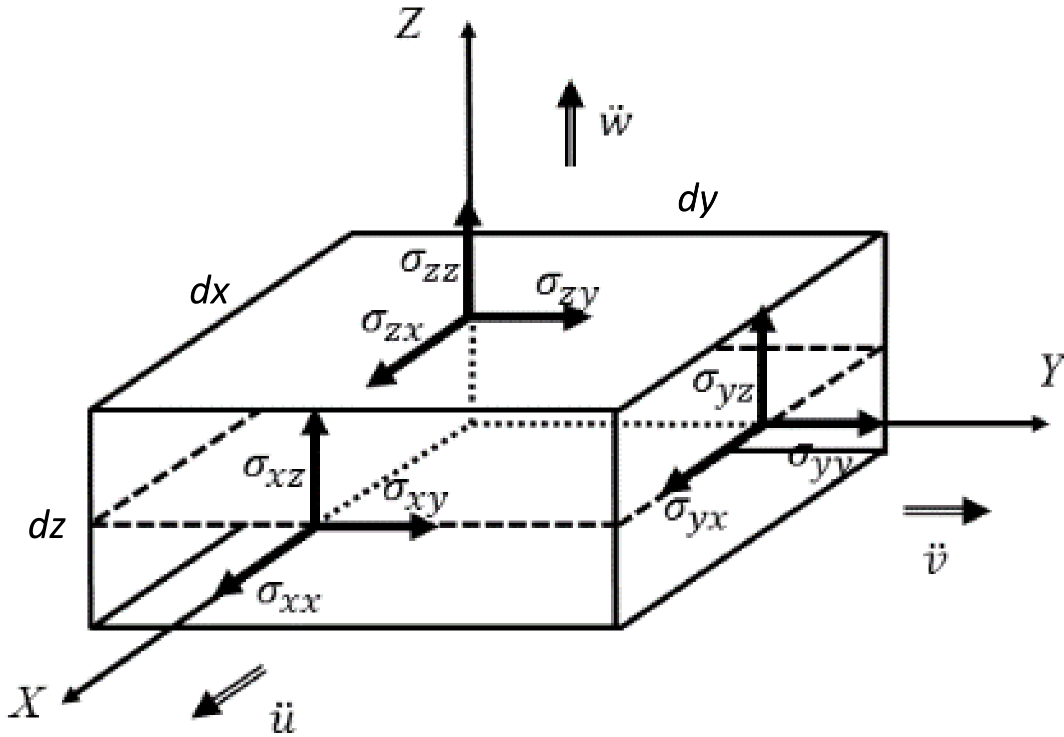

Figure 3.6: Components of stress in three dimensions.

$$\frac{\partial \sigma_{xx}}{\partial x} + \frac{\partial \sigma_{yx}}{\partial y} + \frac{\partial \sigma_{zx}}{\partial z} + X = \rho \ddot{u}$$
$$\frac{\partial \sigma_{xy}}{\partial x} + \frac{\partial \sigma_{yy}}{\partial y} + \frac{\partial \sigma_{zy}}{\partial z} + Y = \rho \ddot{v} \tag{3.4}$$
$$\frac{\partial \sigma_{xz}}{\partial x} + \frac{\partial \sigma_{yz}}{\partial y} + \frac{\partial \sigma_{zz}}{\partial z} + Z = \rho \ddot{w}$$

where σ is the Cauchy stress tensor (normal stresses: σ_{xx} , σ_{yy} , σ_{zz} ; shear stresses: σ_{xy} , σ_{xz} , σ_{yx} , σ_{yz} , σ_{zx} , σ_{zy}), X, Y, and Z are the internal body forces, and the second order derivatives of u, v, and w are the accelerations in Cartesian coordinates [76].

The relationship between strain, displacement, and stress is given by the Hooke's law as

$$\varepsilon_{xx} = \frac{\partial u}{\partial x} = \frac{1}{E}\left[\sigma_{xx} - \upsilon\left(\sigma_{yy} + \sigma_{zz}\right)\right] + \alpha\left(T - T_0\right)$$
$$\varepsilon_{yy} = \frac{\partial v}{\partial y} = \frac{1}{E}\left[\sigma_{yy} - \upsilon\left(\sigma_{zz} + \sigma_{xx}\right)\right] + \alpha\left(T - T_0\right)$$
$$\varepsilon_{zz} = \frac{\partial w}{\partial z} = \frac{1}{E}\left[\sigma_{zz} - \upsilon\left(\sigma_{xx} + \sigma_{yy}\right)\right] + \alpha\left(T - T_0\right)$$
$$\varepsilon_{xy} = \frac{\partial v}{\partial x} + \frac{\partial u}{\partial y} = \frac{\sigma_{xy}}{2G} \tag{3.5}$$
$$\varepsilon_{yz} = \frac{\partial w}{\partial y} + \frac{\partial v}{\partial z} = \frac{\sigma_{yz}}{2G}$$
$$\varepsilon_{zx} = \frac{\partial u}{\partial z} + \frac{\partial w}{\partial x} = \frac{\sigma_{zx}}{2G}$$

where ε in the strain tensor, υ is the Poisson's ratio, α is the coefficient of thermal expansion (CTE), T-T_0 is the temperature change, and G is the shear modulus [77].

For the thin structure in this study, the stresses in the vertical direction can be neglected. So the normal and shear stresses along the z-axis are assumed to be zero as

$$\sigma_{zz} = \sigma_{xz} = \sigma_{yz} = 0 \tag{3.6}$$

From Hooke's law (compare to 3.5)

$$\varepsilon_{xz} = \varepsilon_{yz} = 0$$
$$\varepsilon_{zz} = -\frac{\upsilon}{E}(\sigma_{xx} + \sigma_{yy}) + \alpha\left(T - T_0\right) \tag{3.7}$$

The steel ring of the test mask is regarded as a rigid physical constraint, where the deformation of the mask structure is zero within the bonding area with the mask frame.

To compare the stress distribution of various nodes in the model, the equivalent stress (von-Mises stress) is defined as

$$\sigma_e = \left[\frac{\left(\sigma_{xx} - \sigma_{yy}\right)^2 + \left(\sigma_{yy} - \sigma_{zz}\right)^2 + \left(\sigma_{zz} - \sigma_{xx}\right)^2 + 6\left(\sigma_{xy}^2 + \sigma_{yz}^2 + \sigma_{zx}^2\right)^2}{2} \right]^{1/2} \tag{3.8}$$

3.2 Simulations

The commercial numerical analysis software package used in this study is ANSYS R14.5. The model developed in this study divides the simulation in two steps which involve a different discretization as stated above, and also different ANSYS components: the temperature distribution in the test masks during the transient conditions of the scanned exposure are solved with the computational fluid dynamics software ANSYS FLUENT® for each time step of the considered scanning process using the finite volume method (FVM). Based on these temperature distributions, the thermoelastic stresses and the deformations are determined by ANSYS Mechanical® using the finite element method (FEM), focusing on the maximum temperature rises at thermocouples in the mask.

3.2.1 Meshing of the Model

The models need to be meshed separately for the thermal and the thermoelastic simulation due to the different numerical methods involved. The X-ray mask consist of comparatively thin membrane (30 μm) and absorber (80 μm), but a 1,250 or 3,333 times larger lateral dimension (100 mm). To keep the number of elements in the mesh at a manageable level for computer, and to ensure the maximum aspect ratio in any given mesh cell does not exceed 100:1 (cells no more than 100 times wider than thick in this case) so that the results converge well and remain accurate, single layer of elements will be generated in each of these two zones.

The mesh for the thermal simulation applying the FVM was built by the software GAMBIT®. The mesh is a conformal grid solely consisting of quadrilateral cells. The FEM mesh for the thermoelastic simulation was built by ANSYS Meshing®, covering only the test masks themselves. Most elements are 20-node cuboids referred to as *Hex 20*, while a few elements are 15-node prisms referred to as *Wed 15*. The two types of element are simultaneously identified as *Solid 186* in ANSYS Mechanical® (see Figure 3.7).

Complete information on the four meshes used for the thermal FVM and the thermoelastic FEM model for both the test masks are presented in Table 3.1. The thermal and thermoelastic properties of the materials in the simulations are presented in

Table 3.2.

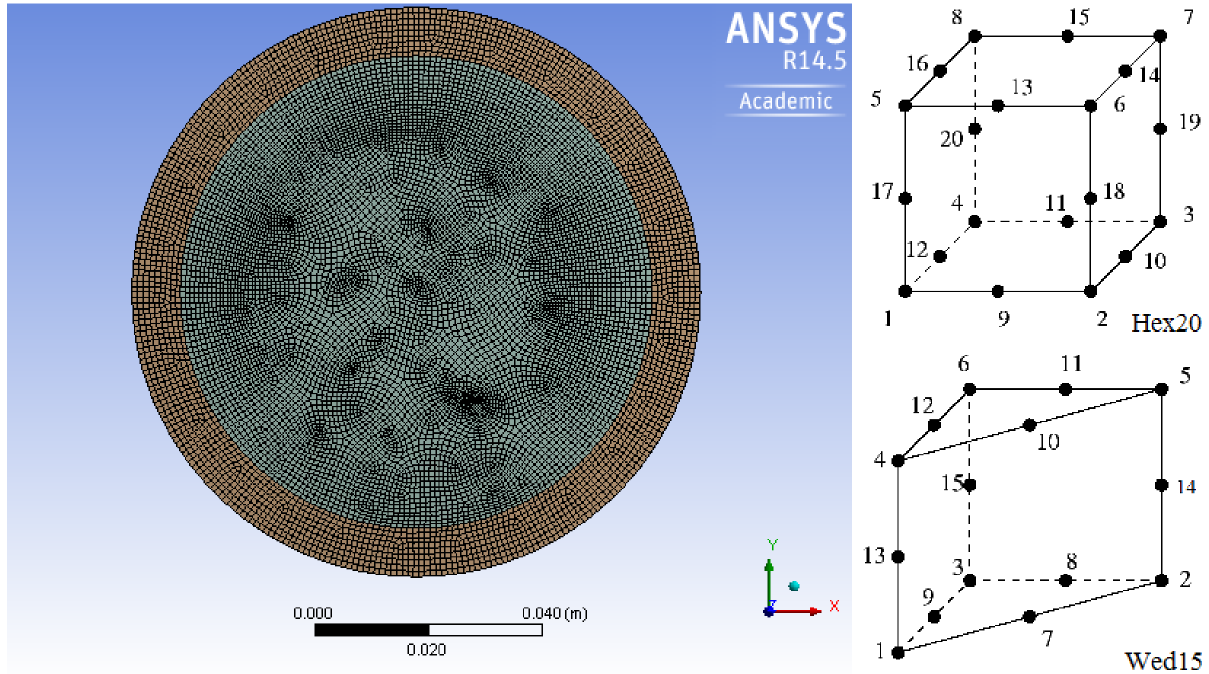

Figure 3.7: Left: FEM mesh of the complete coverage mask for the thermoelastic simulation; Right: details of the FEM elements used in the mesh.

Table 3.1: Overview of mesh sizes and properties.

Test Mask	Simulation Mode	Nodes [$\times10^3$]	Elements [$\times10^3$]	Max. Aspect Ratio
Complete Coverage	FVM (thermal)	1,586	1,421	84.6
	FEM (thermoelastic)	184	258	50.5
Center Block	FVM (thermal)	1,059	940	84.6
	FEM (thermoelastic)	422	638	54.8

Table 3.2: Thermal and mechanical material properties used in the simulations [67]

Material	Thickness (mm)	Density (kg/m^3)	Specific Heat (J/kg)	Thermal Conductivity (W/m/K)	Coefficient of Thermal Expansion (K^{-1})	Young's Modulus (GPa)	Poisson's Ratio
Aluminum	8	2719	871	202.4			
Polyimide	0.03	1420	1080	0.2	55.0e-6	2.5	0.34
Nickel	0.08	8900	460.6	91.7	13.4e-6	200	0.31
Helium	1.4	0.01652	5193	0.1507			
Stainless Steel	1.0 (steel ring) 5.0 (substrate holder)	7750	502.5	16.3	17.0e-6	193	0.31

3.2.2 Thermal Simulations

The time step for the transient simulation is set to be 12.5 msec, which is close to the calculated time step in Appendix C. The simulation flow time is 20 seconds. This corresponds to the typical duration from the start of the exposure process until the temperature distribution in the mask reaches a steady state, i.e. does not further increase from scan to scan. The initial temperature of the model is 18°C . Incident beam powers are selected from the experiments in Chapter 4, one for either test mask. The beam power density locally absorbed in the absorber or in the open areas of the polyimide membrane (in the case of the center block) as obtained from LEX-D is converted to an equivalent internal heat generation in the nickel absorber. The internal heat generation is implemented in ANSYS FLUENT® as a User Defined Function (UDF) program written in the program language C. The UDF program template is presented in Appendix E. The initial position of the synchrotron beam is assumed to be at the center of the mask. The helium gas flow enters the model from the bottom and from the vertical boundary planes of the model at a speed of 50 mm/s. This is also the scan speed with which the beam moves vertically up and down the model for a stroke length of 75 mm.

The time-resolved simulated temperatures at the positions where the five thermocouples are placed on the absorber surface in the corresponding experiments (see Figure 4.2 in Chapter 4) are presented for both test masks. #5 is in the center of the mask, #1 to #4 are at half radius, at 9, 12, 3, and 6 o'clock respectively. Furthermore, the local temperature distribution in the mask at the time when the maximum temperature is simulated in any one of the five thermocouple locations is shown. Due to the symmetricity of thermocouple installation, the simulated temperature distribution of thermocouple #2 in the top of the mask will be presented while thermocouple #4 in the bottom is neglected. Thermocouple #5 at the center of the mask is collinear with #1 and #3 in the horizontal direction, where the maximum temperature at these positions will appear at the same time.

A. Complete coverage mask

In the first simulation, a beam power of 16.86 W impinges onto the model (compare experimental test #6 for the complete coverage mask) representing the case of white-light exposure (without mirrors) at 233.2 mA electron current, 30 µm aluminum and 150 µm Kapton® X-ray pre-absorbers, and 25% open duty cycle of the chopper. This corresponds to a beam power of P_{beam} = 23,223 W/m^2. The simulated temperatures at the five thermocouples positions are presented in Figure 3.8. The temperature distribution after 19.0 seconds when the beam is located at the center of the mask and the maximum temperature appeared at the center thermocouple #5, and after 16.4 seconds when the beam is located at thermocouple #2, are presented in Figure 3.9 and Figure 3.10.

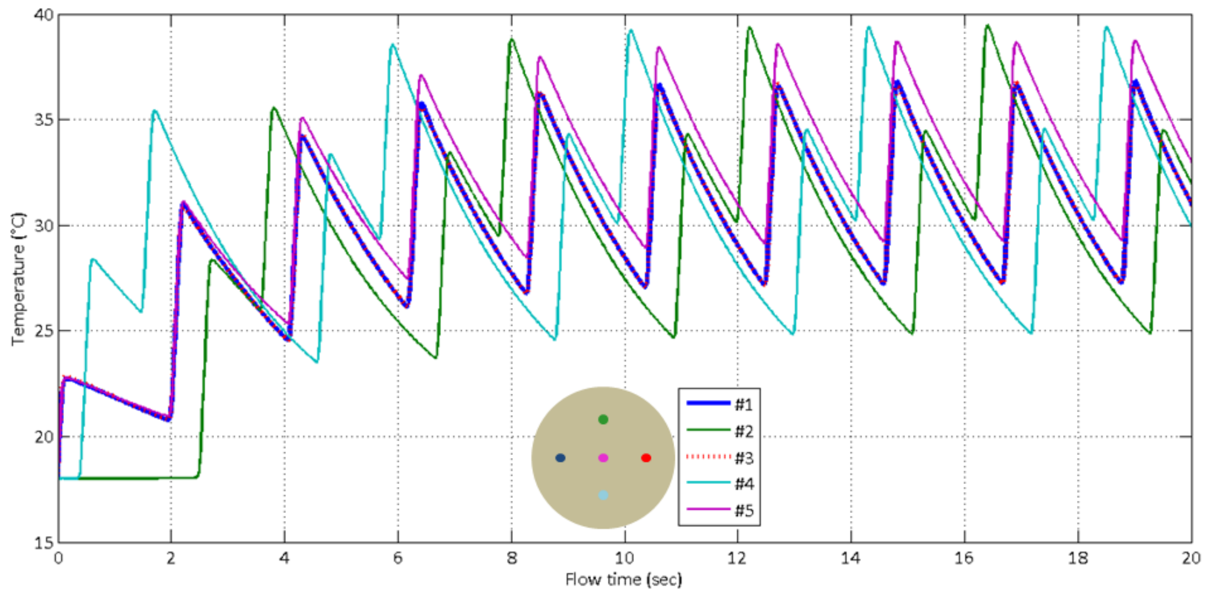

Figure 3.8: Simulated temperatures with respect to flow time at the locations where the five thermocouples are placed in the experiments for the complete coverage mask.

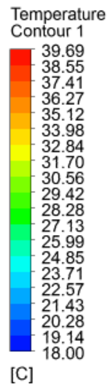

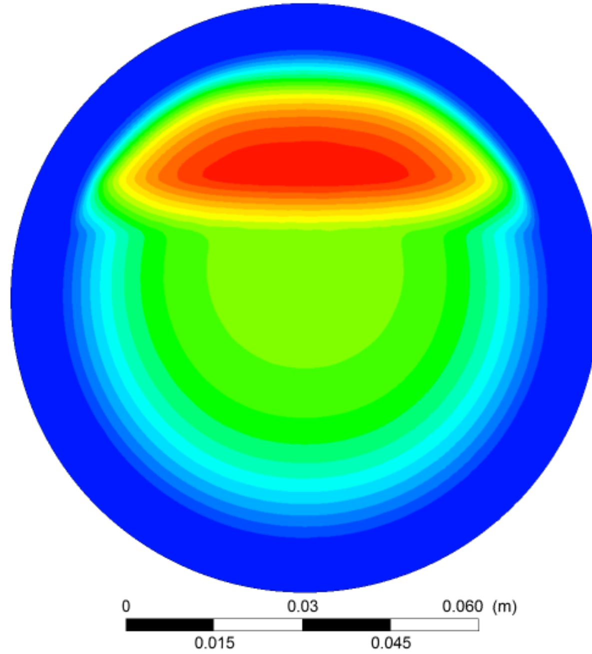

Figure 3.9: Simulated temperature distribution when the beam is at the location of the top thermocouple (#2) and the temperature reaches its highest values in that location. Simulation for the complete coverage mask.

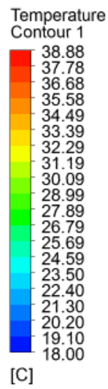

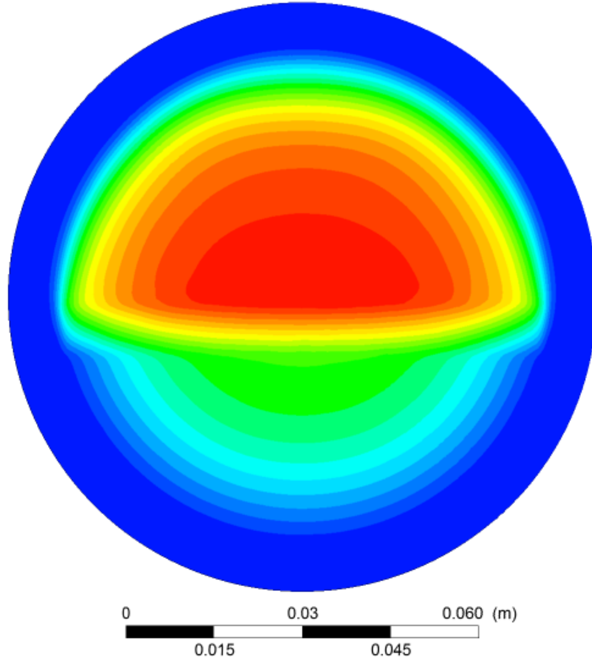

Figure 3.10: Simulated temperature distribution when the beam is at the location of the center thermocouple (#5) and the temperature reaches its highest values in that location. Simulation for the complete coverage mask.

B. Center block mask

In the second set of simulations, a beam power of 17.24 W impinges onto the model (compare experimental test #6 for the center block mask) representing the case of white-light exposure (without mirrors) at 238.4 mA electron current, 30 µm aluminum and 150 µm Kapton® X-ray pre-absorbers, and 25% open duty cycle of the chopper. This corresponds to a beam power of P_{beam} = 23,747 W/m^2. The simulated temperatures at the five thermocouples positions are presented in Figure 3.11. The temperature distribution after 19.0 seconds when the beam is located at the center of the mask and the maximum temperature appeared at the center thermocouple (#5), and after 16.4 seconds when the beam is located further up, at thermocouple #2, are presented in Figure 3.12 and Figure 3.13.

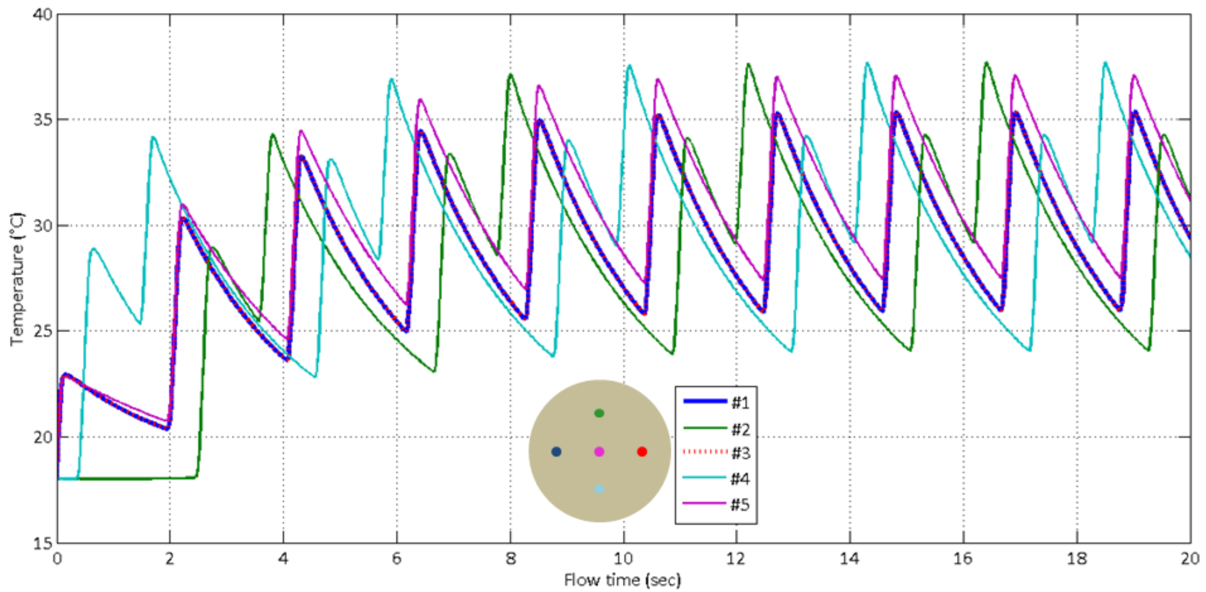

Figure 3.11: Simulated temperatures with respect to flow time at the locations where the five thermocouples are placed in the experiments for the center block mask.

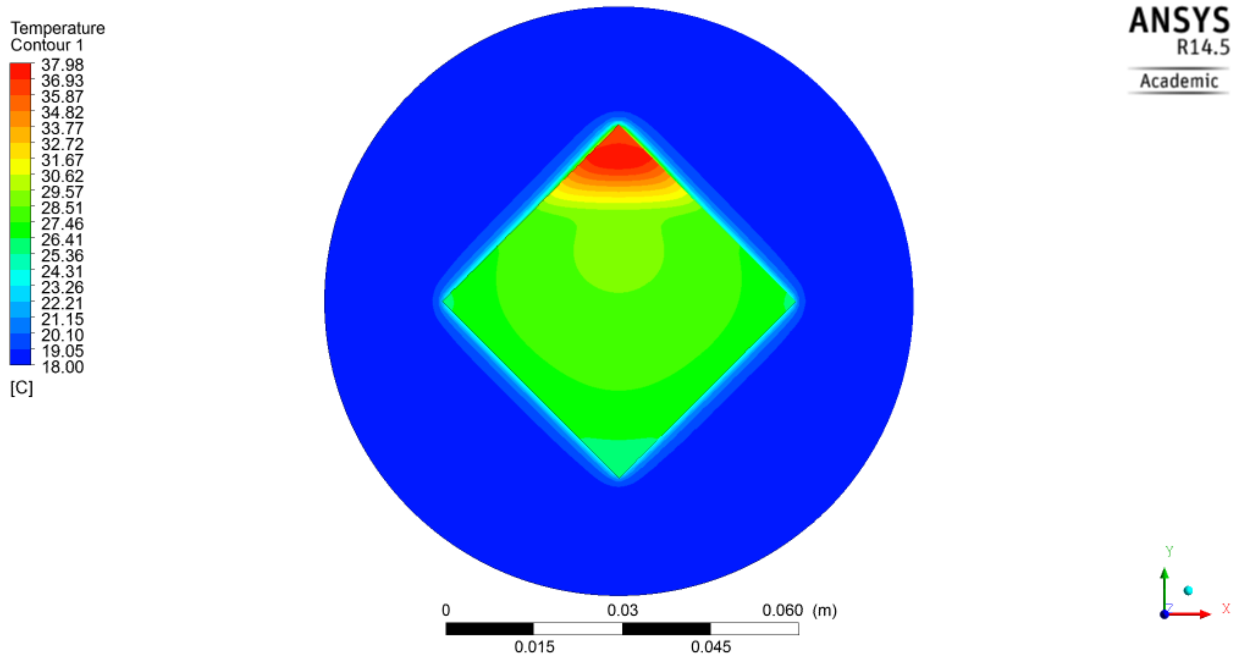

Figure 3.12: Simulated temperature distribution when the beam is at the location of the top thermocouple (#2) and the temperature reaches its highest values in that location. Simulation for the center block mask.

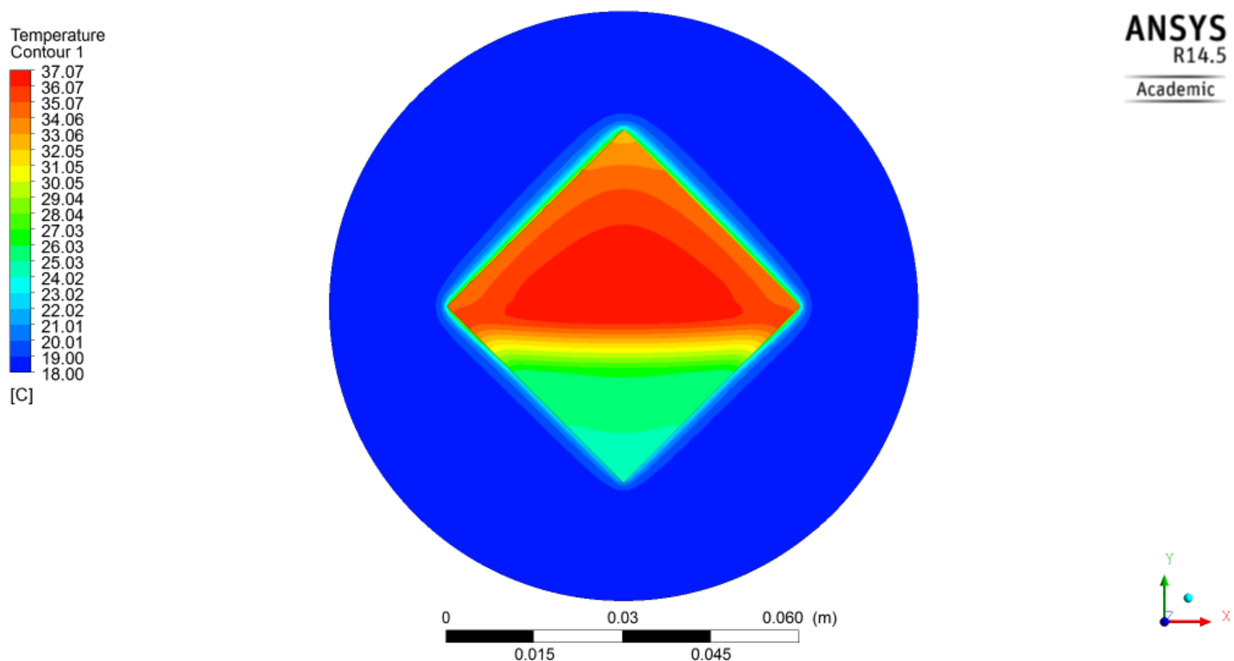

Figure 3.13: Simulated temperature distribution when the beam is at the location of the center thermocouple (#5) and the temperature reaches its highest values in that location. Simulation for the center block mask.

3.2.3 Thermoelastic Simulations

The temperature distributions in the test masks obtained from thermal simulations are transferred into the FEM models for thermoelastic simulations of temperature-induced thermal deformations and stress. The total deformation of the mask structure (the vector addition of deformations in the Cartesian coordinates), the deformations in each axis, and the equivalent stress are presented in Table 3.3.

Table 3.3: Maximum temperature at different thermocouple positions from thermal simulation

Mask	Thermocouple ID	Flow Time (sec)	Temperature (°C)
Complete Coverage	#2	16.4	39.46
	#5	19.0	38.75
Center Block	#2	16.4	37.71
	#5	19.0	37.07

A. Complete coverage mask

The thermoelastic simulation results for the complete coverage mask are presented in Figure 3.14 to Figure 3.18.

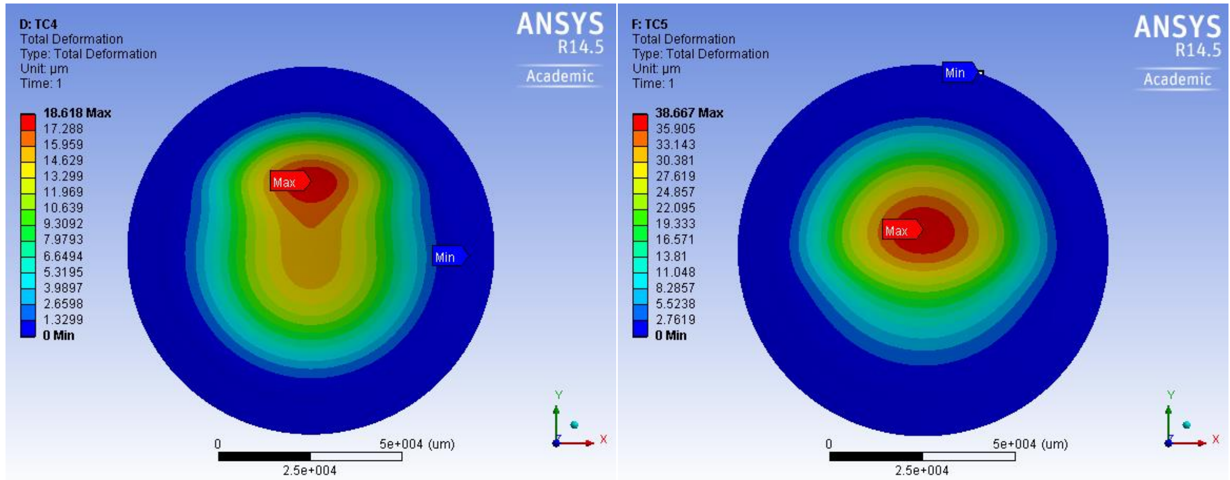

Figure 3.14: Simulated total (3-dimensional) deformations (in micrometers) for the complete coverage mask: Left: Deformations when the beam is at the location of the top thermocouple (#2); Right: Deformations when the beam is at the location of the center thermocouple (#5).

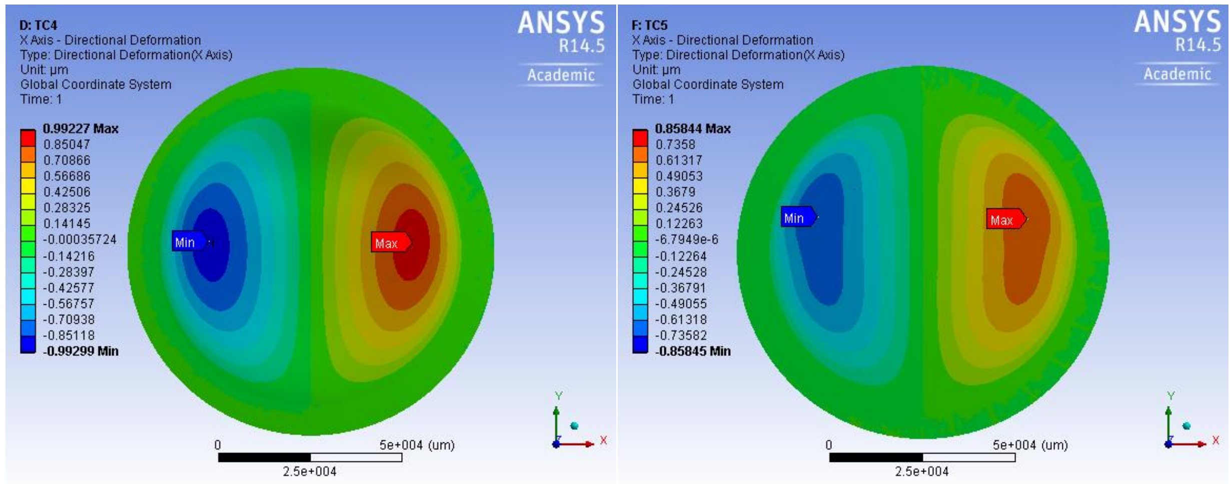

Figure 3.15: Simulated deformations (in micrometers) in the lateral plane along the *x*-axis (orthogonal to the incident synchrotron beam) for the complete coverage mask: Left: Deformations when the beam is at the location of the top thermocouple (#2); Right: Deformations when the beam is at the location of the center thermocouple (#5).

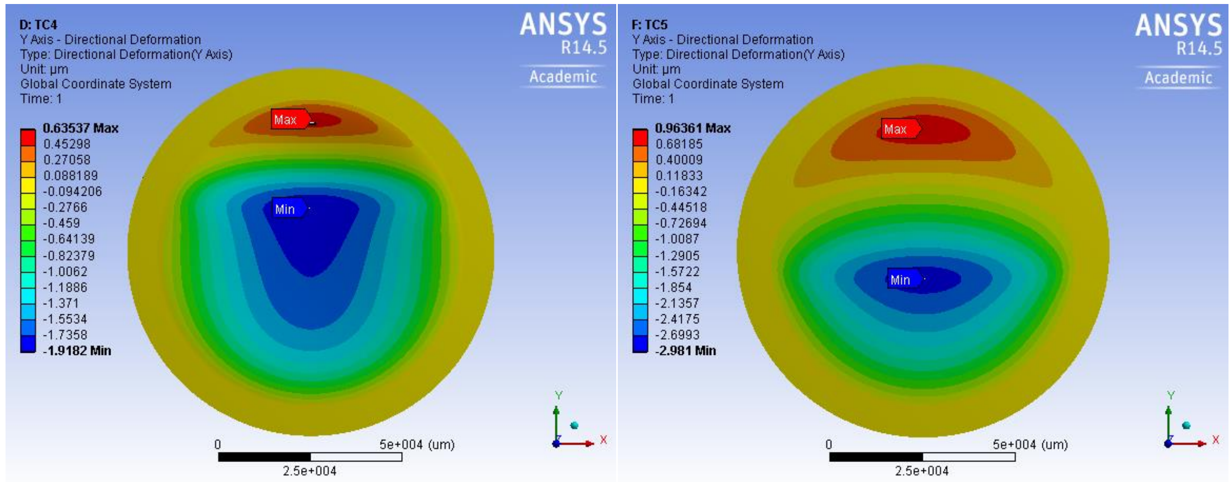

Figure 3.16: Simulated deformations (in micrometers) in the lateral plane along the *y*-axis (orthogonal to the incident synchrotron beam) for the complete coverage mask: Left: Deformations when the beam is at the location of the top thermocouple (#2); Right: Deformations when the beam is at the location of the center thermocouple (#5).

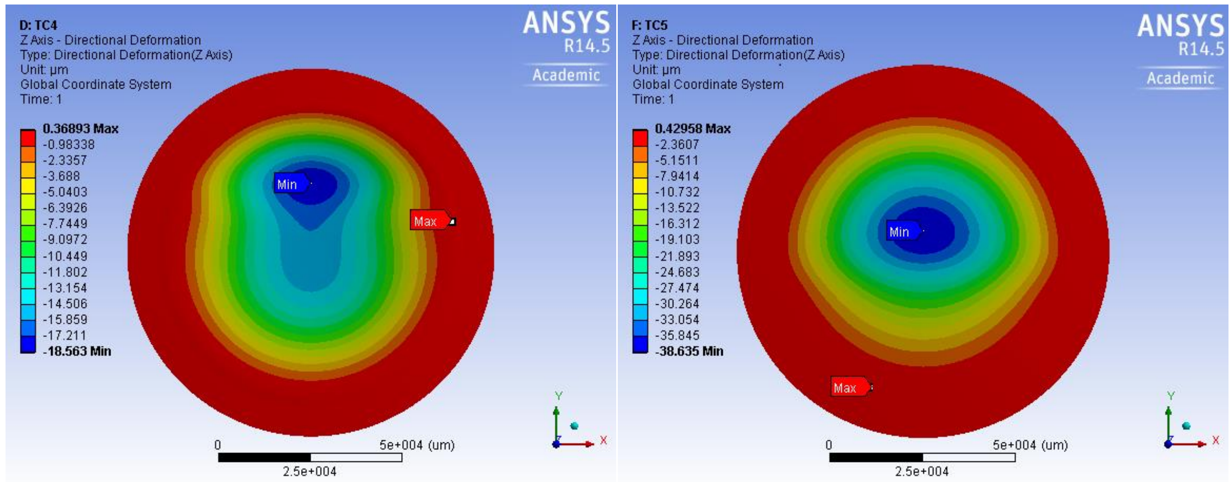

Figure 3.17: Simulated deformations (in micrometers) along the *z*-axis (along the beam direction, orthogonal to the lateral plane) for the complete coverage mask: Left: Deformations when the beam is at the location of the top thermocouple (#2); Right: Deformations when the beam is at the location of the center thermocouple (#5).

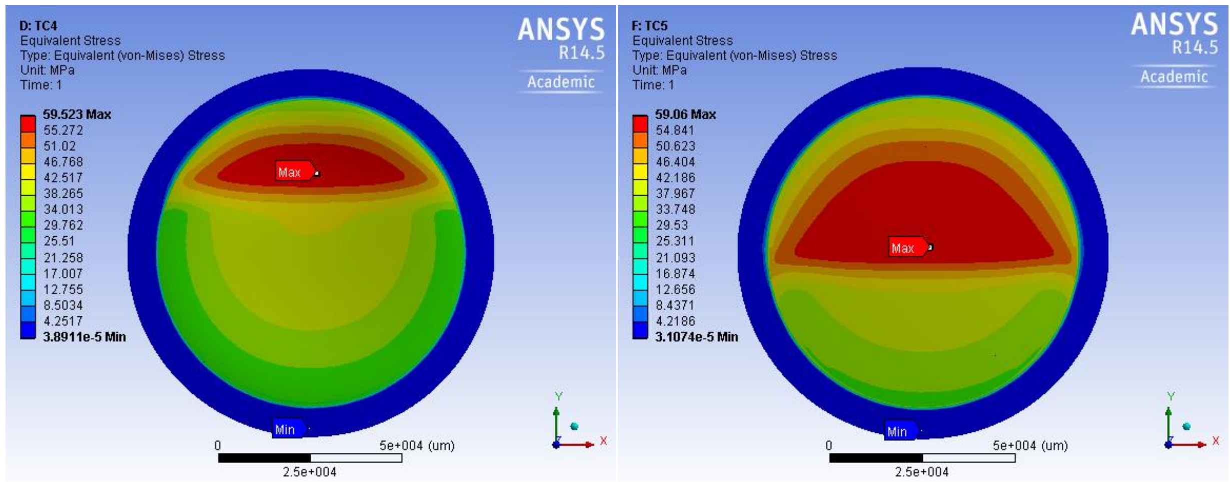

Figure 3.18: Simulated equivalent stress distributions (in MPa) for the complete coverage mask: Left: Deformations when the beam is at the location of the top thermocouple (#2); Right: Deformations when the beam is at the location of the center thermocouple (#5).

B. Center block mask

The thermoelastic simulation results for the center block mask are presented in Figure 3.19 to Figure 3.23.

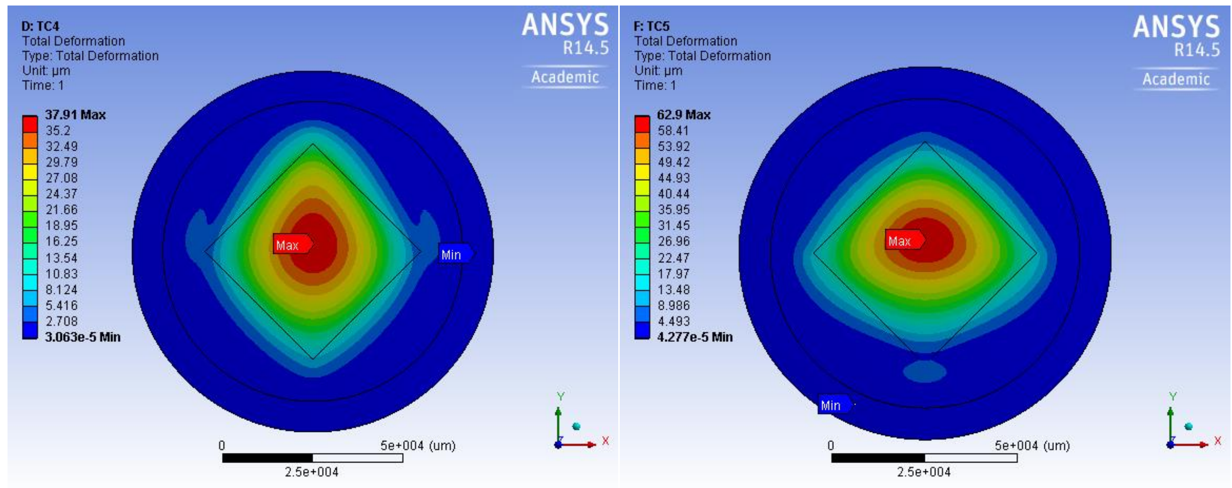

Figure 3.19: Simulated total (3-dimensional) deformations distributions (in micrometers) for the center block mask: Left: Deformations when the beam is at the location of the top thermocouple (#2); Right: Deformations when the beam is at the location of the center thermocouple (#5).

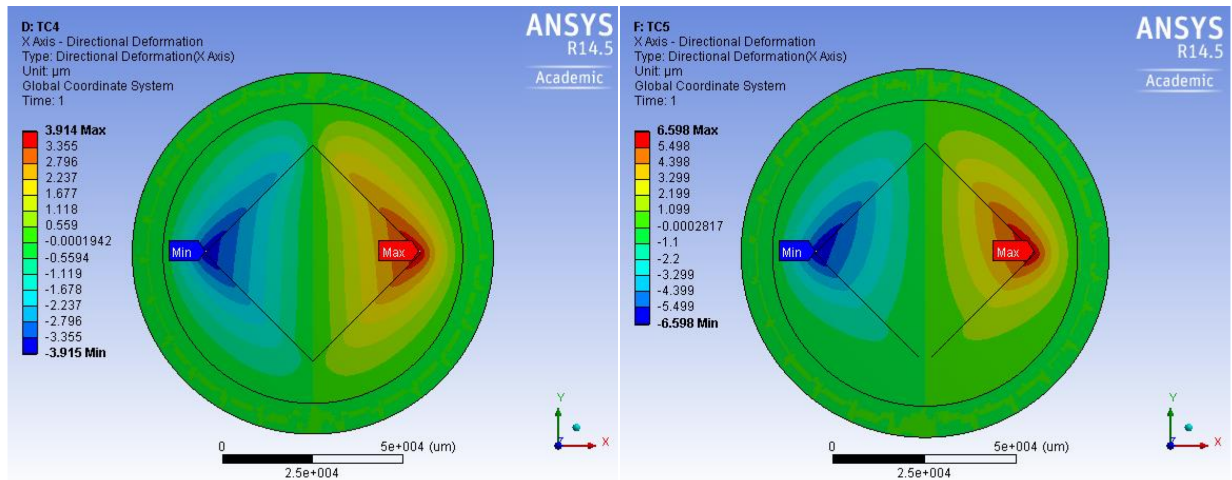

Figure 3.20: Simulated deformations (in micrometers) along the *x*-axis (orthogonal to the incident synchrotron beam) for the center block mask: Left: Deformations when the beam is at the location of the top thermocouple (#2); Right: Deformations when the beam is at the location of the center thermocouple (#5).

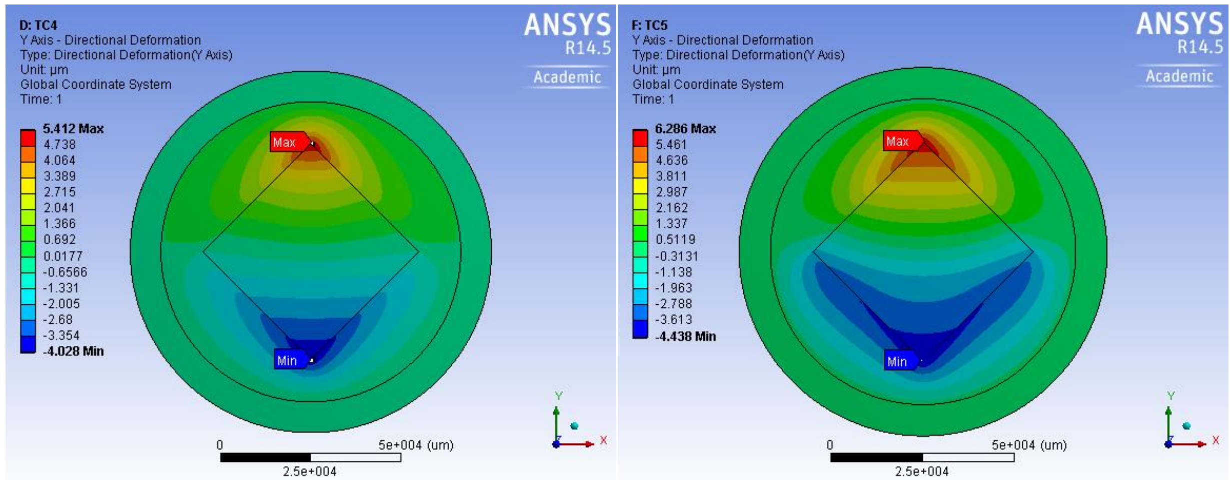

Figure 3.21: Simulated deformations (in micrometers) along the *y*-axis (orthogonal to the incident synchrotron beam) for the center block mask: Left: Deformations when the beam is at the location of the top thermocouple (#2); Right: Deformations when the beam is at the location of the center thermocouple (#5).

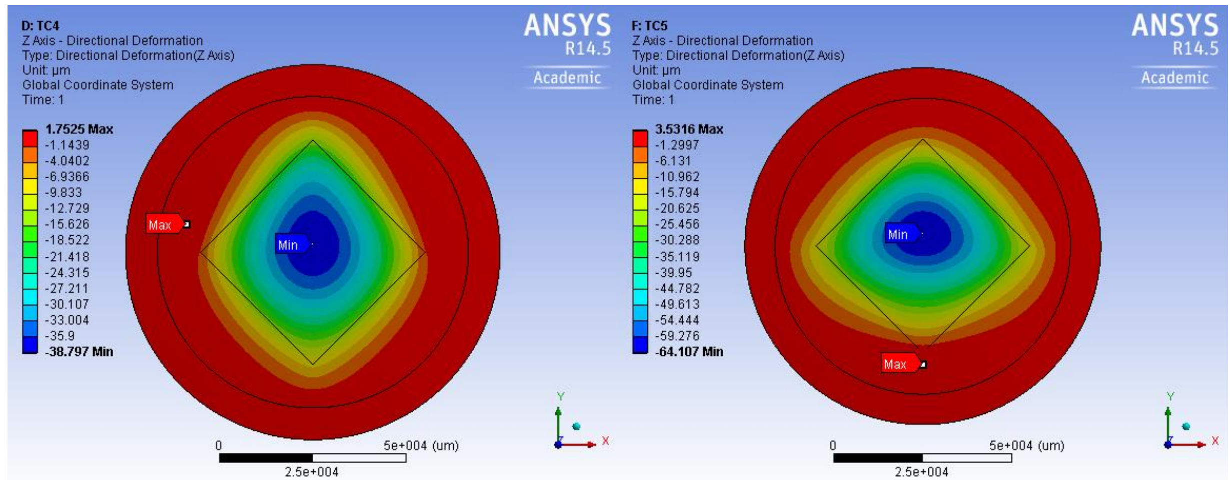

Figure 3.22: Simulated deformations (in micrometers) along the *z*-axis (along the beam direction, orthogonal to the lateral plane) for the center block mask: Left: Deformations when the beam is at the location of the top thermocouple (#2); Right: Deformations when the beam is at the location of the center thermocouple (#5).

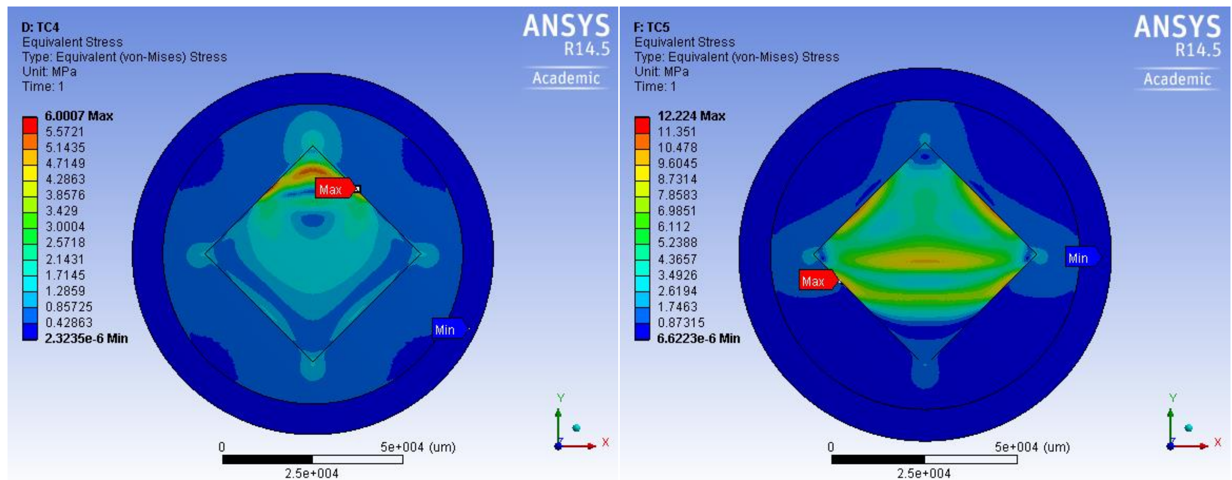

Figure 3.23: Simulated equivalent stress distributions (in MPa) for the center block mask: Left: Deformations when the beam is at the location of the top thermocouple (#2); Right: Deformations when the beam is at the location of the center thermocouple (#5).

3.3 Discussion

The results for the temperature distribution at the five thermocouple positions as a function of time (Figure 3.8 and Figure 3.11) show that after three full scans, the steady state temperatures are reached and further increase from scan to scan is at best minimal. Whenever the beam passes a simulated spot, the temperature increases immediately, and slowly decreases due to heat transfer to the cooled parts, until the beam exposes the same area again, in the next scan. The three locations across the half-height line of the mask (thermocouples #1, #3, and #5) show a series of identical temperature changes. The top thermocouple (#2) reaches its highest value shortly before the center ones, the bottom thermocouple (#4) shortly after the center one (#5). The temperature patterns for the top and bottom location are not identical for each spot. The fact that close to the top or bottom, the reverse point of the scan is close, two temperature rises are shortly separated in space, followed by a relatively longer cooling period until the beam scanned all the way back. Due to the double-exposure without much dwell in between, the top and the bottom thermocouples reach the highest temperature in the models. The center thermocouple (#5) location gets hotter than the ones on the sides at half height since the path to the cooled scanner components on the outer rim of the mask is farther away: Overall, the highest temperature during exposure of about 37°C to 40°C does not appear at the center of the mask, but at the two symmetrical positions at the top and bottom of the mask where thermocouples #2 and #4 are installed. This is because the scanning speed is faster than the heat dissipation speed, which leads to a distinct boundary between the exposed and unexposed area during the scanning process. The slow heat dissipation also explains the overlap of the temperature distribution

profile and the equivalent stress profile in the complete coverage mask (compare Figure 3.9, Figure 3.10, and Figure 3.18), which the accumulation of local heat causes larger local deformations.

The temperature distribution strongly depends on the position of synchrotron beam. Figure 3.9, Figure 3.10, Figure 3.12, and Figure 3.13 indicate the maximum temperature rises at the line that represents the current position of the beam. In all the figures here, the beam is scanning downwards, as can be seen from the comparatively cool area below the current beam position, and the slowly decreasing temperature above. The temperature distribution also depends on the absorber layout: the heat dissipation of the center block is through conduction across the proximity gap, while the energy deposited in the absorber of the complete coverage mask can also be laterally transferred through the metal absorber to the mask frame by thermal conduction. In the second case, heat transfer across the polyimide membrane to the steel ring acts as a thermal barrier. Besides, the increased heat transfer capability is counteracted by the fact that more heat is absorbed in this complete coverage absorber. Ultimately, both masks lead to similar maximum temperatures.

This might change if conduction across the proximity gap becomes less effective. During actual exposures, silicon wafers are coated with resists that also feature low thermal conductivity, such that the resist surface temperature will increase instead of the constant temperature modeled here in the substrate holder. On the upside, though, would a typical proximity gap would be 100 μm rather than 1.4 mm (which had to be chosen to accommodate thermocouples in the actual experiments), which would enhance the cooling effectiveness across the proximity gap significantly.

The total deformations in the test masks are mostly attributed to the axial deformations in the z-axis. The deformations in the lateral plane for complete coverage mask are approximately 6% of the deformations in the axial direction: up to 2 μm along the x-axis (see Figure 3.15) and 4 μm along the y-axis (see Figure 3.16). The deformations in the lateral plane for center black mask are approximately 20% of the deformations in the axial direction: up to 13 μm along the x-axis (see Figure 3.20) and 10 μm along the y-axis (see Figure 3.21). The axial direction deformation needs to be controlled within the distance of the proximity gap, so the absorber structures will not contact with the photoresist.

The thermal deformations in the test masks are affected by two factors. First, the thermal expansion coefficient is much higher for polyimide than it is for nickel, which leads to stronger expansion in the mask membrane compared to the absorber structure at a given temperature. Secondly, temperatures are even anticipated to increase: the thermal conductivity of polyimide is much lower than that of other potential materials for mask membranes, i.e. ceramics and metals. The heat dissipation by thermal conduction to the mask frame therefore is less efficient for a polyimide membrane, which often causes a relatively higher temperature in large isolated absorber structures. Although the temperature rise in the center block mask is lower than in the complete coverage mask, the deformations in all directions are larger in the center block

mask. This is because the modulus of polyimide is much lower than for nickel, such that the polyimide membrane around the center absorber can more easily get distorted. Considering that typical mask layouts will rarely feature large areas without structural support from mask absorbers, the complete coverage mask should better represent the thermal deformations.

The deformation in the complete coverage mask is determined by the temperature distribution in the mask since there is no lateral variation in material composition. During the exposure, the maximum deformation moves along with the synchrotron beam (see Figure 3.14). As the steel ring constrains the mask in the lateral plane, the deformation of the mask structure will be afferent, forming a spherical deflection out of the lateral plane in axial direction (z-axis) (see Figure 3.22). This out-of-plane deformation along the beam direction is up to about 20 μm for a scan position close to the top (see Figure 3.17, left), and can add up to about 40 μm for a central scan position (see Figure 3.17, right) which constitutes a worst case of thermal deformation. Such deformations along the beam direction are not necessarily problematic since the angle between the lateral plane and the deflected membrane are still extremely small. This way, no adverse impact of tilted mask absorber could be occurring. More problematic would be deformations within the lateral plane. They are limited, though, to only 2 μm along the x-axis (see Figure 3.15) and 3 μm along the y-axis (see Figure 3.16). Furthermore, as the beam scans reciprocally in the vertical direction, the deformation in horizontal direction is symmetric (see Figure 3.15), while the deformation in vertical direction depends on the position of synchrotron beam (see Figure 3.16).

The deformation in the center block mask depends on the temperature distribution, as similar results are obtained compared with complete coverage mask. An additional effect, though, is that the outline of the absorber structures coincides with sharp changes of the temperature, comparable to the temperature change at the mask rim in the case of the complete coverage mask. Furthermore, the mechanical properties change significantly at the absorber edges and corners, causing local stress concentrations, so that these structures can be detected in stress, strain and deformation plots even when there are limited temperature gradients driving thermal stress (see Figure 3.23). To provide a schematic overview, the layout of the center block absorber can be represented by a 5×5 grid, where local deformations at each point in the grid are presented to get a better understanding (see Figure 3.24).

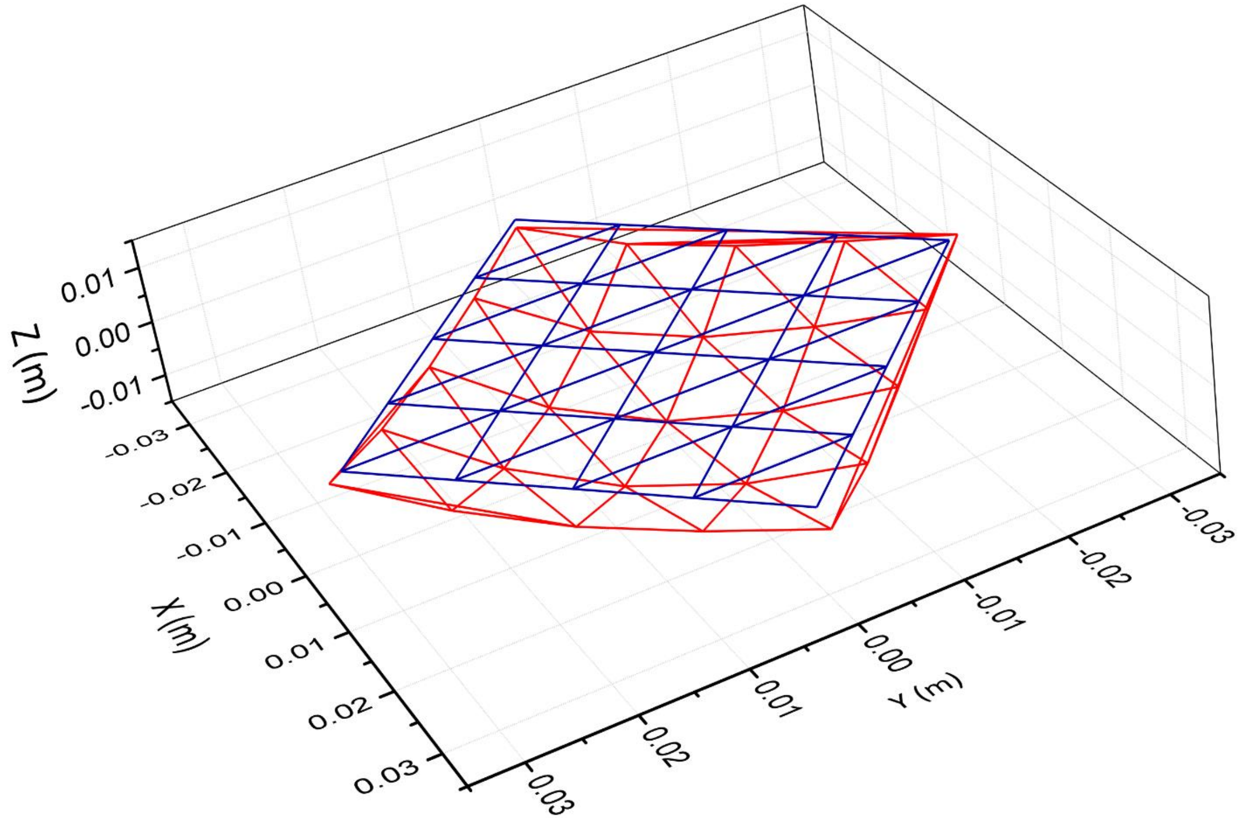

Figure 3.24: 3D schematic of the center block absorber deformation when the beam is at the location of the center thermocouple (#5): Blue: original absorber layout; Red: deformed absorber layout (deformation scaled by 200).

To quantify the effect of the intensity chopper, the temperature in the complete coverage mask has been simulated again at the same conditions as before, but without the 25% open duty cycle intensity chopper. This means that in this case, the incident beam power is four times higher than before: With chopper, the temperature increased by 22°C from 18°C to about 40°C. Without an intensity chopper, the increase in temperature reflects the increase in power and now is about four times higher, by 83°C from 18°C to 101°C (see Figure 3.25). In this case, the thermal deformations of the mask are increased to four times of the value observed at 25% duty cycle (see Figure 3.26). The deformation in the axial direction is about 160 μm, which is far beyond the standard proximity gap of 100 μm and would lead to direct contact between the mask and resist during exposure. This result suggests that without the intensity chopper, polyimide X-ray masks would not be applicable at SyLMAND.

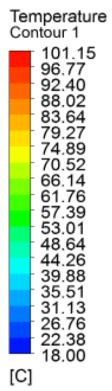

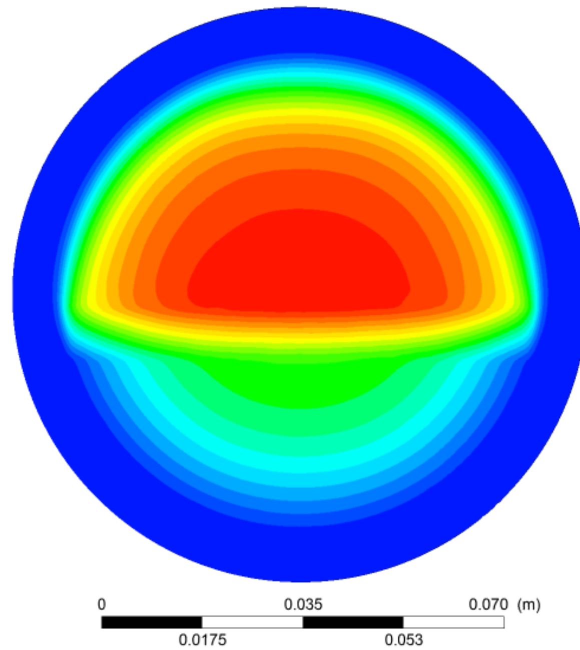

Figure 3.25: Simulated temperature distribution after 19.0 seconds when the beam is at the location of the center thermocouple (#5) and the temperature reaches its highest values in that location. Simulation for the complete coverage mask, exposure without intensity chopper implementation.

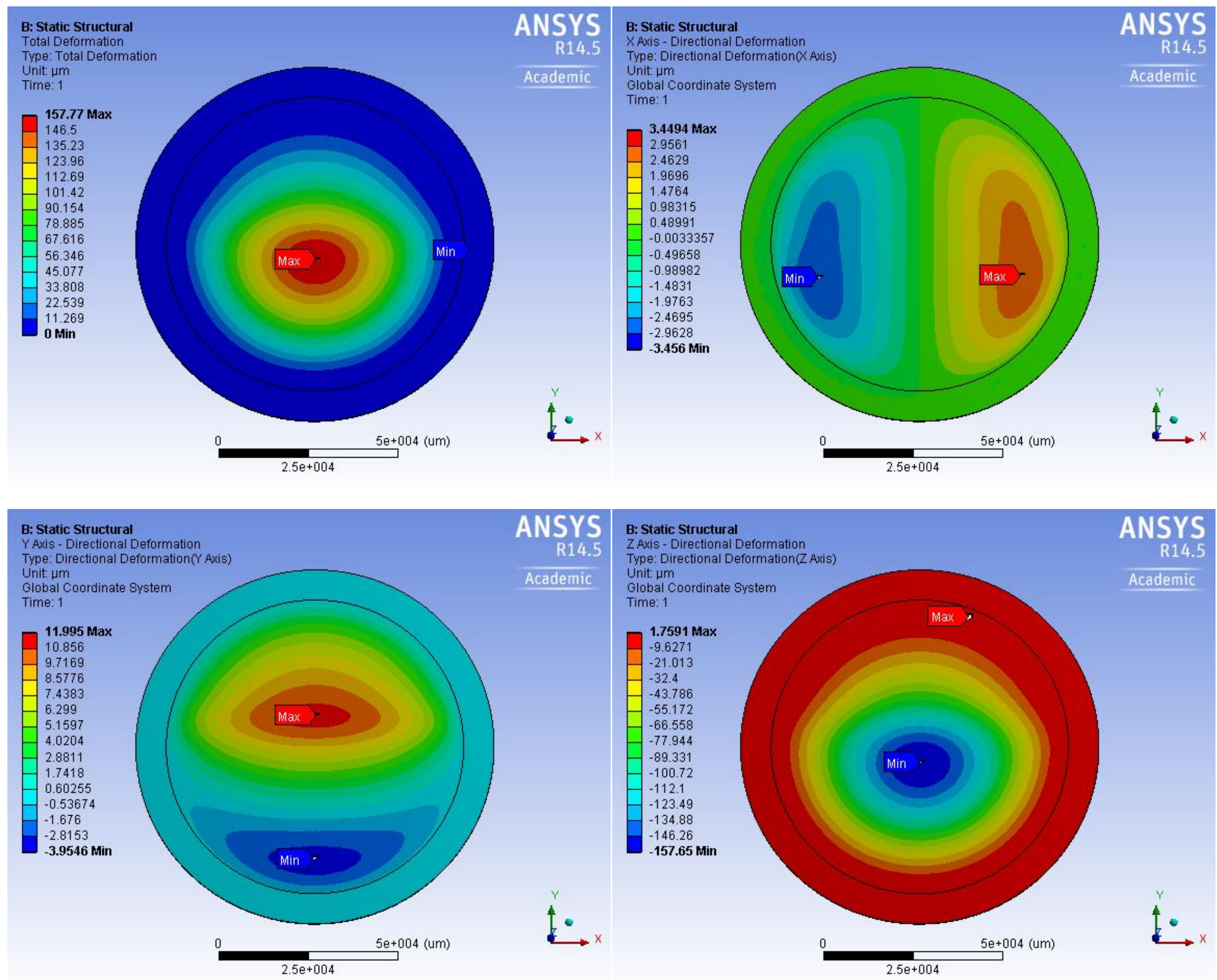

Figure 3.26: Simulated deformations (in micrometers) for the complete coverage mask, exposure without intensity chopper implementation: Upper Left: Total deformation; Upper Right: Deformation along the *x*-axis; Lower Left: Deformation along the *y*-axis; Lower Right: Deformation along the *z*-axis.

3.4 Chapter Summary

In this chapter, a consistent numerical model was developed based on the FVM and the FEM. The software package ANSYS R14.5 was used for a two-stepped approach: The temperature distributions in the test masks during were simulated with the FVM based fluid dynamics module ANSYS FLUENT® for each time step of the considered scanning processes. Based on the obtained temperature distribution, the thermoelastic stress and deformations were determined by ANSYS Mechanical® using the FEM. One case considered for either mask, with input data calculated in the software LEX-D. Discussions of simulation results focused on the maximum temperature rises obtained for those locations that were later experimentally verified by five thermocouples on the mask. The results show that, for the load cases considered, both masks reach comparable maximum temperatures of about 37°C to 40°C. The highest

temperatures are not observed at the exact center of the mask, but rather off towards the top or bottom where there is less time to cool back down between two subsequent X-ray exposures during the scan process. The resulting thermal deformations in the test masks are largest in the axial direction along the incident beam. In the lateral plane, however, the deformations for the complete coverage mask are only approximately 6% of the deformations in axial direction and amount to 2 μm along the *x*-axis and 4 μm along the *y*-axis. The deformations in the lateral plane for center black mask are approximately 20% of the deformations in axial direction: Up to 13 μm along the *x*-axis, and 10 μm along the *y*-axis. The intensity chopper was proven to reduce the head load proportionally to its open duty cycle, i.e. ¼ of the temperature rise at 25% duty cycle with respect to full beam power. This is critical for maintaining acceptable temperature rises, and therefore deformations, during DXRL exposures as discussed in Chapter 5.

CHAPTER 4

THERMAL MEASUREMENTS OF POLYIMIDE MEMBRANE MASKS AND VERIFICATION OF THERMAL SIMULATIONS

4.1 Experimental Design and Setup

4.1.1 Properties of the Synchrotron Beam

The geometry of the synchrotron beam can be adjusted by slits in the beamline and apertures in the scanner. The beamline slits are set to 7 mm in height, basically admitting the entire beam. At the scanner, the vertical aperture is set to 100 mm so the entire mask can get exposed when scanned through the beam. At the sample location, the effective vertical beam height was measured with X-ray sensitive paper to be approximately 8.8 mm according to the vertical opening angle of 0.52 mrad [46]. Horizontally, the beam is collimated to 83 mm in the scanner just upstream the mask frame. This allows to expose the entire exposable area of the test masks, which is 83 mm in diameter.

The beam profiles can be studied by fly-wire photocurrent detection systems in the double mirror system [46]. Figure 4.1 shows the vertical beam profile at the mirror entrance with about 7 mm beam height (between 16.8 mm and 23.8 mm relative height in this graph), exhibiting a Gaussian distribution.

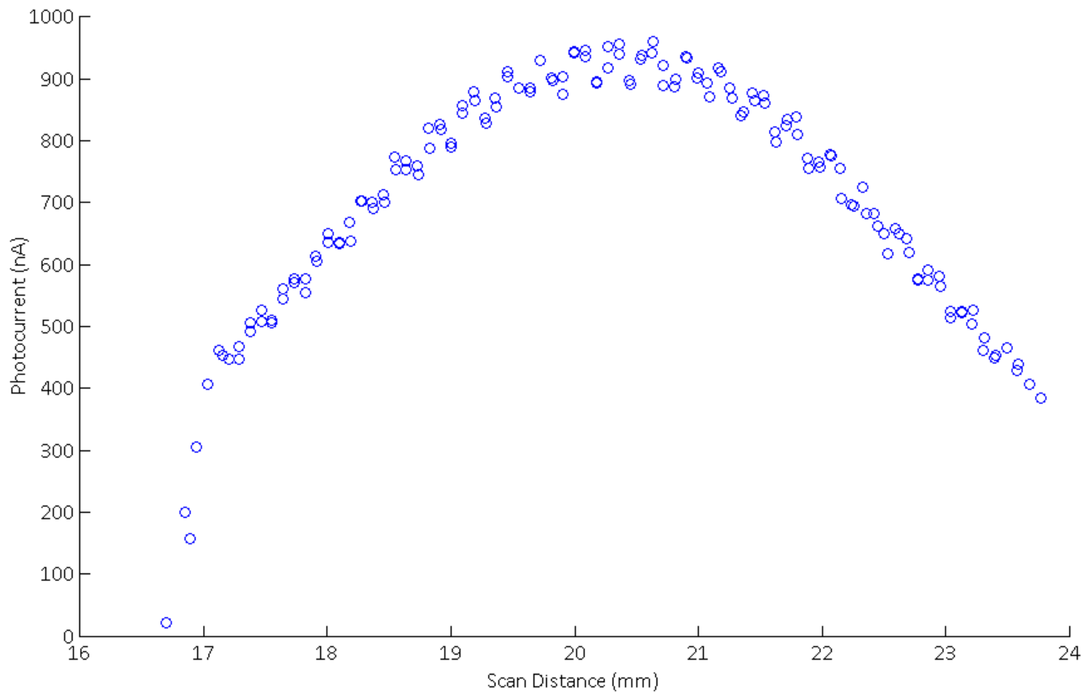

Figure 4.1: Vertical beam profile scanned with the fly-wire photocurrent measurement system at the mirror entrance. The beam is collimated to 7 mm using the upstream slits.

During the experiments, the intensity chopper is usually set to 25% open duty cycle, i.e. it cuts 75% of the original beam power. The mirrors are retracted such that they do not modify the spectral or power distribution. In the scanner, pre-absorbers are installed to further decrease the incident beam power: 30 μm aluminum and 150 μm Kapton®. The exposures take place at a stored electron current of about 220 mA.

4.1.2 Exposure Parameters

Test exposures can be fairly short as thermal equilibrium is reached for less than 1 minute. The scanner was programmed with dose expenditures equivalent to around three-minute exposure time.

With the beamline parameters kept constant, the only remaining variable impacting the incident beam power is the stored electron current. The current decays quasi-exponentially. To calculate the incident beam power and relate the experimental results to this beam power, the actual beam current must therefore be recorded for every test exposure.

To investigate the temperature of the test masks as a function of the beam power with otherwise constant conditions, the experiments are repeated for various beam currents. Besides, the intensity chopper is applied to reduce the beam power (or simulate much smaller beam currents) during some tests, with settings of both 10% and 25% open duty cycle.

All experiments are done at a scan speed of 50 mm/s with a scan height of 75 mm. Before and after each scan stroke, the scanner stage accelerates or decelerates at 400 mm/s^2.

Photoresist and silicon wafer are not loaded in the scanner during the experiments. The reason is that only a limited distance is available between the mask plane and the substrate holder. Almost the entire allowance is used up by the proximity gap to accommodate the thermocouples. Further elements, such as a sample silicon wafer with resist, cannot be added. During the experiments, the bare substrate holder therefore faces the mask.

4.1.3 Experimental Setup with Thermocouples

In this study, the temperature is measured by thermocouples that are placed behind mask absorbers to protect them from direct synchrotron exposure and related unwanted additional heating due to absorption of radiation. The thermocouples are brought in close thermal contact with the mask absorbers by pressing them against the absorbers using self-adhesive Kapton® tape. The 1 m-long American Wire Gauge 40, PFA-coated wires are protected from synchrotron exposure by mask absorbers or a small nickel extension from the center absorber to the mask frame in the case of the center block mask. The thermocouples used in the experiment are chromel/alumel (K-type) 5SC-TT-K-40-36 from Omega Engineering (Stamford, CT, USA). The thermocouples have a wire diameter of 76 μm.

Five thermocouples are used to measure the temperature rise in the exposed area of the test masks. They are placed at the center (#5) and at half distance of the mask radius in both, vertical and horizontal directions (#1-#4, ordered in a clock-wise, with #2 at the top). Figure 4.2 illustrates the positions.

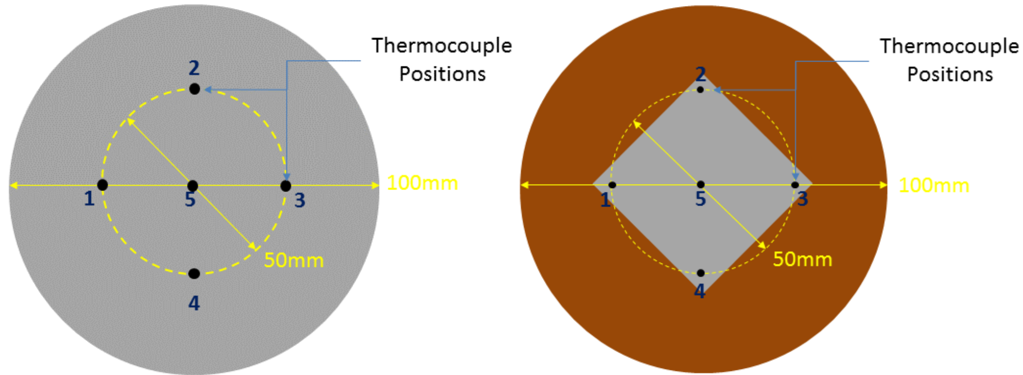

Figure 4.2: Schematics of the positioning of the five thermocouples on the test masks. Left: Complete coverage mask; Right: Center block mask.

The thermocouples are connected to a data acquisition device through a small flange DN40 vacuum port on the wall of the scanner working chamber. The sampling frequency is 8 Hz for the measurement.

Figure 4.3 and Figure 4.4 show the experimental setup, consisting of the test masks mounted in the mask holder of the scanner, as well as five thermocouples mounted to the mask absorbers.

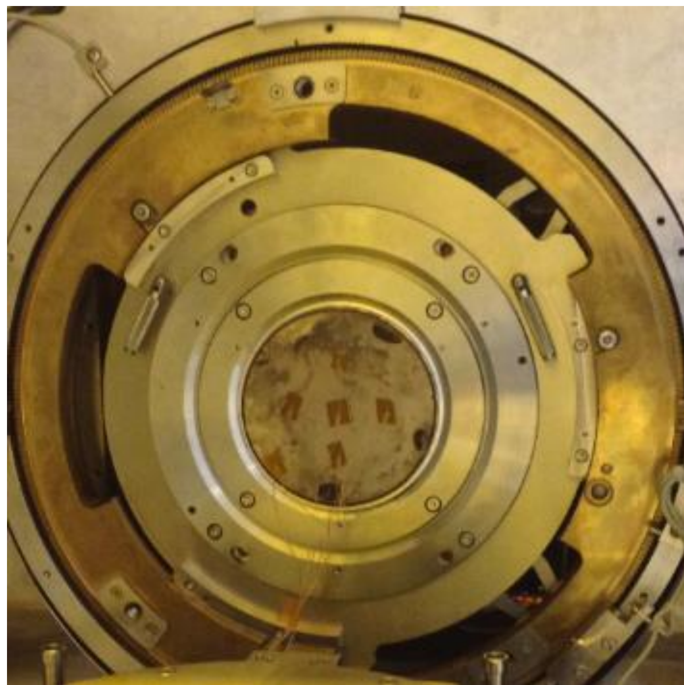

Figure 4.3: Experimental setup of the complete coverage mask, mask holder, scanner adapter, and five thermocouples.

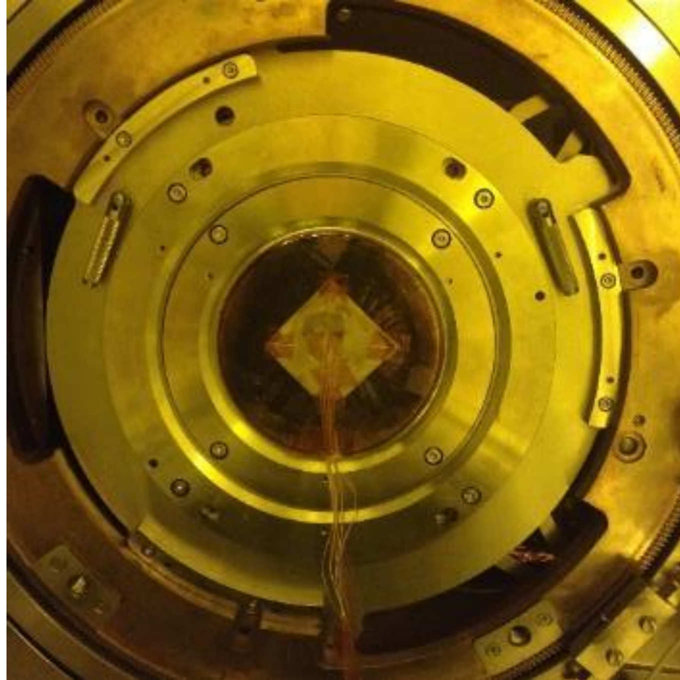

Figure 4.4: Experimental setup of the center block mask, mask holder, scanner adapter, and five thermocouples.

4.2 Experimental Results

The temperatures of the thermocouples mounted onto the test masks are measured under different exposure conditions. During a specific experiment, the incident beam power linearly decreases with the decaying electron current. A typical exposure lasts for a few minutes. During this time, the current typically decays by less than 0.1%. The arithmetic average of the beam currents at beginning and end of the exposure is therefore used to represent the beam condition for each test with sufficient precision. The incident beam power density for each case is calculated by the LEX-D software. In this way, the incident beam power across the exposed area of 83 mm by 8.8 mm can be calculated for comparison of the experimental results with the numerical simulations of comparable cases.

Detailed measurement results are presented in Appendix F. Key results are listed below. Table 4.1 and Table 4.3 summarize the actual exposure conditions for each experiment, including the calculated incident beam power. Table 4.2 and Table 4.4 extract the highest temperatures that occurred for each experiment at each thermocouple.

4.2.1 Test Results for the Complete Coverage Mask

Table 4.1: Exposure parameters for the complete coverage mask.

Test #	Beam Current (mA)	Incident Beam Power (W) calculated by LEX-D	Pre-absorbers Insertion (30 µm Al, 150 µm Kapton)	Intensity Chopper Open Duty Cycle
1	218.5	6.32	Y	10%
2	235.5	11.91	N	10%
3	178.2	12.89	Y	25%
4	202.6	14.65	Y	25%
5	219.6	15.88	Y	25%
6	233.2	16.86	Y	25%
7	222.3	28.10	N	25%

Table 4.2: Maximum temperatures measured by thermocouples on the complete coverage mask.

Test #	Incident Beam Power (W) calculated by LEX-D	Maximum Temperature of #1 (°C)	Maximum Temperature of #2 (°C)	Maximum Temperature of #3 (°C)	Maximum Temperature of #4 (°C)	Maximum Temperature of #5 (°C)
1	6.32	23.30	23.02	22.08	24.52	23.59
2	11.91	27.05	26.90	25.24	30.18	28.04
3	12.89	27.86	27.80	26.07	31.36	28.78
4	14.65	29.92	30.72	28.54	33.72	30.97
5	15.88	30.08	30.09	27.77	34.23	30.87
6	16.86	31.78	32.65	31.33	35.82	32.67
7	28.10	38.47	38.43	34.35	46.57	40.86

4.2.2 Test Results for the Center Block Mask

Table 4.3: Exposure parameters for the center block mask.

Test #	Beam Current (mA)	Incident Beam Power (W) calculated by LEX-D	Pre-absorbers Insertion (30 µm Al, 150 µm Kapton)	Intensity Chopper Open Duty Cycle
1	214.3	6.20	Y	10%
2	210.6	10.65	N	10%
3	182.6	13.13	Y	25%
4	188.8	13.65	Y	25%
5	206.2	14.91	Y	25%
6	238.4	17.24	Y	25%
7	207.7	26.25	N	25%

Table 4.4: Maximum temperatures measured by thermocouples on the center block mask.

Test #	Incident Beam Power (W) calculated by LEX-D	Maximum Temperature of #1 (°C)	Maximum Temperature of #2 (°C)	Maximum Temperature of #3 (°C)	Maximum Temperature of #4 (°C)	Maximum Temperature of #5 (°C)
1	6.20	23.07	22.46	22.88	24.46	24.29
2	10.65	26.19	25.06	25.69	28.51	28.12
3	13.13	28.13	27.22	27.61	30.61	30.03
4	13.65	28.88	27.43	28.79	31.83	30.48
5	14.91	29.45	28.33	28.76	32.36	31.80
6	17.24	31.81	29.87	31.24	34.79	33.90
7	26.25	37.91	35.81	36.76	42.89	42.18

4.3 Interpolation of the Temperature Rise as a Function of the Incident Beam Power

To generalize the results of the thermal study, the dependency of relevant temperatures is derived as a function of the incident beam power. Subsequently, the measured maximum temperatures at the center of the test masks from Table 4.2 and Table 4.4 are plotted as a function of the incident beam powers. Figure 4.5 and Figure 4.6 show a proportional relationship for both of the complete coverage and the center block mask. The validation of the relationship between mask temperature and incident beam power strongly depends on the distance of the proximity gap. As the distance becomes smaller, the better heat transfer through the proximity gap will further reduce the temperature in the masks during exposure.

The linear fit shows that thermal conduction, which linearly relate heat transfer and temperature, dominates the heat transfer mechanism. The functions obtained from the curve fitting suggest that the center block mask has a higher temperature compared to the complete coverage mask at the same incident beam power. The slope ratio of the fitted functions for the two cases is 9:8. This finding is consitent with simulated results: The energy deposited in the complete coverage mask is triple of it is in the center block mask, since the area of its nickel layer is two times larger. However, the lower thermal conductivity of polyimide compared to nickel results in a less efficient dissipation of heat in the center block mask, such that despite of the reduced beam power absoprtion, almost identical temperatures are observed.

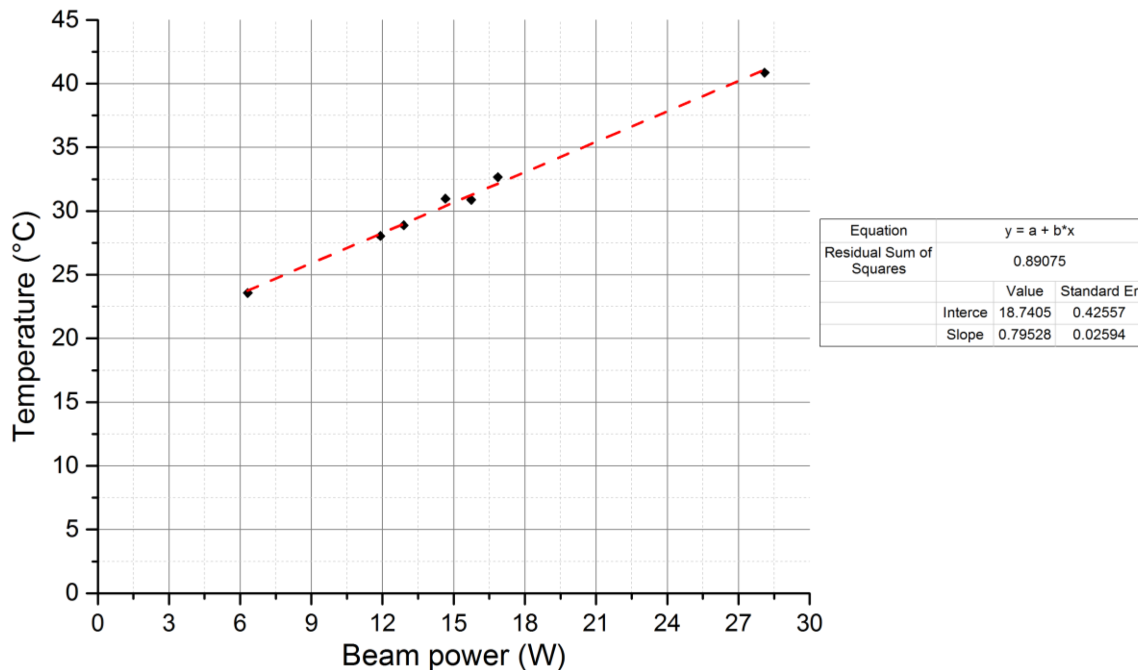

Figure 4.5: Maximum temperature at the center thermocouple (#5) measured for various computed incident beam powers with the complete coverage mask: curve fitting shows a linear relationship with a slope of 0.80°C /W for the complete coverage mask.

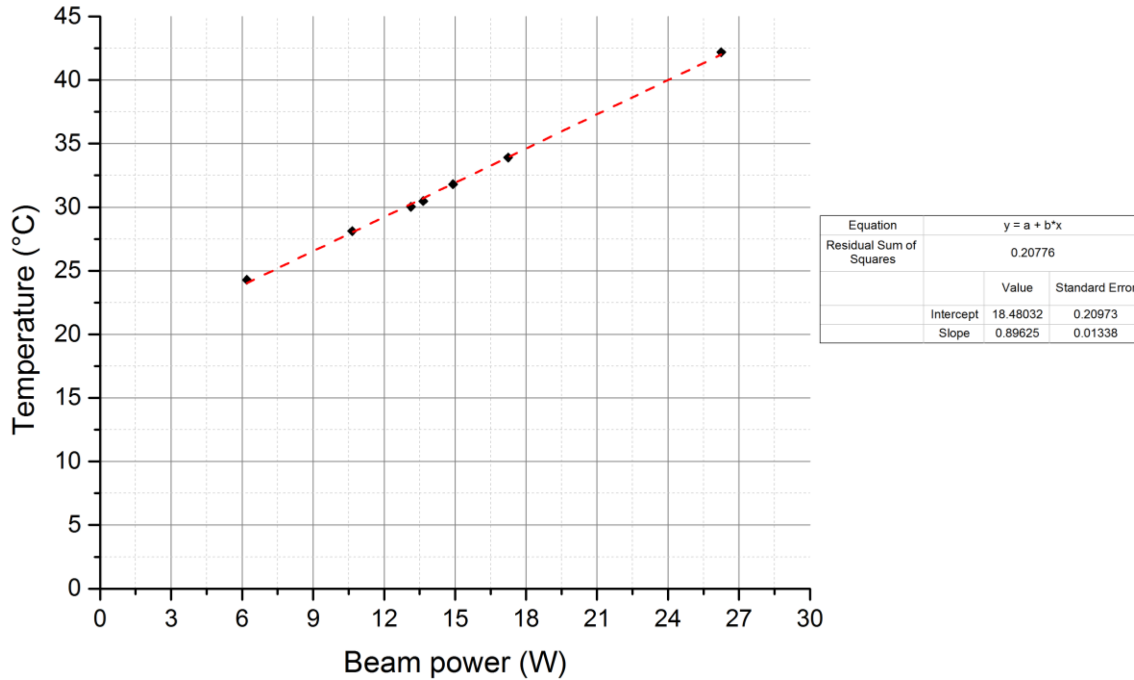

Figure 4.6: Maximum temperature at the center thermocouple (#5) measured for various computed incident beam powers with the center block mask: curve fitting shows a linear relationship with a slope of 0.90°C /W for the center block mask.

4.4 Discussion

The temperature measurements generally align well with the simulated temperature distribution. The qualitative behaviour is in good agreement. Quantitatively, the number of scans needed to reach thermal equilibrium also aligns well. As far as specific temperature values are concenrned, the complete coverage mask, for instance, delivers a simulated maximum temperature of 39°C to 40°C, depending on the exact location in the model. The corresponding experiment is Test #6 which delivers, according to Table 4.2, up to 36°C. At the loaction of the center thermocouples, the difference is about 6°C. The errors between the simulated and measured temperatures are compared in more detail in Figure 4.7 and Figure 4.8. The simulated thermal distribution consistently overestimates the experimental values by approximately 6°C for the complete coverage mask, and by about 4°C for the center block mask. Many aspects could lead to question the exactness of the simulations, including the necessary compromises made in modeling the exposure process, the simplifications made to decrease the computational power needed, or the exactness of the simulated input power values. As importantly, though, can issues in the experiment lead to underestimating the actual temperatures in the polyimide X-ray masks. A less than optimum thermal contact between the thermocouples and the nickel absorber, for instance, could lead to too low a measured temperature. Since the thermocouples were attached to the mask using self-adhesive Kapton® tape rather

than permanent, but thermally better conducting thermal glue, incomplete thermal contact might be a key contributor to the slight offset in temperatures.

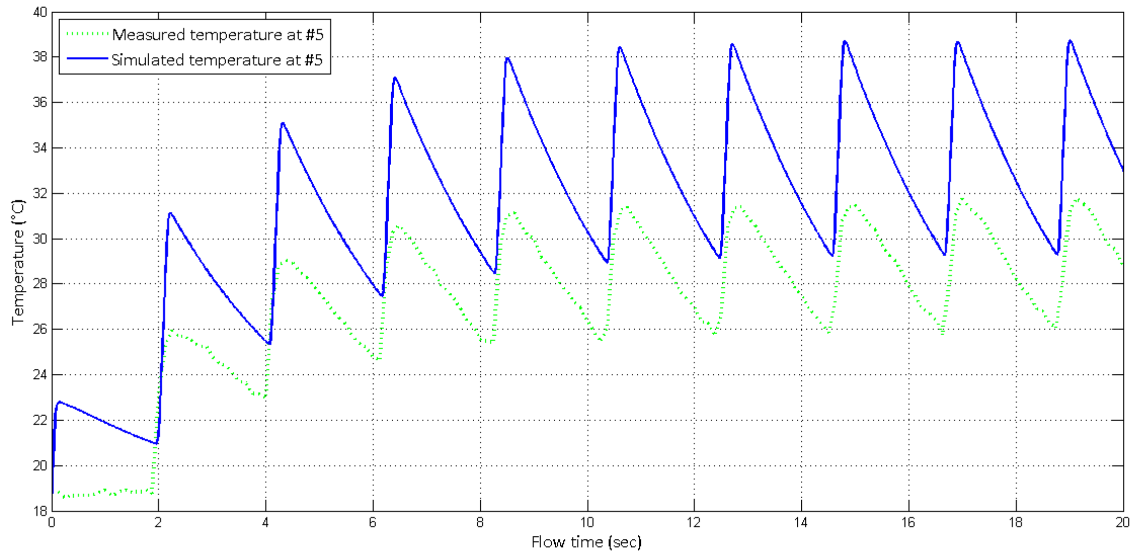

Figure 4.7: Simulated (solid line) and measured (dotted line) temperature with respect to time at the location of the center thermocouple (#5) for the complete coverage mask.

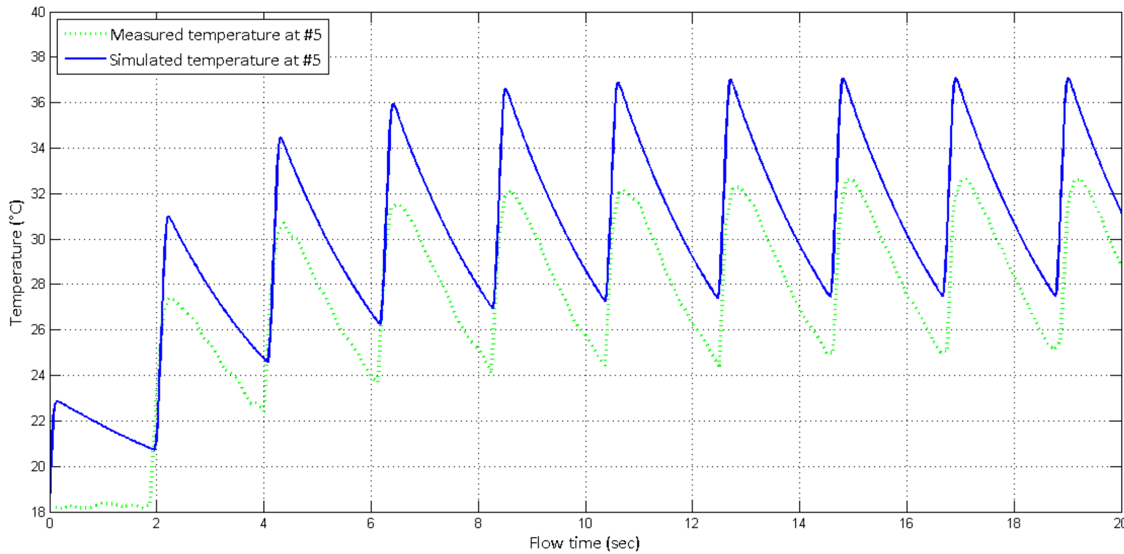

Figure 4.8: Simulated (solid line) and measured (dotted line) temperature with respect to time at the location of the center thermocouple (#5) for the center block mask.

A closer look at the temperatures measured at the top (#2) and bottom (#4) thermocouples reveals unexpected results: in the simulations discussed in Chapter 3, both temperatures were identical, when comparing the same case and at the time when the location is hit by the beam. This is a physically reasonable

result since the locations are thermally equivalent. The measured temperatures are different, though the measured temperature at the bottom of the mask (#4) has the highest temperature rise and the top (#2) has the lowest, rather than a symetrical temperature distribution in the vertical axis. The difference is about 6°C in the case of complete coverage mask, and 4°C in the case of center block mask. The disparity between the simulated and measured temperatures is attributed to an experimental artefact rather than a systematic error in the simulations: during the experiments, the substrate holder was not maintained parallel to the mask plane. The substrate holder is, under normal exposure conditions, pressed against the mask, using proximity shims and maintaining parallel orientation. During the thermal tests, though, a much larger than usual proximity gap was needed to accommodate the thermocouples, and proximity gap spacers could not be used to protect the thermocouple wires. Under the given conditions, the substrate holder can slightly swivel. Gravity leads to a slight tilting of the substrate holder, such that the proximity gap at the top is smaller than at the bottom (see Figure 4.9). This leads to more efficient cooling across the smaller proximity gap at the top, and hence lower temperatures: the proximity gap has an non-uniform distance so that the thermal conductance of the helium gas is not homogenous at different heights.

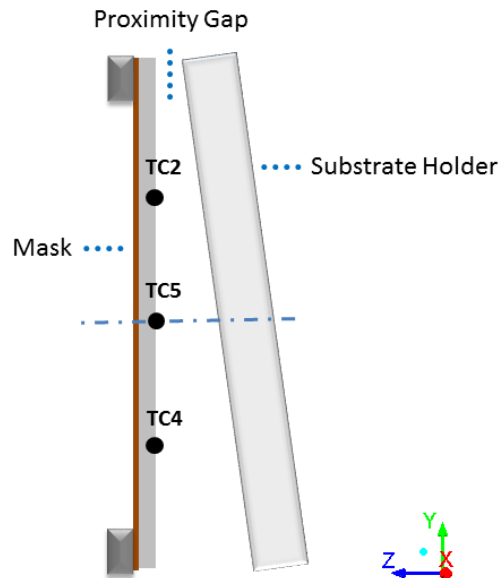

Figure 4.9: Schematic of the tilted substrate holder during the measurements.

Apart from the mentioned minor discrepancies, the experiments basically validated the simulated model. It can therefore be applied to simulate expected thermal distributions during the exposure process. In Chapter 5, two typical DXRL exposure scenarios will be simulated.

4.5 Chapter Summary

In this chapter, the temperature distributions in the test masks during X-ray exposures were measured with five thermocouples bonded to the absorber. For either of the two masks, seven different beam powers were analyzed. Beam power adjusted by using different pre-absorbers and intensity chopper duty cycle settings and were quantified by using the software LEX-D. For the complete coverage mask, maximum temperatures of 24.5°C were measured for an incident beam power of 6.32 W, while a maximum temperature of 46.6°C was recorded for an incident beam power of 28.1 W. For the center block mask, maximum temperatures of 24.5°C were measured for an incident beam power of 6.20 W, while a maximum temperature of 42.9°C was recorded for an incident beam power of 26.3 W. While the experimental results generally validate the numerical results in the preceding chapter, some discrepancies were found, which were associated with an unexpected inconsistency in the experimental setup. Under the conditions required for the experiments, the separation between mask and the substrate holder in the scanner during exposure is not constant across the mask area, but varies locally and is therefore different from the constant value assumed in the simulations. Fundamentally, however, the measured temperatures not only validated the numerical cases considered before, but also proved that the temperature rise was proportional to the incident beam power, which substantiated the target of becoming able to predict the temperature rise in the X-ray mask for a wide range of potential load cases.

CHAPTER 5

SIMULATION OF DXRL EXPOSURES

In the previous two chapters, a thermal and thermoelastic simulation tool was developed to study thermal deformations in DXRL masks, and it was experimentally verified. The geometric space available for the verification was limited, and photoresist and wafer could not be implemented in the analysis. With a reliable simulation tool at hand, the model can now get extended to include photoresist and wafer layers and apply the complete model to predict thermal deformations under realistic DXRL exposure conditions.

The extended model now includes PMMA as the most typically applied photoresist in DXRL. Studied thicknesses vary bewteen 100 µm to 500 µm. The model also includes a 500 µm-thick standard silicon wafer. Figure 5.1 illustrates this extendeed model (compare with Figure 3.5 for the original basic model). Also, the proximity gap is reduced to 100 µm, according to the standard setting of the X-ray scanner at SyLMAND. This extended simulation for the DXRL exposures requires further development of User Defined Functions (UDFs) in ANSYS FLUENT®, as the other layers in the model can be heated by absorption of the synchrotron beam, while in the previous model only the nickel absorber absorbed power. Beside the UDF for heat generation in the nickel absorber, additional UDFs are now implemented for the polyimide membrane, the PMMA resist, and the silicon wafer. The thermal properties of PMMA and silicon are presented in Table 5.1.

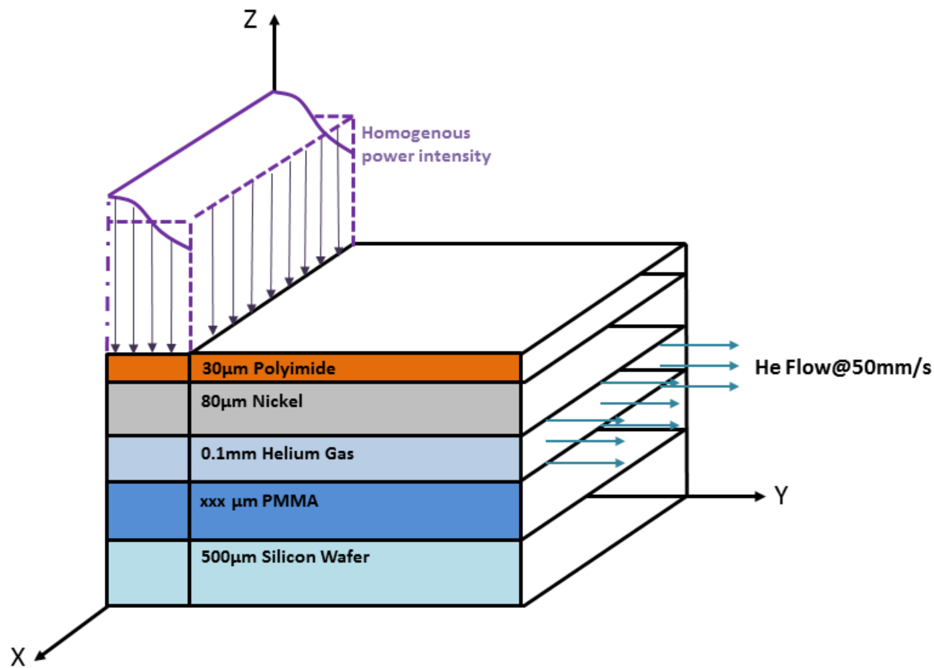

Figure 5.1: Extended DXRL exposure simulation model with PMMA-wafer assembly: Cross-sectional view of the synchrotron beam impinging onto the modeled layers.

Table 5.1: Thermal properties of PMMA X-ray resist and silicon wafer [10]

Material	Density (kg/m^3)	Specific Heat (J/kg)	Thermal Conductivity (W/m/K)
PMMA	1170	1466	0.2
Silicon	2329	700	148

5.1 Simulation for the Complete Coverage Test Mask under DXRL Exposure

This first simulation is to identify the impact of the changed conditions when compared with the previous original model. The PMMA resist will, due to its low thermal conductivity, tend to decrease the heat transfer, while the significantly reduced proximity will increase it. For direct comparability, all other parameters have been kept constant: the beam power, including the pre-absorbers (30 µm Al, 150 µm Kapton), and the intensity chopper setting at 25% open duty cycle previously used for the simulation (and represented by experimental test #6) for the complete coverage mask in Chapter 3 will be reused here. A layer of 100 µm PMMA resist, together with a 500 µm silicon wafer, are added into the simulation model. The extended mesh consists of $1.586 \cdot 10^5$ nodes. All temperatures given are for the top surface of the respective layer (i.e. the side closest to the mask).

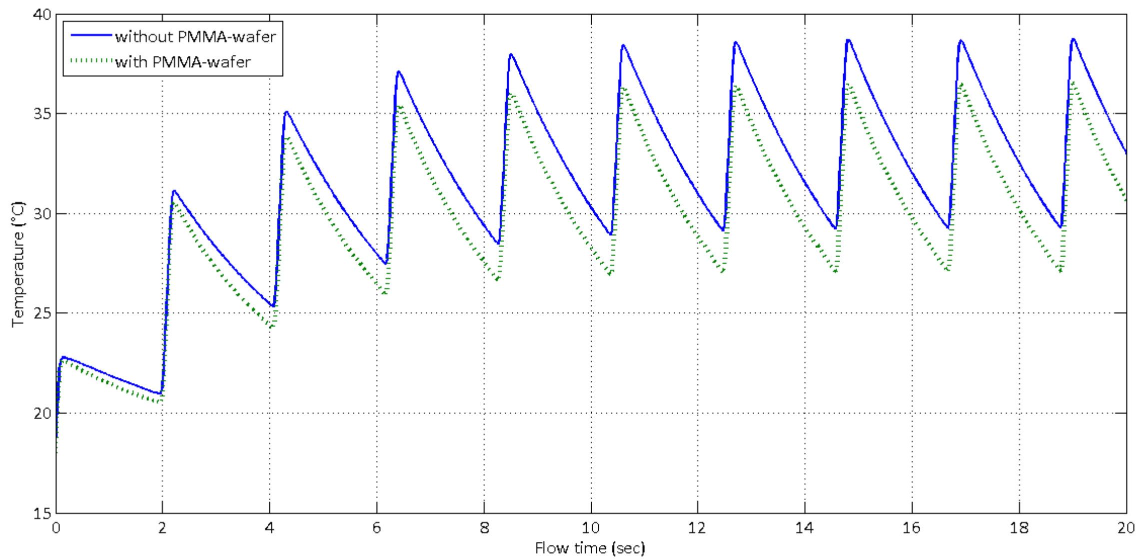

Figure 5.2: Simulated temperatures with respect to flow time at the location of the center thermocouple (#5) for the complete coverage mask using the intensity chopper with 25% open duty cycle. Top curve (solid blue): original model without resist and wafer, 1.4 mm proximity gap (compare Figure 3.8). Bottom curve (dotted green): extended model with PMMA resist and silicon wafer, 0.1 mm proximity gap.

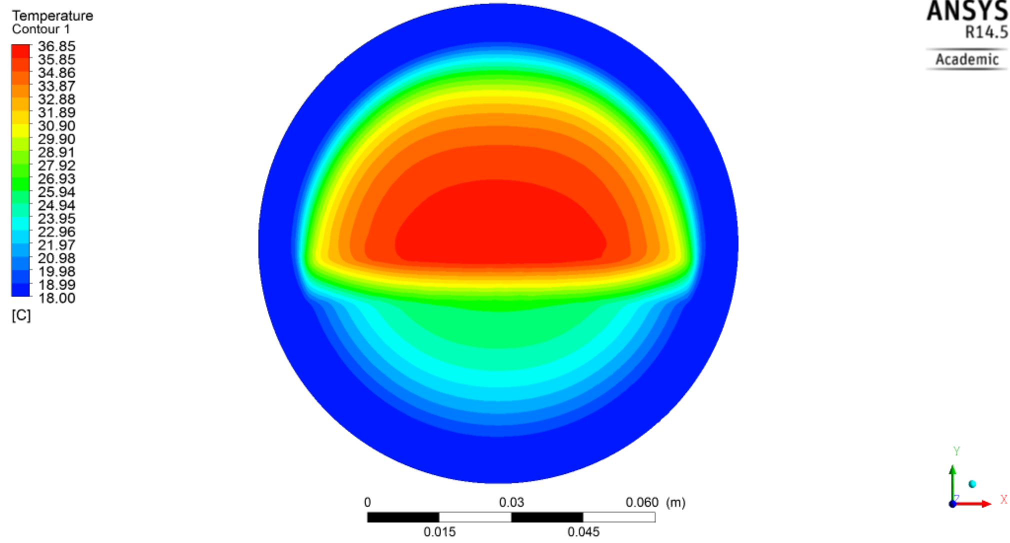

Figure 5.3: Simulated mask temperature distribution when the beam is at the location of the center thermocouple (#5) and the temperature reaches its highest values in that location. Simulation for the nickel absorber in the complete coverage mask.

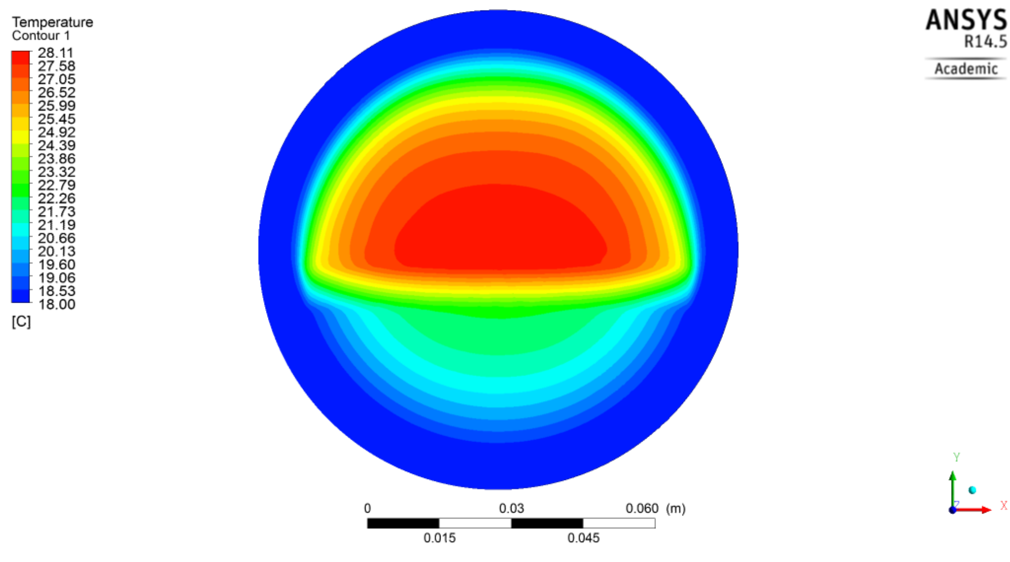

Figure 5.4: Simulated resist temperature distribution when the beam is at the location of the center thermocouple (#5) and the temperature reaches its highest values in that location. Simulation for the PMMA resist on the silicon wafer behind the complete coverage mask.

5.2 Simulation for the Center Block Test Mask under DXRL Exposure

The center block mask represents the typical case of a mask that is not entirely covered by absorbers. Consequently, the uncovered PMMA resist areas now get directly exposed to, and absorb, synchrotron

radiation. Two different standard resist thicknesses at SyLMAND are considered in this study: 250 μm and 500 μm. As explained in Chapter 1, different resist thicknesses require adjusted radiation spectra. To meet the requirement of a specific top-to-bottom dose ratio, the double mirror system and pre-absorbers are applied to change the spectrum of the synchrotron beam (see Table 5.2).

The beam powers absorbed in each layer, at 200 mA ring current, were recalculated with LEX-D to serve as input data for the numerical simulation and is compiled in Figure 5.5. (see Appendix D) The 80 μm nickel absorber effectively absorbs almost the entire beam power, with infinitesimal energy transmitted through it. In areas not covered by nickel absorbers, portions of the beam powers are deposited in the 30 μm polyimide membrane, in the 250 and 500 μm PMMA resist, and in the 500 μm silicon wafer (see Appendix E). Absorption in the helium gas layer is negligible and was therefore not modeled, as well as the infinitesimal energy deposited in unexposed PMMA and silicon wafer.

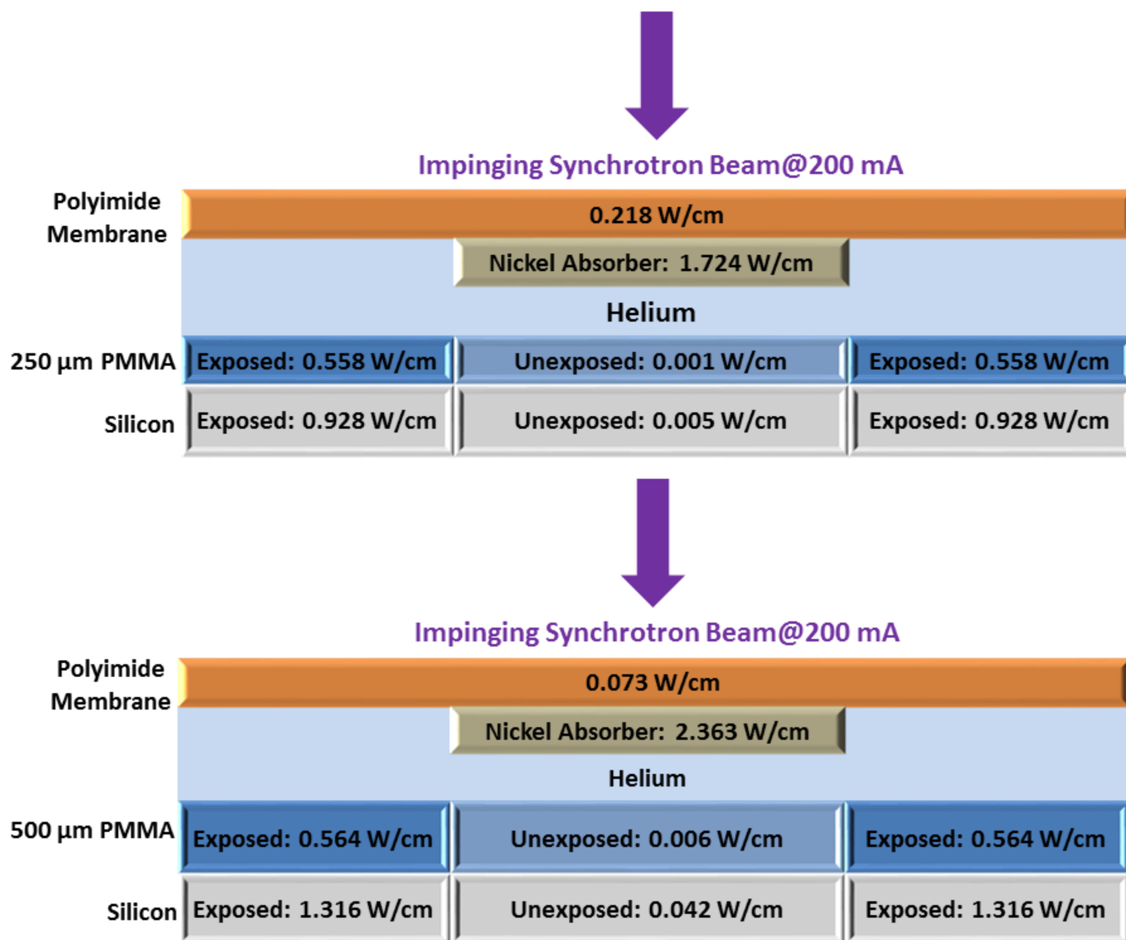

Figure 5.5: Beam power density distribution in the various layers of the extended DXRL exposure model (input data obtained from LEX-D calculations, considering the 25% intensity chopper) for the center block mask: Upper: 250 μm PMMA; Lower: 500 μm PMMA.

Table 5.2: Synchrotron beam parameters for DXRL exposures

PMMA Thickness (µm)	Mirror Angle (mrad)	Pre-absorber	Dose Expenditure (mA·min)	Intensity Chopper open Duty Cycle	Top-to-Bottom Dose Ratio	Incident Beam Power (W) at 200 mA calculated by LEX-D
250	4	N/A	252	25%	14.46 : 3.5	14.31
500	N/A	150 µm Kapton	424	25%	9.64 : 3.5	19.61

As the spectrum gets adjusted to be harder for the thicker PMMA layer, fewer hard spectral components are cut in the beamline, and the overall incident beam power in the simulation model is consequently higher than when exposing thinner PMMA layers (19.61 W as compared to 14.31 W). Mask absorbers are laid out to always absorb close to all radiation impinging at any spectrum to be expected. With higher incident beam power at thicker resist layers, more power will therefore get absorbed in the nickel absorbers (2.363 W/cm as compared to 1.724 W/cm). The polyimide membrane, however, only absorbs a small fraction of the incident beam power and gets even more transparent at higher photon energies. Due to a significantly lower fraction of the beam power absorbed in the polyimide at harder spectra, less absolute power will get absorbed in the polymer even at increased incident beam power (0.07 W/cm as compared to 0.218 W/cm).

The simulated temperature distributions in the center block mask and the 250 µm or 500 µm PMMA resist layers are presented in Figure 5.6 to Figure 5.9.

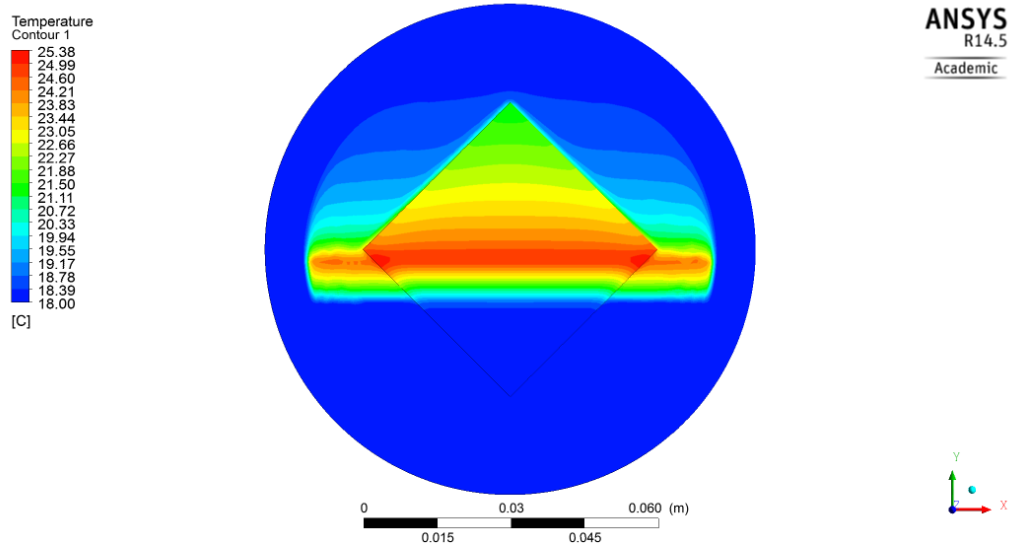

Figure 5.6: Simulated temperature distribution when the beam is at the location of the center thermocouple (#5) and the temperature reaches its highest value in that location. Simulation for the center block mask in front of 250 µm PMMA. (Beam moving downwards)

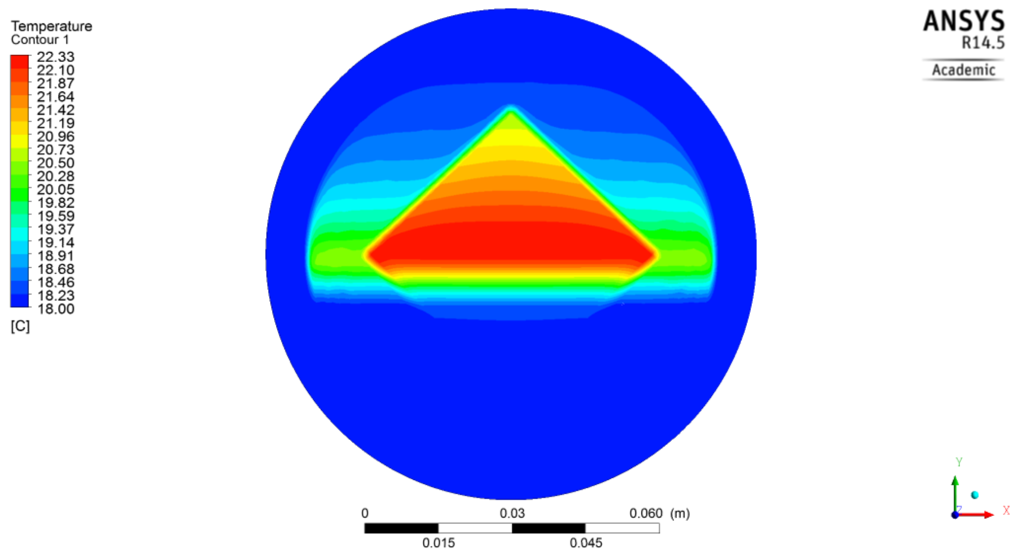

Figure 5.7: Simulated resist temperature distribution when the beam is at the location of the center thermocouple (#5) and the temperature reaches its highest value in that location. Simulation for 250 µm PMMA resist on the silicon wafer behind the center block mask. (Beam moving downwards)

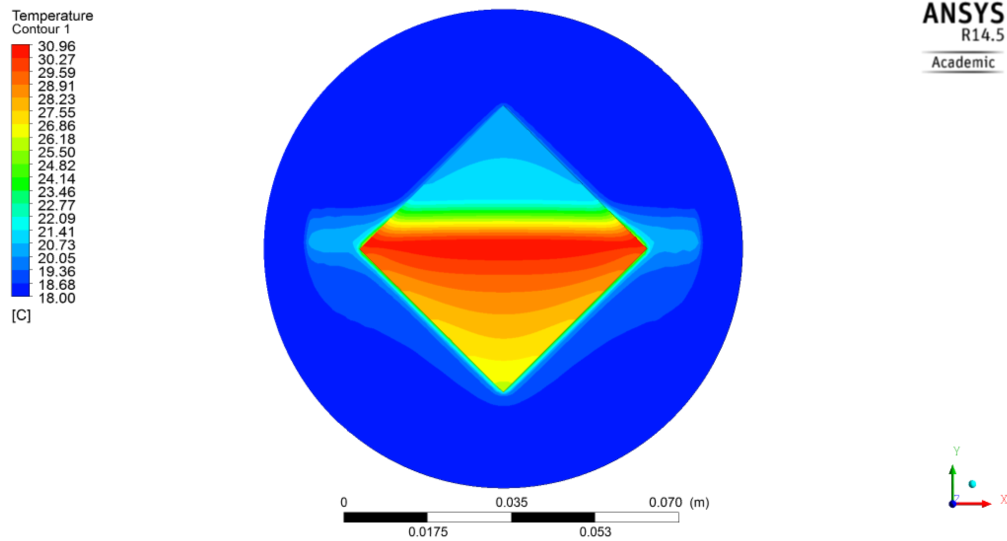

Figure 5.8: Simulated temperature distribution when the beam is at the location of the center thermocouple (#5) and the temperature reaches its highest value in that location. Simulation for the center block mask in front of 500 µm PMMA. (Beam moving upwards)

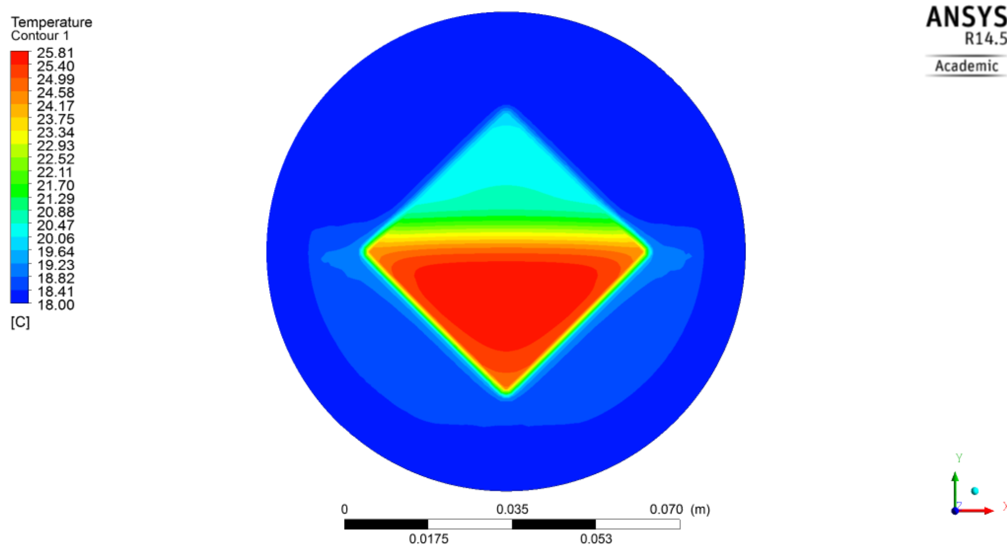

Figure 5.9: Simulated resist temperature distribution when the beam is at the location of the center thermocouple (#5) and the temperature reaches its highest value in that location. Simulation for 500 µm PMMA resist on the silicon wafer behind the center block mask. (Beam moving upwards)

5.3 Thermoelastic Simulation for the Center Block Mask and PMMA Resist

Temperature distributions obtained from thermal simulations described above are now used in thermoelastic simulations to quantify the thermal deformations occurring during DXRL exposures. The

center block mask and the PMMA resist as well as the silicon wafer are considered. The simulation for the mask uses the same FEM model described in Chapter 3, as no changes occur to the mask deformation mechanism in this case. The input temperatures, of course, are different now in the extended model. The new aspect of the deformation model is that now the PMMA layer on the silicon wafer is modeled as well. ANSYS Mechanical® is used, with the assumption of no slip or twist on the interface of the two components. The silicon wafer is considered to be bonded solidly to the substrate holder without any relative movement (see Figure 5.10). The mesh consists of $3.54 \cdot 10^4$ nodes and $6.37 \cdot 10^3$ elements. The mechanical properties of PMMA and silicon are presented in Table 5.3.

Table 5.3: Mechanical properties of PMMA and silicon [10][78]

Material	Thickness (µm)	Coefficient of Thermal Expansion (K^{-1})	Young's Modulus (GPa)	Poisson's Ratio
PMMA	250; 500	$68 \cdot 10^{-6}$	3.24	0.37
Silicon	500	$2.6 \cdot 10^{-6}$	169	0.28

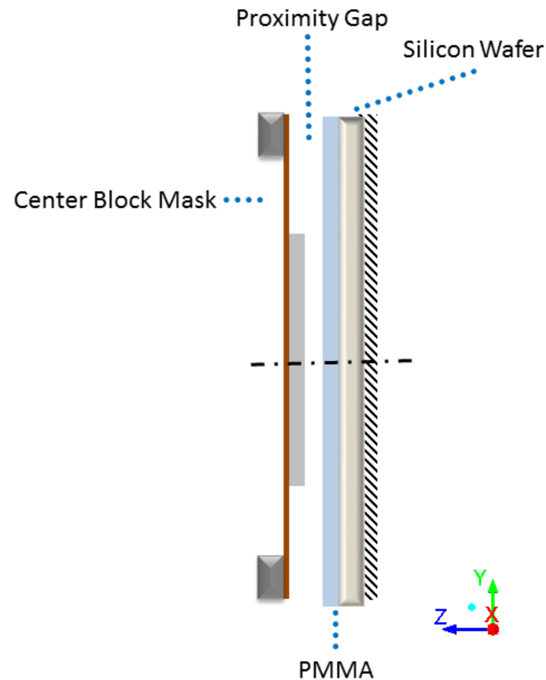

Figure 5.10: Schematic of the PMMA-wafer assembly model

5.3.1 Exposure of 250 µm PMMA

The simulated deformations for the center block mask and 250 µm PMMA are presented in Figure 5.11 and Figure 5.12.

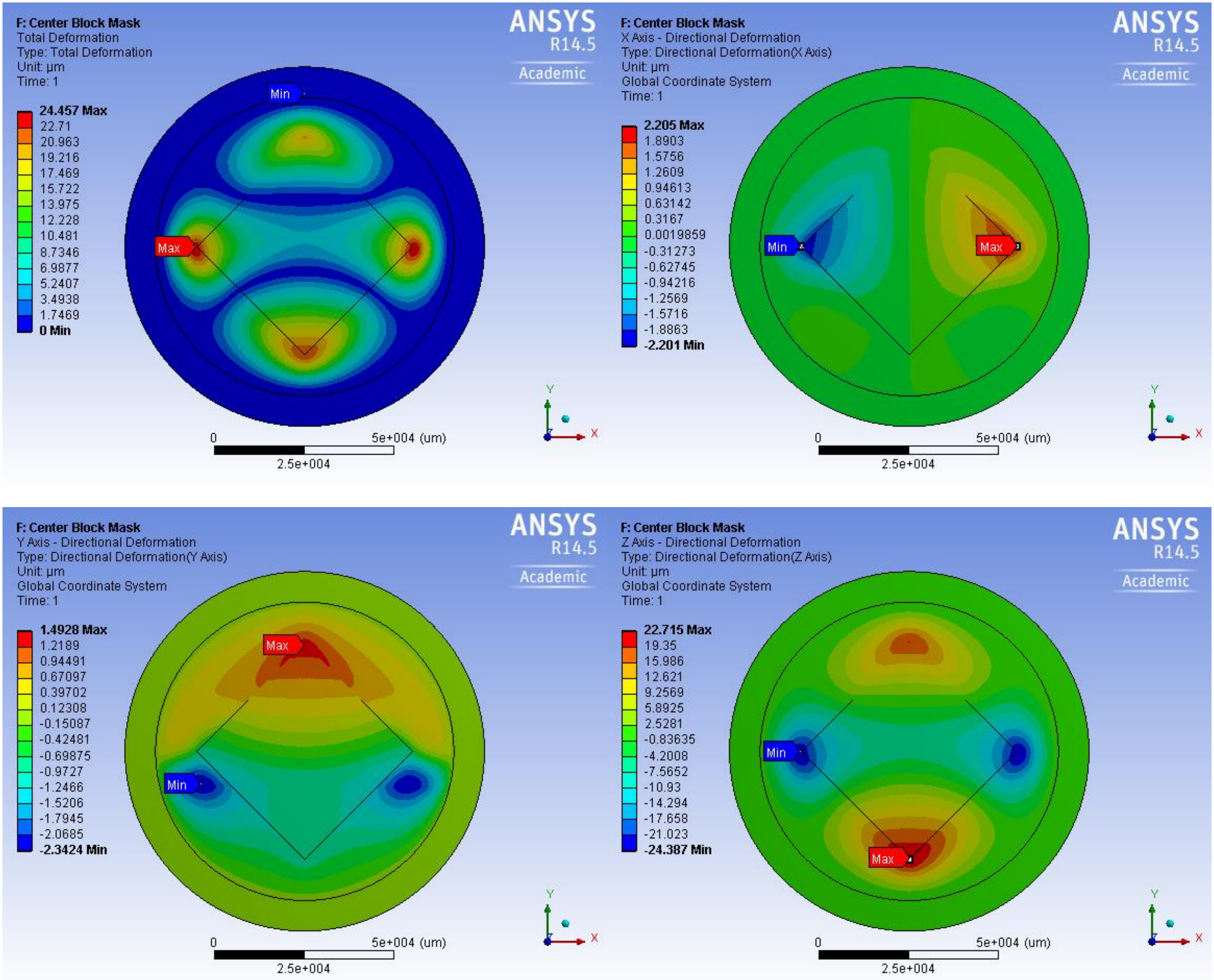

Figure 5.11: Simulated deformations (in micrometers) for the center block mask in front of 250 µm PMMA: Upper Left: Total deformation; Upper Right: Deformation along the *x*-axis in the mask plane; Lower Left: Deformation along the *y*-axis in the mask plane; Lower Right: Deformation along the *z*-axis opposing the beam direction.

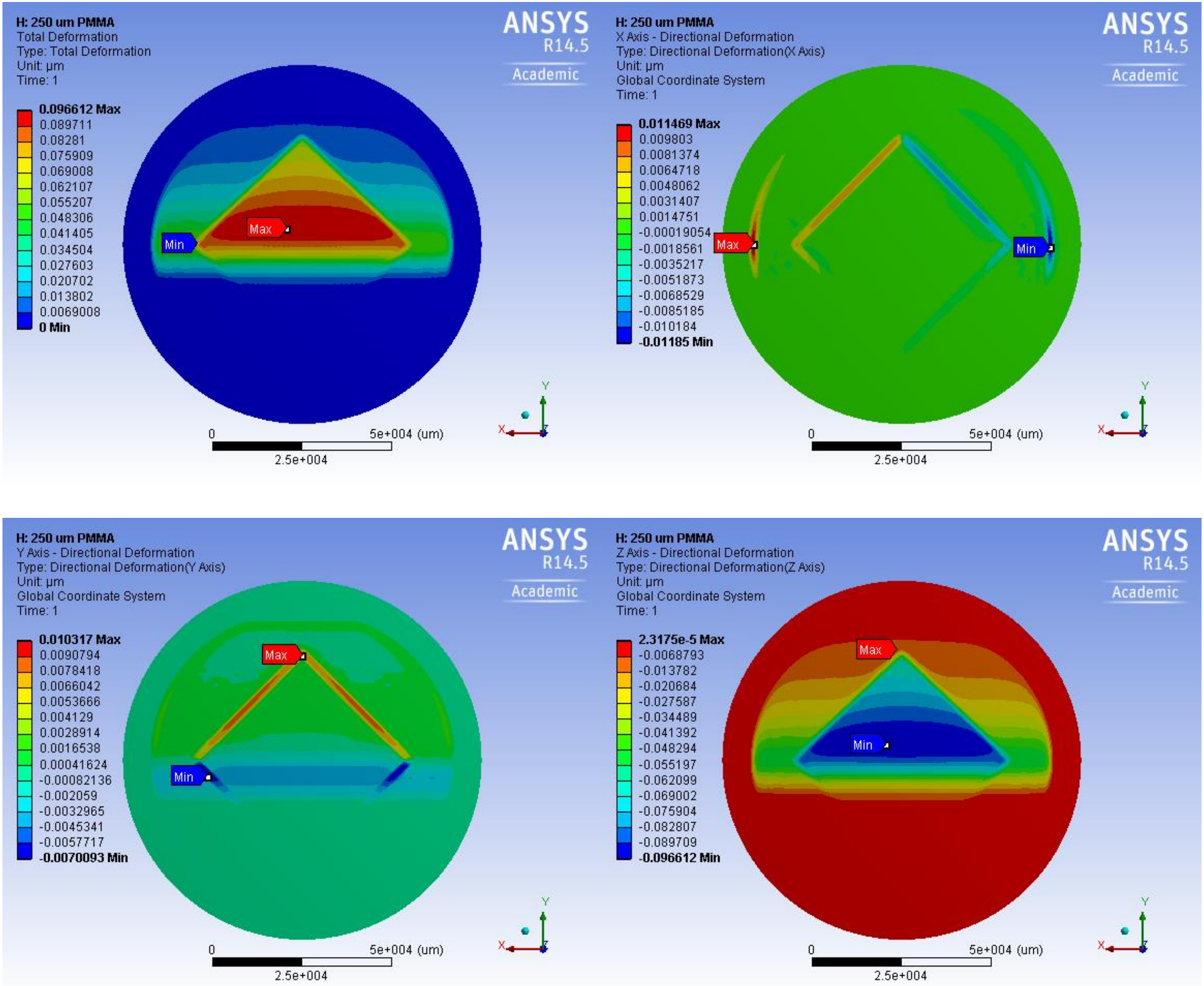

Figure 5.12: Simulated deformations (in micrometers) for the 250 µm thick PMMA layer behind the center block mask: Upper Left: Total deformation; Upper Right: Deformation along the x-axis in the mask plane; Lower Left: Deformation along the y-axis in the mask plane; Lower Right: Deformation along the z-axis opposing the beam direction.

5.3.2 Exposure of 500 µm PMMA

The simulated deformations for the center block mask and 500 µm PMMA are presented in Figure 5.13 and Figure 5.14.

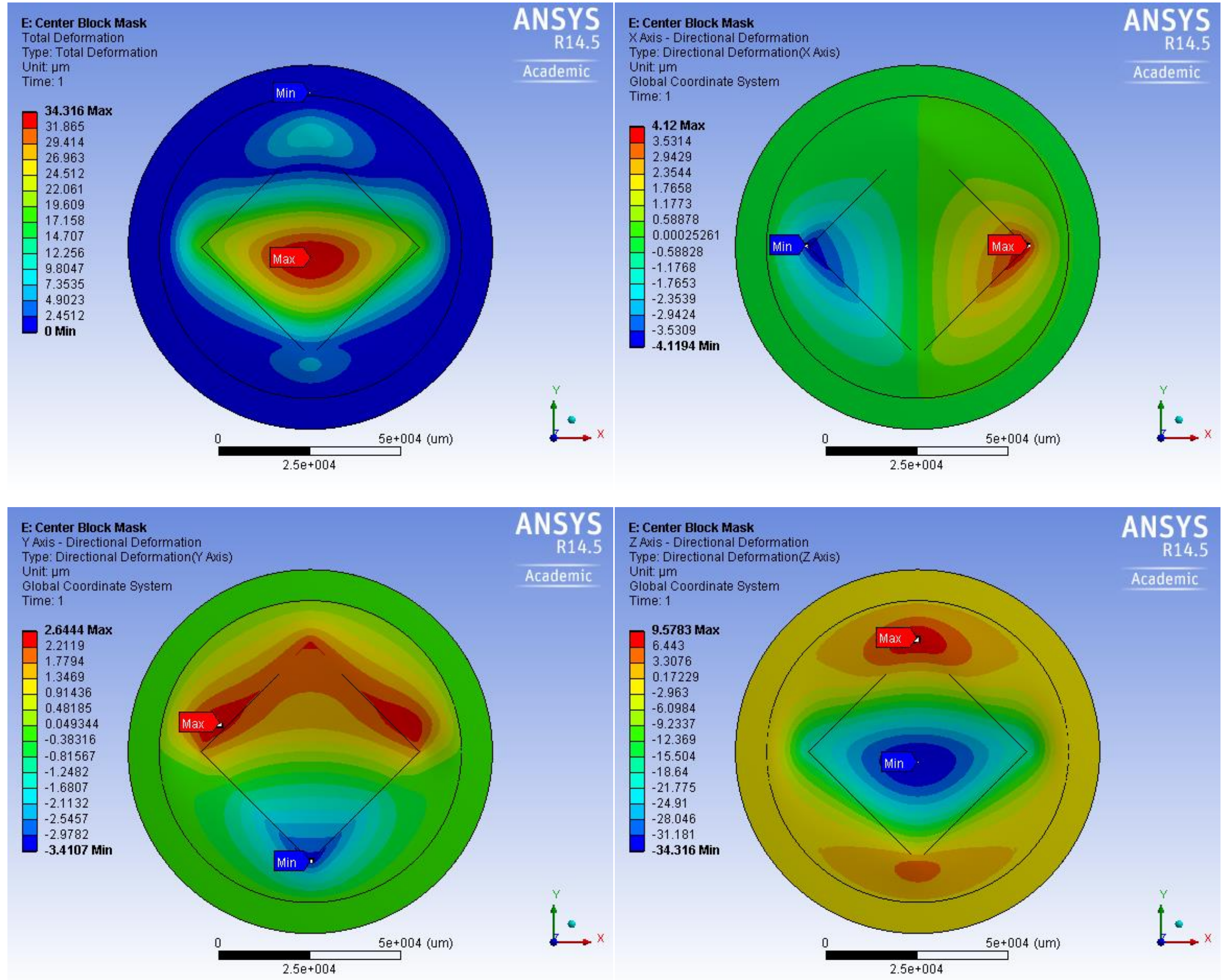

Figure 5.13: Simulated deformations (in micrometers) for the center block mask in front of 500 µm PMMA: Upper Left: Total deformation; Upper Right: Deformation along the x-axis in the mask plane; Lower Left: Deformation along the y-axis in the mask plane; Lower Right: Deformation along the z-axis opposing the beam direction.

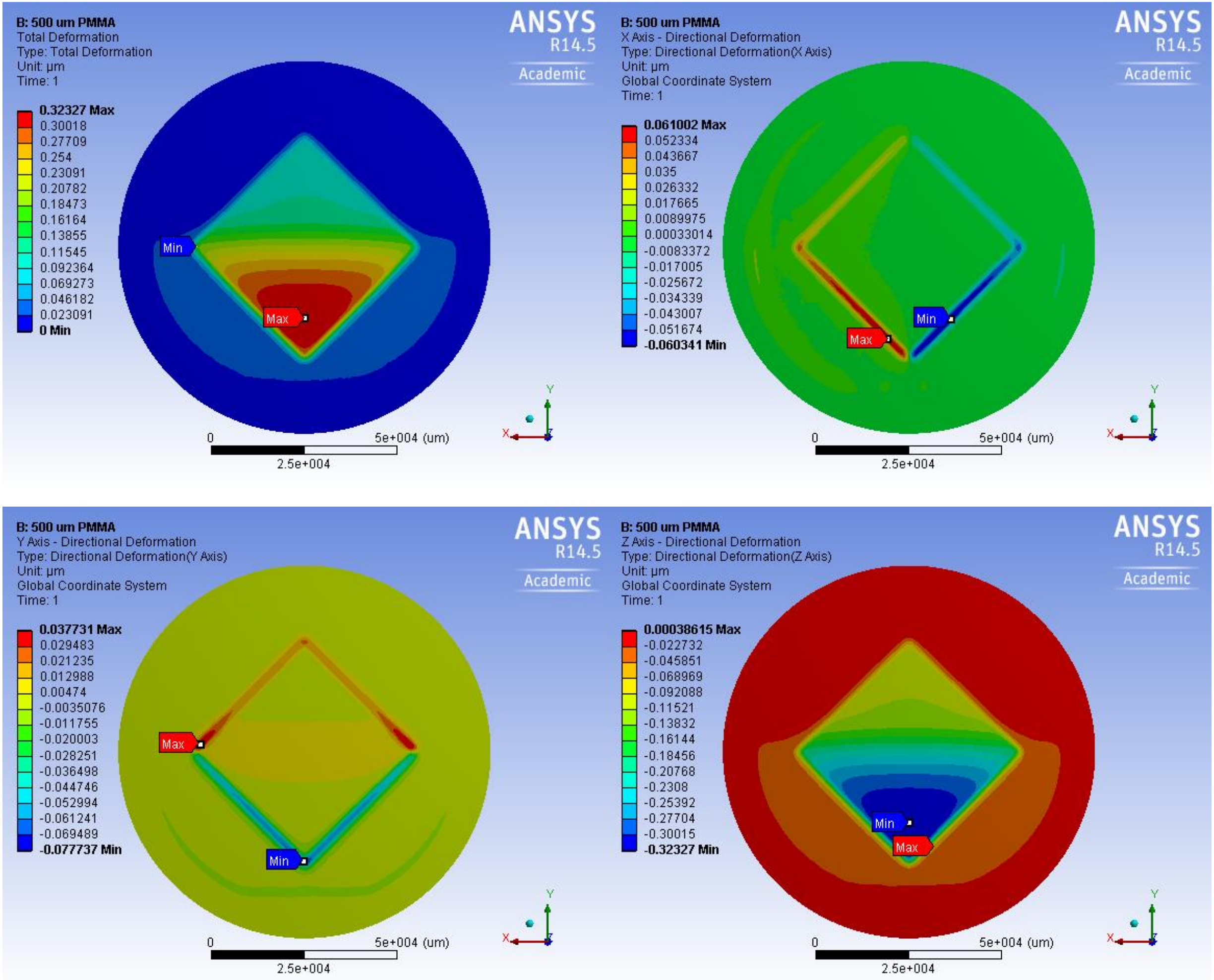

Figure 5.14: Simulated deformations (in micrometers) for the 500 µm thick PMMA layer behind the center block mask: Upper Left: Total deformation; Upper Right: Deformation along the *x*-axis in the mask plane; Lower Left: Deformation along the *y*-axis in the mask plane; Lower Right: Deformation along the *z*-axis opposing the beam direction.

5.3.3 Summary of Simulation Results

The results of the thermoelastic simulations for DXRL exposures are presented in Table 5.4.

Table 5.4: Results of the thermoelastic simulations for DXRL exposures

Cases		Max Temperature (°C)	Max Total Deformation (μm)	Max X-axis Deformation (μm)	Max Y-axis Deformation (μm)	Max Z-axis Deformation (μm)
250 μm PMMA	Mask	25.38	24.5	2.2	2.3	24.4
	Resist	22.33	0.10	0.01	0.01	0.10
500 μm PMMA	Mask	30.96	34.3	4.1	3.4	34.3
	Resist	25.81	0.32	0.06	0.08	0.32

5.4 Discussion

The thermal simulations show that the reduced proximity gap leads to a net increase of the cooling effectiveness despite the added PMMA-wafer assembly. The temperature rise in the complete coverage mask is slightly reduced, by approximately 2°C, when compared to the previous thermal simulation from Chapter 3 (compare Figure 3.10 and Figure 5.3). The mask now is heated up to 37°C. As before in Chapter 3, the heat gets dissipated along the mask absorbers to the mask frame, and across the proximity gap. This latter contribution is more efficient now as the gap is much reduced. From the PMMA resist surface, the heat is conducted, with limited efficiency compared to other solids, but better efficiency than across the helium gas gap, to the cooled wafer (see Figure 5.3). The heat transfer through the PMMA resist heats it up by 10°C even though the PMMA absorbed infinitesimal radiation behind the complete absorbers (see Figure 5.4).

For the center block mask, more UDFs were implemented in the model to obtain a better prediction of the effects during DXRL exposure. Lower layers in the areas unprotected by absorbers get exposed: parts of the polyimide membrane, of the PMMA, and of the silicon wafer also absorb beam power. Furthermore, the entire model, whether behind absorbers or not, gets heated and cooled by conduction. The highest temperatures occur in the center block mask. The resist underneath shows a similar lateral pattern of temperature distribution as the mask, but at an infinitesimal level. It is therefore apparent that the dominant heating mechanism of the resist is not direct absorption of radiation in PMMA behind transparent mask areas, but conduction of heat absorbed in the mask absorbers just above the non-exposed PMMA areas. A sharp temperature gradient in the PMMA layer is observed at the projected lateral layout boundaries of the absorber (see Figure 5.7 and Figure 5.9). This is because PMMA has a low thermal conductivity (similar

to polyimide), and the lateral heat dissipation within the wide resist layer is much slower than it is in the short axial direction towards the cooled silicon wafer. On the other hand, the exposed resist absorbs only relatively small fractions of the locally beam power, leading to very limited radiation-induced energy deposition in the resist layer. The observed, relatively low temperature rises in PMMA are critical to avoid foaming and cracking [14]. The two incident beam powers of the realistic scenarios discussed in this chapter (approximately 14-20W) exceed most of those values of the beam power studied by temperature measurements in Chapter 4 (approximately 6-30 W). Yet, the temperature rises in the mask remain well manageable.

The thermoelastic simulations show that during the DXRL exposure, the deformation in the PMMA resist is at a much smaller scale (up to about 1%) compared to deformations in the center block mask (see Table 5.4). Thus, the accuracy of pattern transfer is dominated by thermal deformations of the mask rather than the resist. The deformations in the lateral plane (*x-y* plane), as integrated distortions across the entire center block mask, amount to about 2 μm in each direction for 250 μm thick resist and about 4 μm in each direction for 500 μm thick resist. This increase in the thicker resist reflects the increased temperatures due to higher incident beam powers and reduced conduction through the thicker, poorly conducting PMMA.

As the local structure inaccuracy, deformations of several micrometers would be detrimental for most MEMS applications. As an effect integrated over almost the entire wafer (few MEMS components are 6 cm large and almost none have as large feature size as the center block mask), however, such results would still be acceptable for most cases, and mostly translate into position inaccuracies. Yet, the results show the outstanding importance of controlling the incident beam power to achieve a sufficient accuracy of pattern transfer. The deformation of the absorber must always be kept at the lowest level possible. Thus, the intensity chopper is a critical SyLMAND beamline component when implementing polyimide membrane masks. When changing from 25% open duty cycle used in these simulations to 10%, temperature rises and deformations would get reduced by a factor of 2.5, resulting in micron- or submicron deformations for the most part. Further reductions could be achieved when the intensity chopper gets upgraded for continuous duty cycle adjustability, and beam powers less than 10% can be selected. For complex patterns in a real X-ray mask, the small feature size will also decrease the local temperature rise and deformation, which thermal deformations might no longer be a dominant source of inaccuracy.

5.5 Chapter Summary

In this chapter, the simulation model from previous study was extended to study the thermal and thermoelastic situation for DXRL exposures under realistic conditions: The extended model included 100 to 500 μm thick PMMA resist on a 500 μm thick silicon wafer, as well as reduced proximity gap of 100 μm. This reduced proximity gap leads to a net increase of the cooling effectiveness despite the added PMMA-

wafer assembly. The temperature rise in the complete coverage mask is slightly reduced to only 37°C, when compared to the previous thermal simulation from Chapter 3. The heat transfer through the mask-covered PMMA resist heats it up by 10°C even though the PMMA does not itself absorb any radiation. For the center block mask, resist underneath absorbers shows a similar lateral pattern of temperature distribution as the mask, but at a lower level. Apparently, the dominant heating mechanism of the resist is conduction of heat absorbed in the mask absorbers just above the non-exposed PMMA areas. A sharp temperature gradient in the PMMA layer is observed at the projected lateral layout boundaries of the absorber. This is because PMMA has a low thermal conductivity, and the lateral heat dissipation within the wide resist layer is much slower than it is in the short axial direction towards the cooled silicon wafer. On the other hand, the exposed resist absorbs only relatively small fractions of the local beam power, leading to very limited radiation-induced energy deposition in the resist layer. The deformation in the PMMA resist is about 1% of the deformations in the center block mask, and the accuracy of pattern transfer is dominated by thermal deformations of the mask rather than the resist. In the lateral plane, integrated distortions across the entire center block mask amount to about 2 μm in each direction for 250 μm thick resist and about 4 μm in each direction for 500 μm thick resist. Local deformations are much smaller. The results still demonstrate the significant importance of controlling the incident beam power, e.g. by means of the intensity chopper, to achieve a sufficient accuracy of pattern transfer.

CHAPTER 6

SUMMARY AND CONCLUSION

6.1 Summary and Conclusion

This thesis aimed to identify and develop a viable fabrication approach for polyimide membrane X-ray masks to be used at SyLMAND. Special consideration was given to quantify the anticipated heat load and the resulting thermal deformations during exposure. The fabrication method for the polyimide membrane X-ray mask was developed within the restrictions of materials (e.g. mask absorber plating alternatives) and equipment (e.g. maximum achievable curing temperatures) available at SyLMAND. The heat load under different beam power scenarios was analyzed numerically and verified experimentally. Subsequently, a detailed study based on the simulated temperature distribution predicted the thermal deformations of test masks for realistic deep X-ray lithography (DXRL) exposure scenarios with PMMA resist layers of different thicknesses (250 µm; 500 µm) and silicon wafer substrates.

Two polyimide products, Evonik P84® and Durimide 7520® have been investigated as potential mask membrane materials. Spin-coating experiments proved Durimide 7520® to generate a more homogeneous membrane than P84® even after modifications for improved spin coating behaviour. A complete fabrication sequence was developed for Durimide 7520 membranes, including patterning of mask absorber templates in 100 µm thick negative tone UV resist NR26-25000P®, electroplating of the absorber structures in 80 µm thick nickel, and release of the polyimide membrane through etching of the exposure window into the stainless steel sacrificial substrate using $FeCl_3$. The final polyimide X-ray test masks have 30 µm thick polyimide membranes and 80 µm thick nickel absorbers, with an exposure window of 83-mm-diameter. Two test masks were prepared, one with complete coverage of absorber, the other with a square absorber layout at the center.

Thermal challenges often encountered when using polymer-based mask membranes can be controlled using some of the SyLMAND laboratory's design features: The intensity chopper at SyLMAND can significantly reduce the heat load by changing the duty cycle of the incident synchrotron beam from 100% to 10% or 25% of the full beam power. Also, the double mirror system and X-ray pre-absorbers can reduce the beam power by modifying the beam spectrum. These instruments at SyLMAND allow quasi-continuous beam power tuning, and therefore control of the heat load in the mask during exposure. Their impact on the lithographic results was further studied:

Numerical simulations were carried out to analyze the temperature rise and resulting thermal deformations: ANSYS FLUENT® was used for the thermal analysis by computational fluid dynamics, and ANSYS Mechanical® was applied for thermoelastic analysis with the finite element method. The numerical

model was experimentally verified, using five thermocouples attached to the surface of the mask absorbers. Temperature distributions in the test mask during exposure were obtained and verified the numerical model of thermal simulation. However, some discrepancies on the order of 5°C existed between simulated and measured temperatures. The error is caused by an unintentional tilt of the substrate holder during the experiments, which locally changed the distance of the proximity gap.

It could be shown that the mechanism of heat dissipation between the mask as the primary absorber of the incident beam power and the cooled surroundings of the mask is mainly through thermal conduction across the proximity gap. The temperature of the X-ray mask increases proportionally with the incident synchrotron beam power at otherwise constant conditions. Beam power tuning using the intensity chopper and other beamline and storage ring properties can therefore be applied to control the temperature rise in the polyimide X-ray mask. Temperatures obtained from numerical simulations and experimental results were related to specific incident beam power values obtained from analytical results of photon-solid matter interaction. Individual beam power – mask temperature values were finally interpolated to obtain a generalized prediction of anticipated mask temperatures for different exposure scenarios. Typical final temperatures amount to 30 to 40°C for incident beam power values around 10 W.

The polyimide membrane has a low thermal conductivity (0.12 W/m/K) and a high thermal expansion coefficient ($55 \cdot 10^{-6}$ K^{-1}), which can cause undesired thermal deformations of the locally exposed, and heated, absorber patterns. The thermoelastic simulation results of DXRL exposure show that the deformations in the lateral plane are only about 10% of the axial deformations. Only those lateral distortions have a direct impact on the final structure accuracy of the lithographic process. For the center block mask, the deformations in the lateral plane amount to approximately 2.3 μm for 250 μm thick PMMA, and to approximately 4 μm for 500 μm thick PMMA. These deformations, integrated across the entire layout area, are seen to not affect the accuracy of pattern transfer significantly, provided that the incident beam power is reduced by the intensity chopper as was done in the studied cases. While the mask absorbers deformed on the order of micrometers, the thermal deformations in the PMMA resist itself is limited to dozens of nanometers, which can be neglected when compared to other sources of inaccuracies.

The results of the fabrication process and the thermal analyses promise successful application of polyimide-based X-ray masks at SyLMAND. Thermal deformations of the absorber patterns can be controlled to an acceptable level, so that thermoelastic deformations of the mask will not significantly reduce the pattern transfer accuracy in the resist during exposure. The key component at SyLMAND to achieve this goal is the intensity chopper which can effectively reduce the heat load in the polyimide X-ray mask during exposure, at the cost of increased exposure times.

6.2 Future Work

The following items could be considered to expand the current research and to more thoroughly investigate the topic:

- As gold electroplating capabilities have now been developed at SyLMAND, future polyimide masks can use gold absorbers so that thinner (and more easily fabricated) absorbers can be applied.
- As a high resolution, direct-write UV laser lithography system is currently getting commissioned at SyLMAND, high resolution mask templates can be fabricated on future polyimide X-ray masks.

The two points above allow to complete the fabrication sequence developed in this research with improved absorber patterning techniques to fabricate XRL masks with complex MEMS layouts for further studies and applications.

- The experimental verification and analysis aspect could be further improved by replacing the sensing approach: the simple thermocouples used to measure the temperature distribution in the X-ray mask during exposure can be replaced by a costlier, but advanced infrared camera. The development of thermographic technology now provides high resolution in both image and temperature. For example, JENOPTIK produces an infrared camera with image resolution of 2014 × 1536 infrared pixels and thermal resolution of less than 0.05 Kelvin. The measurement with advanced infrared camera can meet the requirements of real-time and high resolution, which is much more detailed than using thermocouples. For this approach, however, such a camera would have to be purchased. Furthermore, the viewport glass in the X-ray scanner would have to be replaced with an infra-red-transparent alternative, or a vacuum feedthrough would have to be designed and implemented.
- The deformation of the mask layout incurred during the entire fabrication process needs to be studied as a further cause of overall lithographic inaccuracies, beyond thermal deformations during exposure. One such contribution to be studied would be the curvature of the mask under the impact of the various thin films deposited. Measurements require a surface profiler. However, the accessibility of a device that can measure the 4" substrate is limited at SyLMAND and the CLS. A new optical profiler is currently getting procured and will be available soon, which will allow the measurement of the mask curvature during the fabrication process.

APPENDIX A

TECHNICAL INFORMATION FOR POLYIMIDE MATERIALS

A.1 Polyimide Solution P84®

Table A.1: Mechanical properties of P84® compiled from vendor information (Evonik, Germany)

Tensile Strength (MPa)	140
Young's Modulus (GPa)	3.9
Glass Transition Temperature (°C)	315
Thermal Decomposition Temperature (°C)	550
Coefficient of Thermal Expansion (10^{-6}/°C)	50

Table A.2: Mixture of P84® and NEP

	Evonik P84® Solution	N-Ethyl-2-Pyrrolidone (NEP)
Density (g/cm^3)	1.125	0.99
Volumetric Percent	70.00%	30.00%
Mixture Density (g/cm^3)	1.129	
Weight Percent	17.06%	82.94%

A.2 Photoresist Durimide 7520®

All information is compiled from vendor information (Fujifilm Electronic Materials U.S.A., Inc.; North Kingstown, RI).[68]

Table A.3: Mechanical properties of Durimide 7520® [68]

Tensile Strength (MPa)	215
Young's Modulus (GPa)	2.5
Glass Transition Temperature (°C)	285
Thermal Decomposition Temperature (°C)	525
Coefficient of Thermal Expansion (10^{-6}/°C)	55

Table A.4: Processing parameters of Durimide 7520® [68]

Exposure Range	60-200 mJ/cm2
Soft Bake	100°C/3 min
Post Exposure Delay	20-22°C/30 min
Cure	350°C/60 min
Shrinkage from Soft Bake to Cure	45%

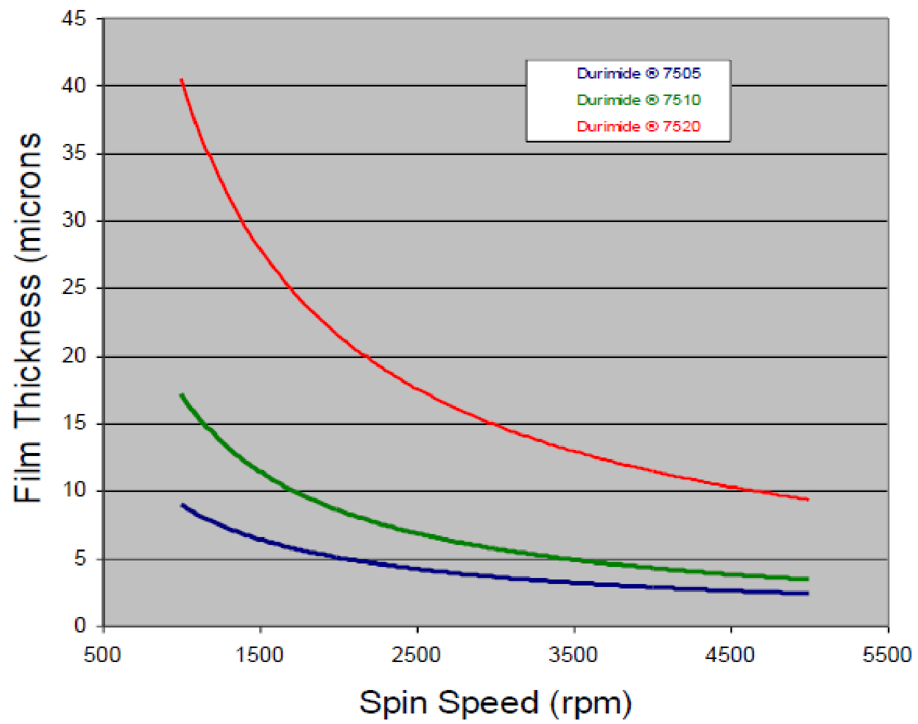

Figure A.1: Relationship between spin speed and cured film thickness for Durimide 7520®. [68]

APPENDIX B

SURFACE ROUGHNESS MEASUREMENTS FOR POLYIMIDE MASK FABRICATION

The surface roughness of the stainless steel substrate, of the polyimide membrane, and of the titanium layer was measured using a Micromap 570 3D optical surface profiler manufactured by Micromap Corporation (Tucson, AZ). The measuring window of the surface profiler is 1.254 mm × 0.934 mm. The measurement mode was 'wave mode', which utilizes white light interferometry phase scans. The surface roughness of the substrate and polyimide membrane was measured at the center of the sample. For the measurement of the titanium layer, the surface roughness was measured at the center and two radii, 25 mm and 45mm (see Figure B.1). For either radius, two different points were measured with the sample rotated by 90°. The results of the surface roughness measurement are presented in Table B.1. The roughness values are given based on two-dimensional area scans rather than conventional one-dimensional line scans. Associated roughness values, according to new standards, include the area-average roughness S_a, given in units of Ångström (10^{-10} m, or 10^{-4} μm).

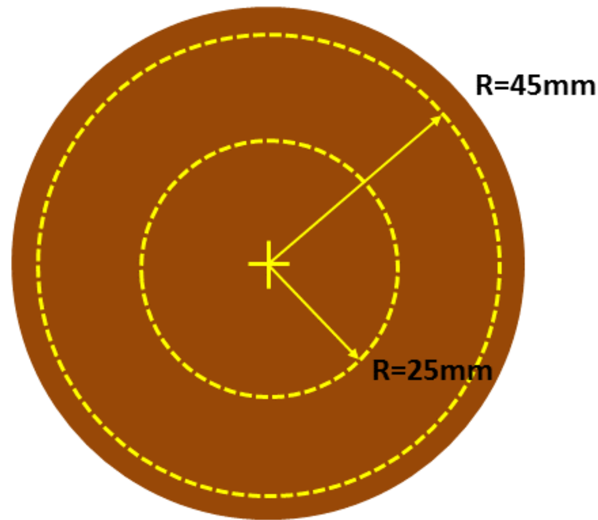

Figure B.1: Positions of surface roughness measurements for the titanium layer.

Table B.1: Measured surface roughness at selected mask fabrication steps

Surface	Average Roughness, S_a (Å)	Maximum Height Difference, S_t (Å)
Stainless Steel Substrate	1590	22960
Polyimide Membrane	596.9	15620
Titanium Layer @ Center	1693	22750
Titanium Layer @ R=25 mm	1346	18560
Titanium Layer @ R=25 mm - 90°	1598	23550
Titanium Layer @ R=45 mm	1622	25880
Titanium Layer @ R=45 mm - 90°	975.5	16760
Average of Titanium Layer	**1447**	**21500**

The original data for the seven measurement points mentioned above are present below.

Stainless-Steel-Substrate.MMD

RCa: -3502 mm

2015-05-06 15:47:35 RCb: 1569 mm

Op: Brian Yates

Area: 1.245 mm x 0.934 mm Wave

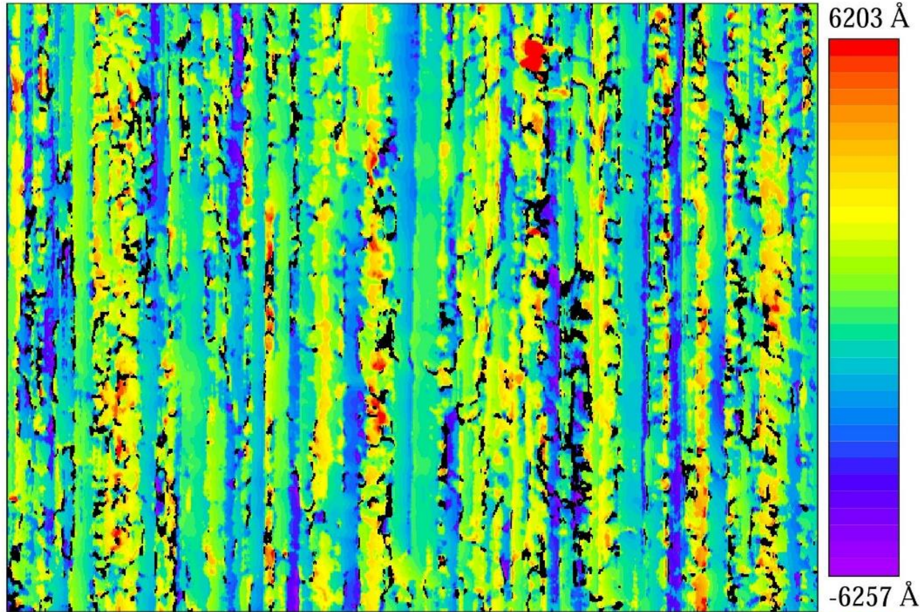

Sq: 2077 Å

Sa: 1590 Å

St: 22960 Å

Sdq: 49.98 mR

QUARTIC

Points: 282639

640x480

520 white

5X

Reference Off

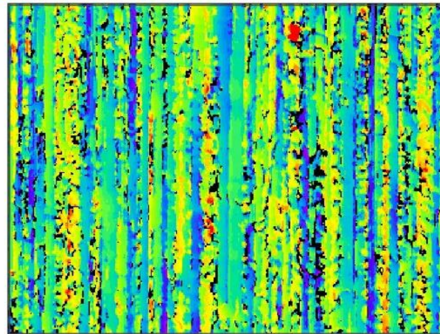

Polyimide-30 microns-over-Stainless-Steel-Substrate.MMD

		RCa:	-8487 mm
2015-05-06 15:38:11		RCb:	-2000 mm
Op:	Brian Yates		
Area:	1.245 mm x 0.934 mm	Wave	

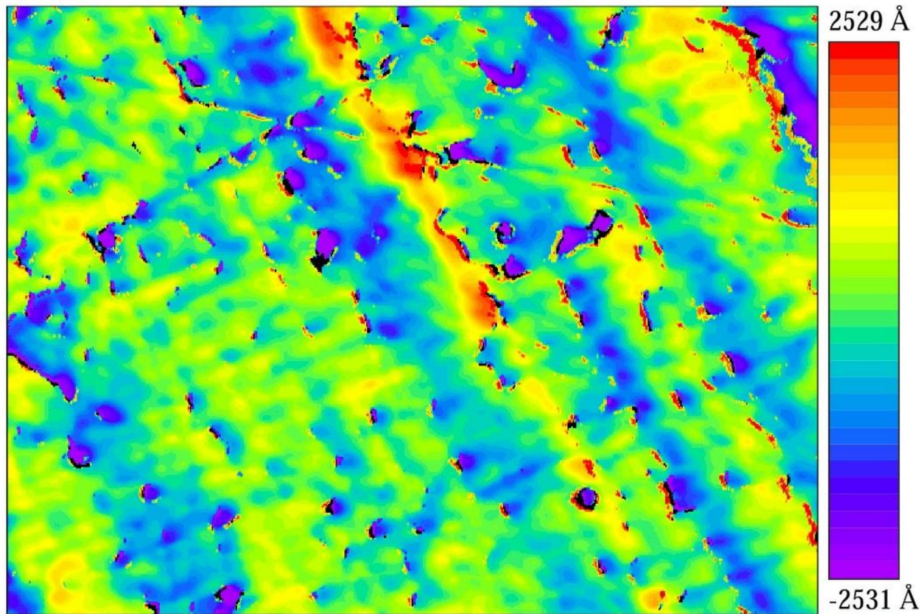

Sq: 843.3 Å
Sa: 596.9 Å
St: 15620 Å

Sdq: 20.61 mR
QUARTIC
Points: 304523
640x480
520 white
5X
Reference Off

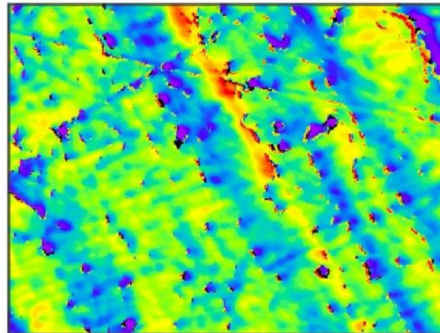

Ti-1.5micron-over-Polyimide-30 microns-middle.MMD

RCa: -333.7 mm

2015-05-06 14:25:09 RCb: -103.9 mm

Op: Brian Yates

Area: 1.245 mm x 0.934 mm Wave

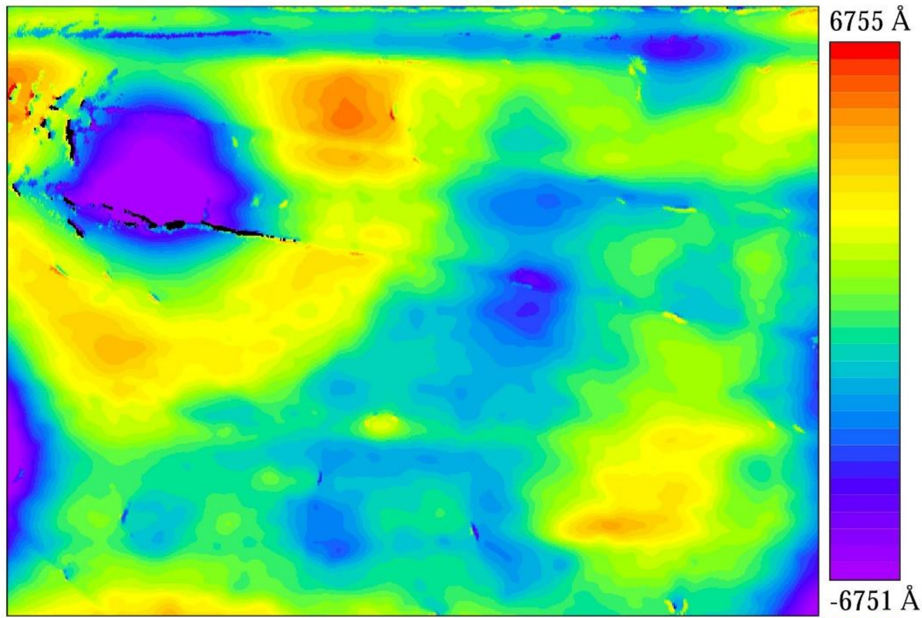

Sq: 2251 Å
Sa: 1693 Å
St: 22750 Å

Sdq: 14.15 mR
QUARTIC
Points: 306494
640x480
520 white
5X
Reference Off

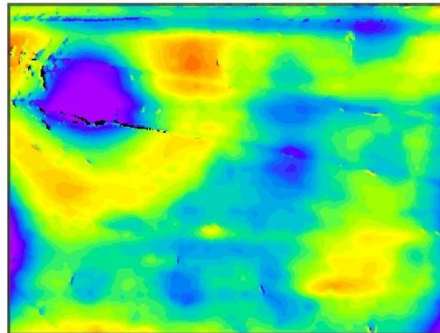

Ti-1.5micron-over-Polyimide-30 microns-R-25mm.MMD

RCa: 359.2 mm
2015-05-06 14:48:08 RCb: -149.9 mm
Op: Brian Yates
Area: 1.245 mm x 0.934 mm Wave

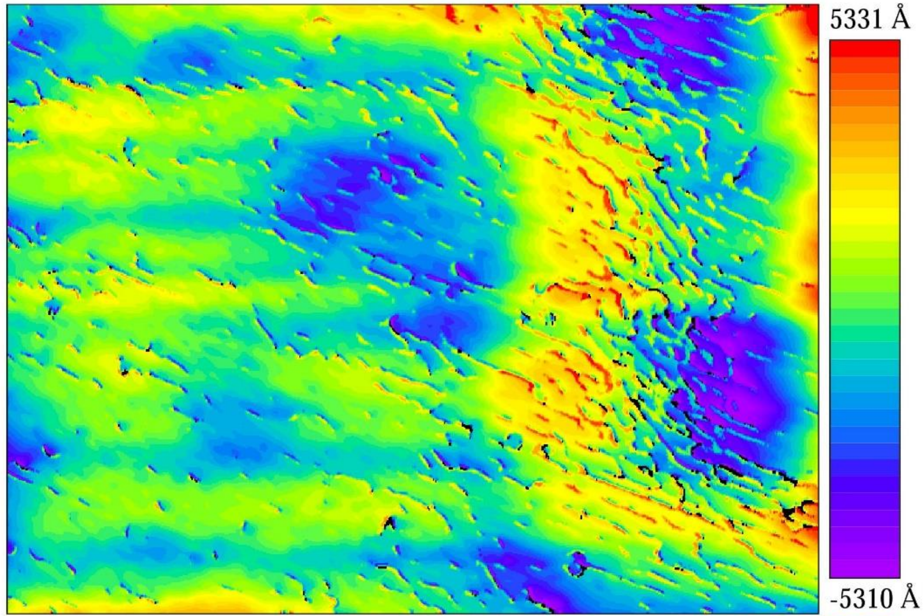

Sq: 1774 Å
Sa: 1346 Å
St: 18560 Å

Sdq: 36.40 mR
QUARTIC
Points: 304675
640x480
520 white
5X
Reference Off

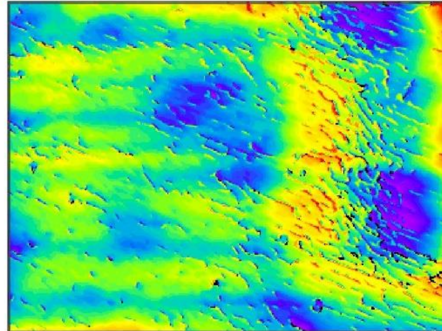

Ti-1.5micron-over-Polyimide-30 microns-R-25mm-90degrees.MMD

2015-05-06 15:02:26

Op: Brian Yates

Area: 1.245 mm x 0.934 mm

RCa: -483.0 mm

RCb: -166.3 mm

Wave

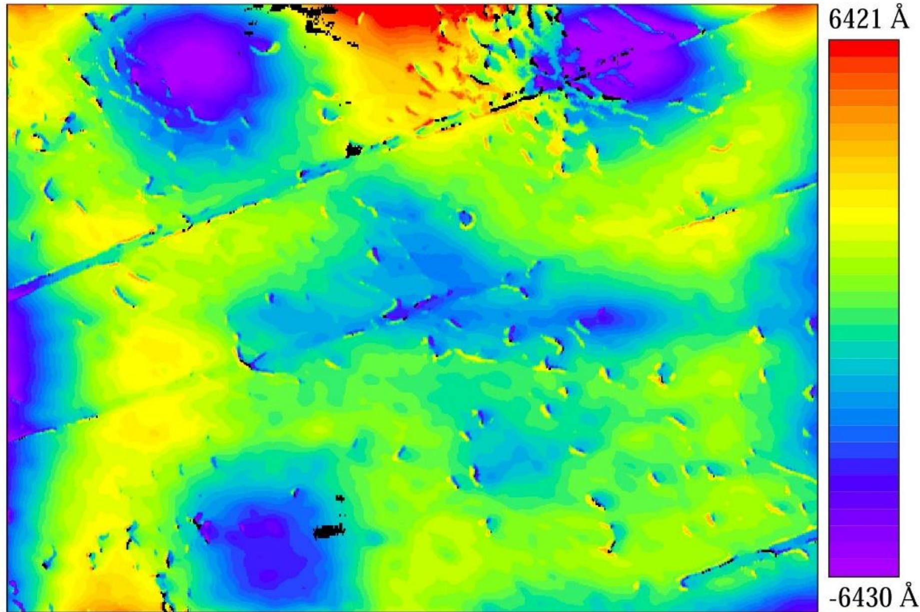

6421 Å

-6430 Å

Sq: 2142 Å

Sa: 1598 Å

St: 23550 Å

Sdq: 24.92 mR

QUARTIC

Points: 305015

640x480

520 white

5X

Reference Off

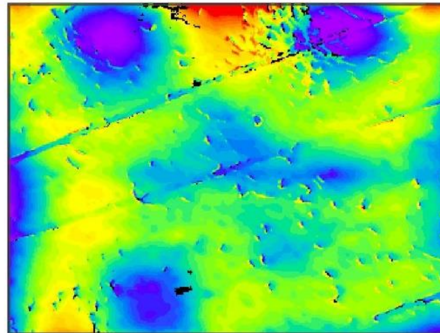

Ti-1.5micron-over-Polyimide-30 microns-R-45mm.MMD

	RCa: 10360 mm
2015-05-06 14:55:55	RCb: -115.3 mm
Op: Brian Yates	
Area: 1.245 mm x 0.934 mm	Wave

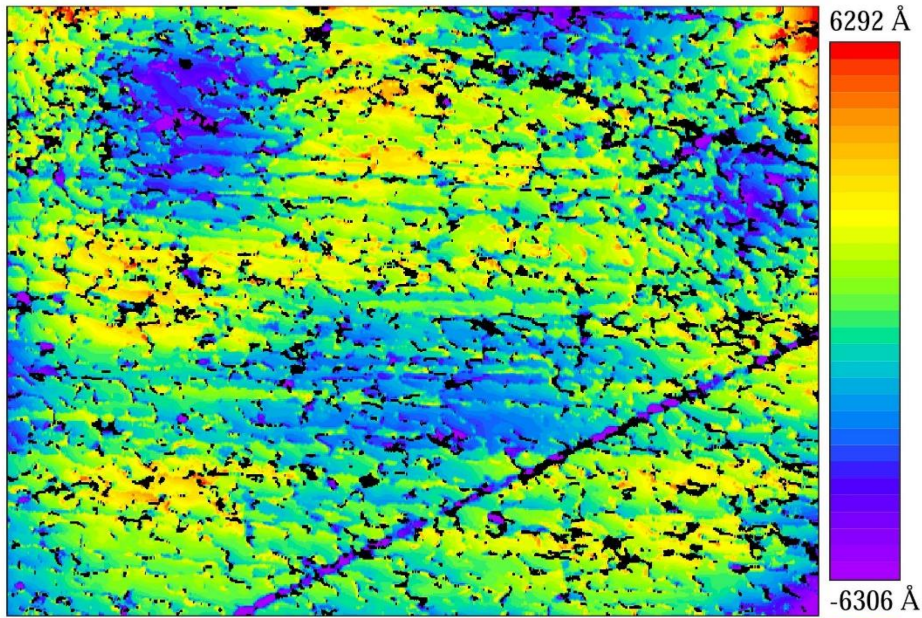

Sq: 2100 Å
Sa: 1622 Å
St: 25880 Å

Sdq: 43.16 mR
QUARTIC
Points: 271823
640x480
520 white
5X
Reference Off

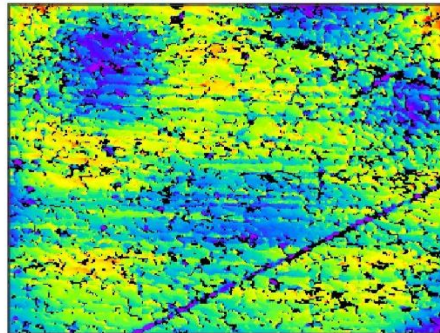

Ti-1.5micron-over-Polyimide-30 microns-R-45mm-90degrees.MMD

RCa: -2983 mm

2015-05-06 15:16:05 RCb: -256.0 mm

Op: Brian Yates

Area: 1.245 mm x 0.934 mm Wave

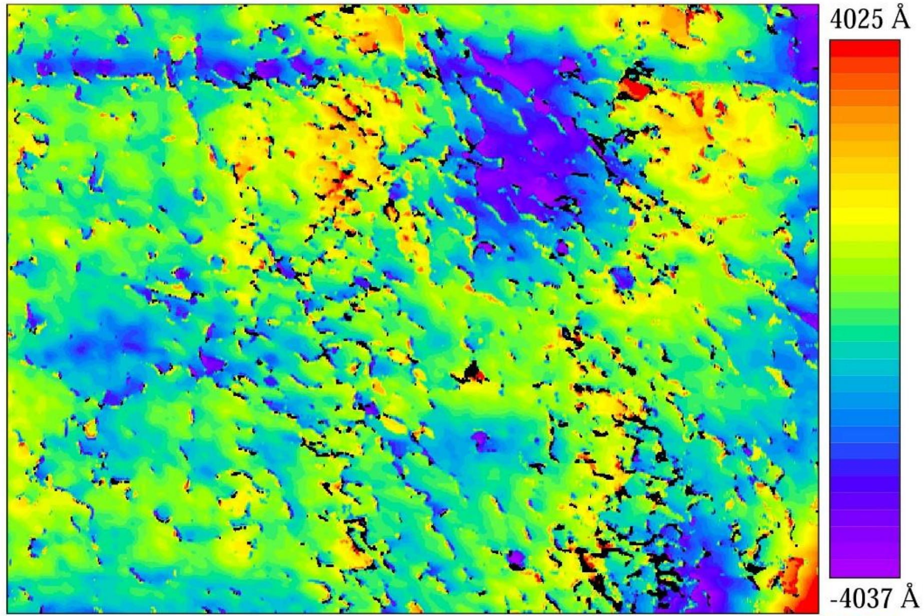

Sq: 1344 Å

Sa: 979.5 Å

St: 16760 Å

Sdq: 34.00 mR

QUARTIC

Points: 295673

640x480

520 white

5X

Reference Off

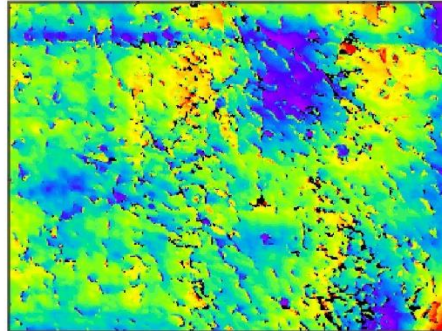

APPENDIX C

CALCULATIONS OF 100 MBAR HELIUM GAS PROPERTIES AND DIMENSIONLESS NUMBERS

The equations to calculate relevant conditions associated with the 100 mbar helium buffering gas atmosphere in the scanner working chamber are derived from [79]. The modelling parameters used in the calculations are presented in Table C.1.

Table C.1: Modelling parameters for helium gas calculations

Ambient pressure of helium gas, P	Ambient temperature of helium gas, T_∞	Specific heat capacity of helium gas, c_p	Distance of the proximity gap, d	Relative velocity of helium gas, V	Reference temperature, T_0
100 mbar	291.15 K/18°C	5193 J/kg/K	1.4 mm	50 mm/s	273.15 K

C.1 Calculation of the Knudsen Number K_n of 100 mbar Helium at 18°C:

The Knudsen number is a dimensionless number used to judge the validation of the continuum assumption. The characteristics of individual molecules/atoms are ignored, but the macroscopic effect of the gas molecules/atoms is studied in the continuum model. The molecular-mean-free path (λ) is compared to the characteristic dimension of the system, which is the proximity gap distance in this case: If this ratio is low, the number of helium atoms within the control volume is large enough to be statistically meaningful, and continuum fluid behavior can be assumed [80].

In the ideal gas law $PV=NRT$, N represents the amount of substance, R is the gas constant $R= 8.314\cdot10^{-5}$ $m^3\cdot bar/K\cdot mol$, and the Avogadro constant is $N_0= 6.023\cdot10^{23}$ mol^{-1}. With the atomic diameter (σ) for helium of $\sigma = 3.74\cdot10^{-10}$ m, the gas law can be expressed as

$$\frac{N}{V} = \frac{PN_0}{RT_\infty} = 2.488\times10^{23}$$

$$\lambda = \frac{1}{\sqrt{2}\cdot\pi\cdot\left(\frac{N}{V}\right)\cdot\sigma^2} = 6.468\times10^{-6}\,\text{m} = 6.468\,\mu\text{m}$$ - Mean free path of 100 mbar helium gas at 18°C

$$K_n = \frac{\lambda}{d} = 4.620\times10^{-3}$$

Since the Knudsen number is within the interval of 0 to 0.1, continuum fluid mechanics with a slip flow condition should be applied, where a relative velocity exists between the fluid and channel surface [81].

C.2 Calculation of the 100 mbar Helium Density *ρ* at 18°C:

$$\rho = 0.17623\frac{P}{(T_\infty / T_0)}\left[1 + 0.53\times10^{-3}\frac{P}{(T_\infty / T_0)^{1.2}}\right]^{-1} \text{kg/m}^3 = 0.01652\text{kg/m}^3$$

C.3 Calculation of the Dynamic Viscosity *μ* and Kinematic Viscosity *v* of 100 mbar Helium at 18°C:

$$\mu = 1.885\times10^{-5}(T_\infty / T_0)^{0.7}\text{kg/m/s} = 1.950\times10^{-5}\text{kg/m/s}$$

$$\upsilon = \frac{\mu}{\rho} = 1.180\times10^{-3}\text{m}^2\text{/s}$$

C.4 Calculation of the Thermal Conductivity *k* of 100 mbar Helium Gas at 18°C:

$$k = 0.144(1 + 2.7\times10^{-4}P)(T_\infty / T_0)^{0.71(1-2\times10^{-4}P)}\text{W/m/K} = 0.1507\text{W/m/K}$$

C.5 Calculation of the Prandtl Number *Pr* and the Thermal Diffusivity *α* of 100 mbar Helium at 18°C:

The Prandtl number is a dimensionless number, defined as the ratio of momentum diffusivity with respect to thermal diffusivity. For most gases, the Prandtl number is around 0.7. The thermal diffusivity α can be expressed in terms of the Prandtl number Pr and the kinematic viscosity v:

$$Pr = c_p\frac{\mu}{k} = 0.6724$$

$$\alpha = \frac{\upsilon}{Pr} = 1.755\times10^{-3}\text{m}^2\text{/s}$$

C.6 Calculation of the Reynolds Number Re_D and the Rayleigh Number Ra_D of 100 mbar Helium at 18°C:

The Reynolds number is a dimensionless number to judge the domain of fluid flow. If the flow is characterized by random fluctuations in velocity, temperature, pressure, and density, it is referred to as turbulent. In the absence of such fluctuations the flow is laminar.

For a fluid moving between two plane parallel surfaces, where the width of the surfaces is much greater than the separation of the plates, the characteristic dimension is twice the separation of the plates [82]. The Reynolds number of the 100 mbar Helium gas flow in the proximity gap therefore is based on the characteristic dimension of twice the distance of the proximity gap, which is $D = 2d = 2.8$ mm.

$$Re_D = \frac{VD}{\upsilon} = 0.1186$$

The critical Reynolds number for a fluid moving between plane parallel surfaces depends on environmental conditions, but is on the order of 10^5 to 10^6. At smaller Reynolds numbers, the flow is laminar, and turbulent at Reynolds numbers exceeding the critical Reynolds number. For the rarefied helium gas in this study, with a very small Reynolds number of about 0.1, the domain of the flow is laminar.

Assuming that the maximum temperature in the mask surface is T_s=50°C=323.15 K, the temperature difference to the scanner cooled to 18°C becomes ΔT=32 K. The film temperature T_f= $(T_f + T_\infty)/2$= (50+18) °C/2=39°C=307.15 K.

Volumetric thermal expansion coefficient for ideal gas: $\beta = -\frac{1}{\rho}(\frac{\partial \rho}{\partial T})_p = \frac{1}{\rho}\frac{p}{RT^2} = \frac{1}{T_f} = 3.256\times 10^{-3}$

The Rayleigh number indicates the relative importance of buoyancy forces to viscous dissipation and diffusion forces. At low Rayleigh number, heat transfer is primarily through conduction, rather than natural convection.

$$Ra_D = \frac{\beta g D^3 \Delta T}{\alpha \upsilon} = 1.083\times 10^{-2}$$

At such low Rayleigh numbers, the fluid remains stagnant, and heat transfers through the proximity gap by conduction [80].

C.7 Determination of the Time Step τ for Transient Thermal Simulation:

$$\tau = \frac{D}{\sqrt{\beta g D \Delta T}} = 0.052\text{sec} \rightarrow \Delta t = \frac{\tau}{4} = 0.013\text{sec} = 13\text{msec}$$ [83]

C.8 Determination of the Heat Transfer Coefficient *h* of the Polyimide Membrane:

The polyimide membrane is exposed to the helium gas in the exposure window, where heat in the mask can dissipate into the helium environment. To find the heat transfer coefficient *h*, the Rayleigh and Nusselt numbers needed to be evaluated. The Nusselt number is a dimensionless heat transfer coefficient, which describes the ratio of convective to conductive heat transfer across the boundary of the control volume. With the length of the polyimide membrane surface (diameter of the exposure window): L=83 mm=0.083 m and the Rayleigh number as explained above, but now calculated for the length L rather than the characteristic dimension D of the proximity gap,

$$Ra_L = \frac{\beta g L^3 \Delta T}{\alpha \upsilon} = 235.1$$

$$\overline{Nu_L} = \left[\frac{Pr}{2.435 + 4.884 Pr^{1/2} + 4.953 Pr} \right]^{1/4} \left(Ra_L \right)^{1/4} = 2.006$$ - Average Nusselt number of vertical plate

$$h_{conv} = \frac{\overline{Nu_L} k}{L} = 3.783 \text{W/m}^2/\text{K}$$

APPENDIX D

LEX-D CALCULATION FOR THE POWER ABSORPTION IN DIFFERENT MATERIAL LAYERS

The powers absorbed in the different layers of material are needed as input data for the thermal simulations. The results are calculated by the software LEX-D (LIGA Exposure-Development) from Sandia National Labs, Livermore, USA, which given by the difference between power input and output through the material layer. The input and output power densities are obtained in terms of the unit power Watt with respect to unit horizontal increment of 1 mrad with 17 m beam trajectory from bending magnet (e.g. 1.7 cm wide at the exposed sample in horizontal direction) per mA beam current, as well as the unit power Watt at 200 mA beam current per cm horizontal increment at sample. The standard beam current assumed in the LEX-D calculation is 200 mA. The obtained power densities can be proportionally adjusted to the exact electron beam current for each simulation. The power absorption rates are calculated based on the uniform beam width of 83 mm (8.3 cm). The results for absorbed power taking into account the intensity chopper with 25% open duty cycle (bold values in the table below) are used in the User Defined Functions (UDFs) for ANSYS FLUENT® in the thesis. The absorbed powers in each material layer for different simulation cases are presented in Table D.1.

Table D.1: LEX-D results for power absorption in different material layers

Simulation Cases	Material Layers	Power IN [W/mrad/mA]	Power IN [W/cm]	Power OUT [W/mrad/mA]	Power OUT [W/cm]	Power Absorption [W/cm] at current of	Power Absorption [W/8.3cm] at current of	Power Absorption with 25% Chopper [W/8.3 cm]
						200 mA		
Chapter 3	80 µm Nickel	0.0662	7.784	0.0069	0.814	6.970	57.85	**14.46**
	30 µm Polyimide			0.0653	7.684	0.100	0.830	**0.207**
Chapter 5: 250 µm PMMA	80 µm Nickel	0.0585	6.921	0.0002	0.0235	6.898	57.25	**14.31**
	30 µm Polyimide			0.0511	6.048	0.873	7.246	**1.811**
	250 µm PMMA	0.0511	6.048	0.0323	3.817	2.231	18.52	**4.629**
	500 µm Silicon Wafer	0.0323	3.817	0.0009	0.106	3.711	30.80	**7.700**
Chapter 5: 500 µm PMMA	80 µm Nickel	0.0870	10.29	0.0071	0.838	9.452	78.45	**19.61**
	30 µm Polyimide			0.0846	10.00	0.290	2.407	**0.602**
	500 µm PMMA	0.0846	10.00	0.0655	7.743	2.257	18.73	**4.683**
	500 µm Silicon Wafer	0.0655	7.743	0.0210	2.478	5.265	43.70	**10.92**

APPENDIX E

USER DEFINED FUNCTIONS (UDF) IN THE ANSYS FLUENT SIMULATION

E.1 UDF for the Thermal Simulation in Chapter 3:

```
#include "udf.h"

#define FLUXC 9.2892e10 /*to define the internal heat generation in the unit of W/µm/m^2*/

static real ymin=-0.0044,ymax=0.0044,ym=0.0,vv=-0.05; /*to define the geometry, starting position, and
velocity of beam*/

static real tt1=0.0; /*to define the initial time*/

DEFINE_PROFILE(flux,tf,i) /* to define a custom boundary profile that varies as a function of spatial
coordinates and time.*/

    {

        face_t f; /*index that a wall face*/

        real tt,xc[ND_ND],det; /*to define variable declarations, xc will hold the position
        vector*/

        tt=CURRENT_TIME; /*real current flow time (in seconds)*/

        det=tt-tt1; /*to define time step*/

        tt1=tt; /*renewed flow time*/

        ymin=ymin+vv*det; /*displacement of the beam at each time step*/

        ymax=ymax+vv*det;

        ym=ym+vv*det;

        if(ymin>=0.04775)vv=-0.05; /*to define scanning range of the beam and reciprocal
        motion*/

        if(ymax<=-0.04775)vv=0.05;

        begin_f_loop(f,tf)

            {

                F_CENTROID(xc,f,tf); /*centroid is defined to specify position
                dependent profiles*/
```

```
if(fabs(xc[1])<=0.0375&&sqrt(xc[0]*xc[0]+xc[1]*xc[1])<=0.0415&&xc
[1]<=ymax&&xc[1]>=ymin) /*to define the boundary of heat flux*/
            {
            F_PROFILE(f,tf,i) =FLUXC;
            }
        else
            {
            F_PROFILE(f,tf,i) =0.0;
            }
    }
    end_f_loop(f,tf)
}
```

E.2 UDF for the DXRL Exposure Thermal Simulation in Chapter 5:

```
#include "udf.h"
#define FLUXC 0.6451e10
static real ymin=-0.0044,ymax=0.0044,ym=0.0,vv=-0.05;
static real tt1=0.0;
DEFINE_PROFILE(flux,tf,i)
    {
        face_t f;
        real tt,xc[ND_ND],det;
        tt=CURRENT_TIME;
        det=tt-tt1;
        tt1=tt;
        ymin=ymin+vv*det;
        ymax=ymax+vv*det;
```

```
		ym=ym+vv*det;
		if(ymin>=0.04775)vv=-0.05;
		if(ymax<=-0.04775)vv=0.05;
		begin_f_loop(f,tf)
			{
				F_CENTROID(xc,f,tf);
				if(fabs(xc[1])<=0.0375&&sqrt(xc[0]*xc[0]+xc[1]*xc[1])<=0.0415&&xc
				[1]<=ymax&&xc[1]>=ymin&&(fabs(xc[0])+fabs(xc[1]))>=0.03) /*to
				define the boundary of heat flux on PMMA/wafer, considering the layout
				of center block absorber*/
				{
					F_PROFILE(f,tf,i) =FLUXC;
				}
				else
				{
					F_PROFILE(f,tf,i) =0.0;
				}
			}
	end_f_loop(f,tf)
	}
```

APPENDIX F

TEMPERATURE MEASUREMENTS FOR THE TEST MASKS

F.1 Measurements for the Complete Coverage Test Mask

The measurement results for each test are presented below:

Test 1:

I = 218.5 mA, 10% chopper, with pre-absorbers; calculated incident beam power $P_{LEX\text{-}D}$ = 6.32 W

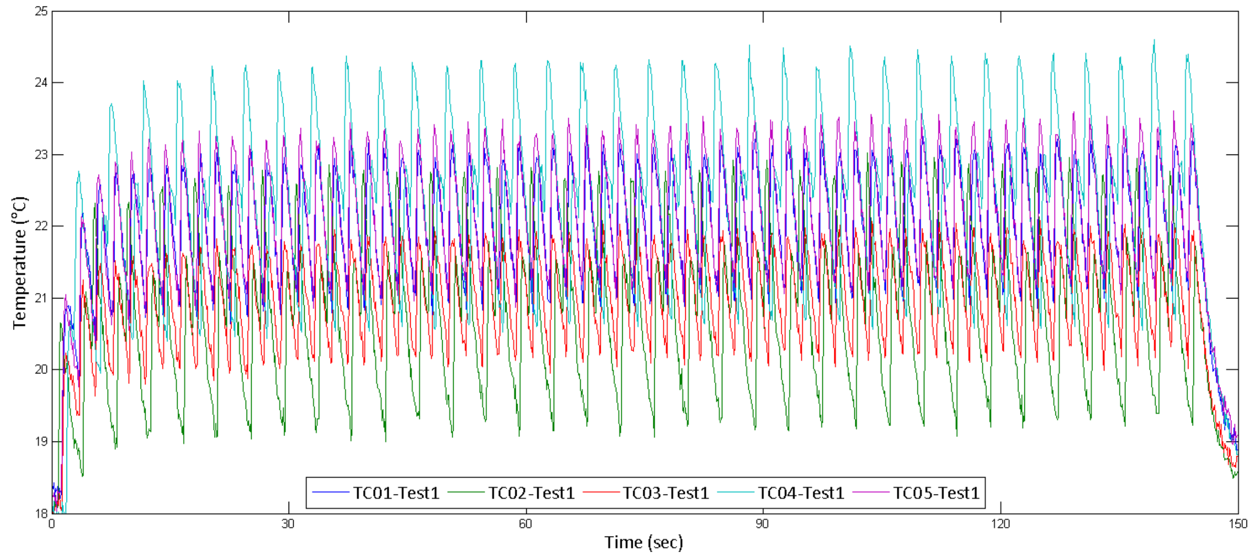

Test 2:

I = 235.5 mA, 10% chopper, without pre-absorbers; calculated incident beam power $P_{LEX\text{-}D}$ = 11.91 W

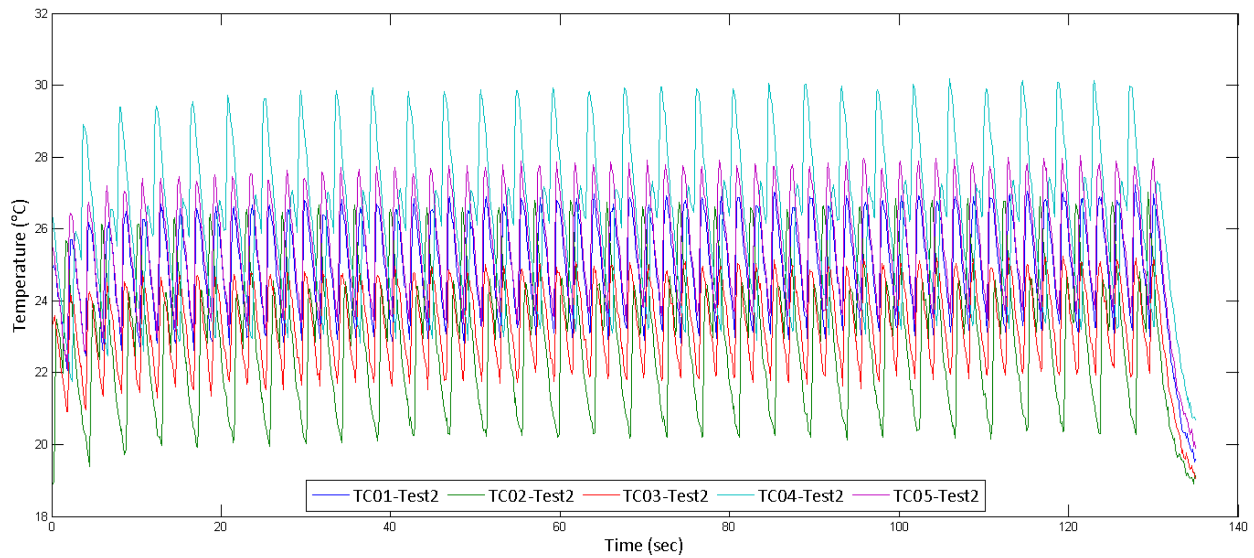

Test 3:

I = 178.2 mA, 10% chopper, with pre-absorbers; calculated incident beam power $P_{LEX\text{-}D}$ = 12.89 W

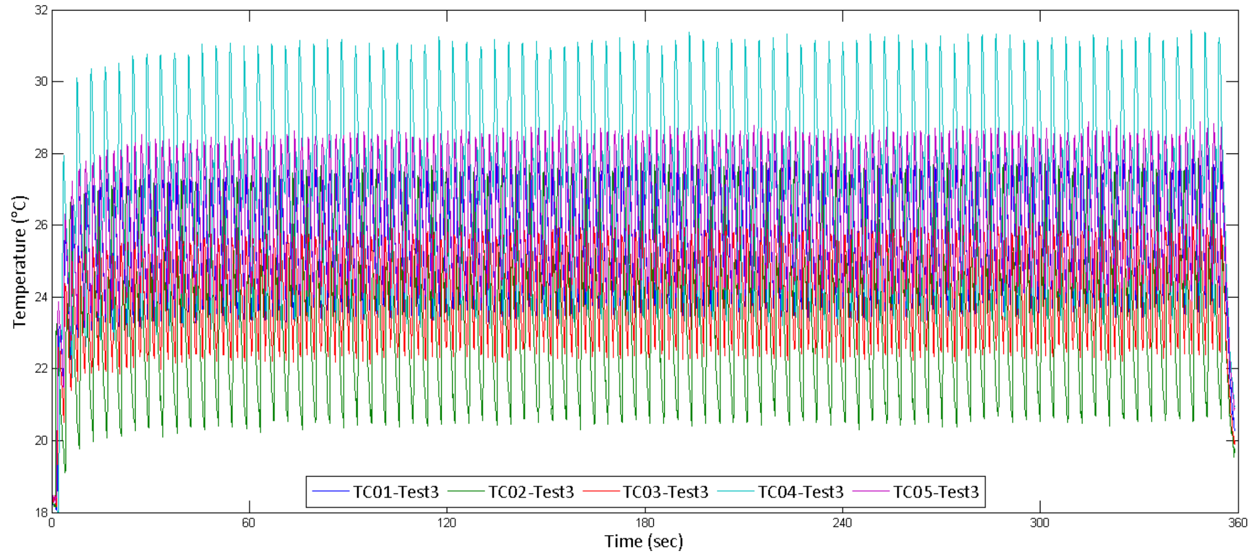

Test 4:

I = 202.6 mA, 10% chopper, with pre-absorbers; calculated incident beam power $P_{LEX\text{-}D}$ = 14.65 W

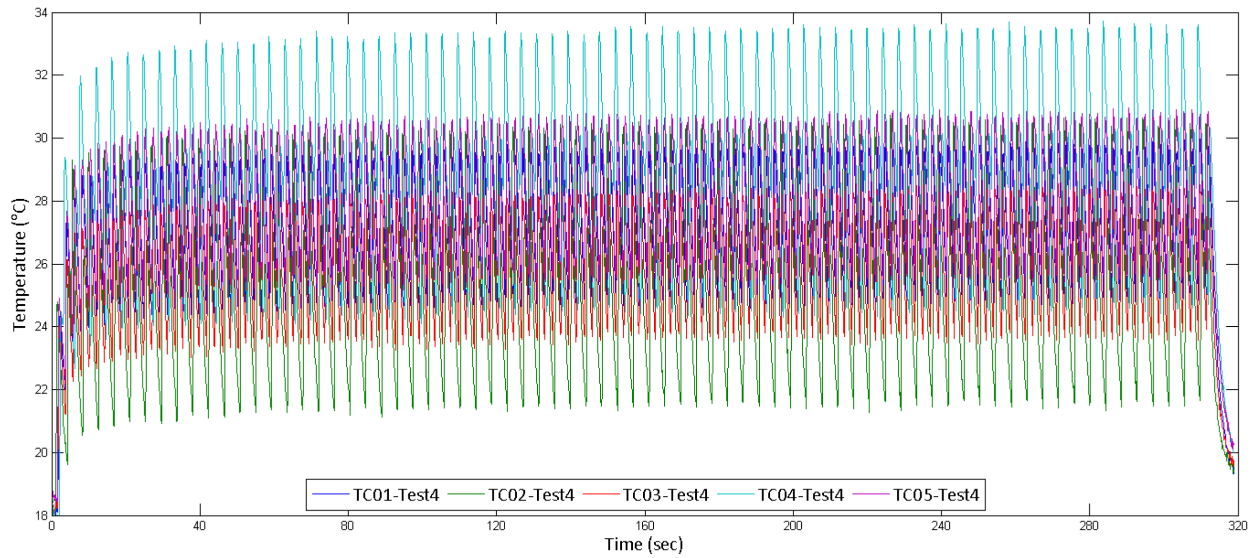

Test 5:

I = 219.6 mA, 10% chopper, with pre-absorbers; calculated incident beam power $P_{LEX\text{-}D}$ = 15.88 W

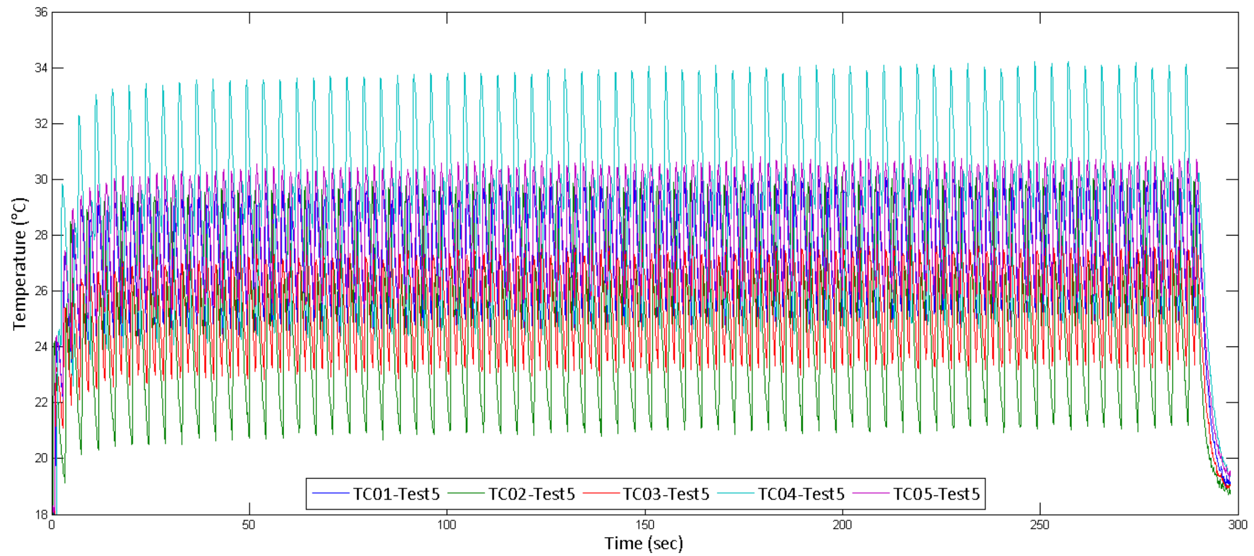

Test 6:

I = 233.2 mA, 10% chopper, with pre-absorbers; calculated incident beam power $P_{LEX\text{-}D}$ = 16.86 W

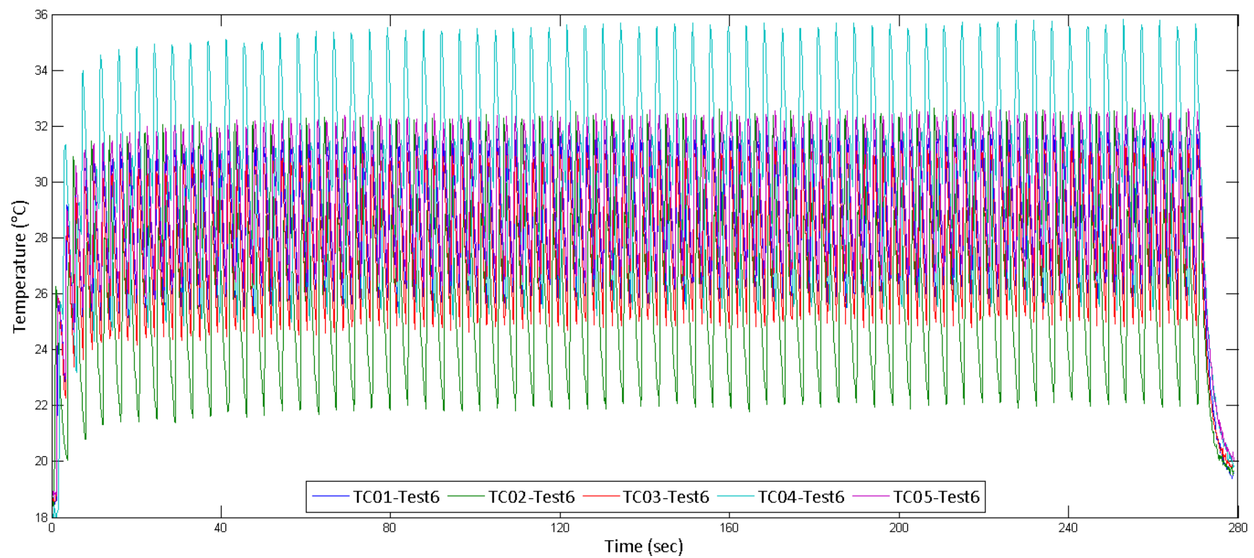

Test 7:

I = 222.3 mA, 10% chopper, without pre-absorbers; calculated incident beam power P_{LEX-D} = 28.10 W

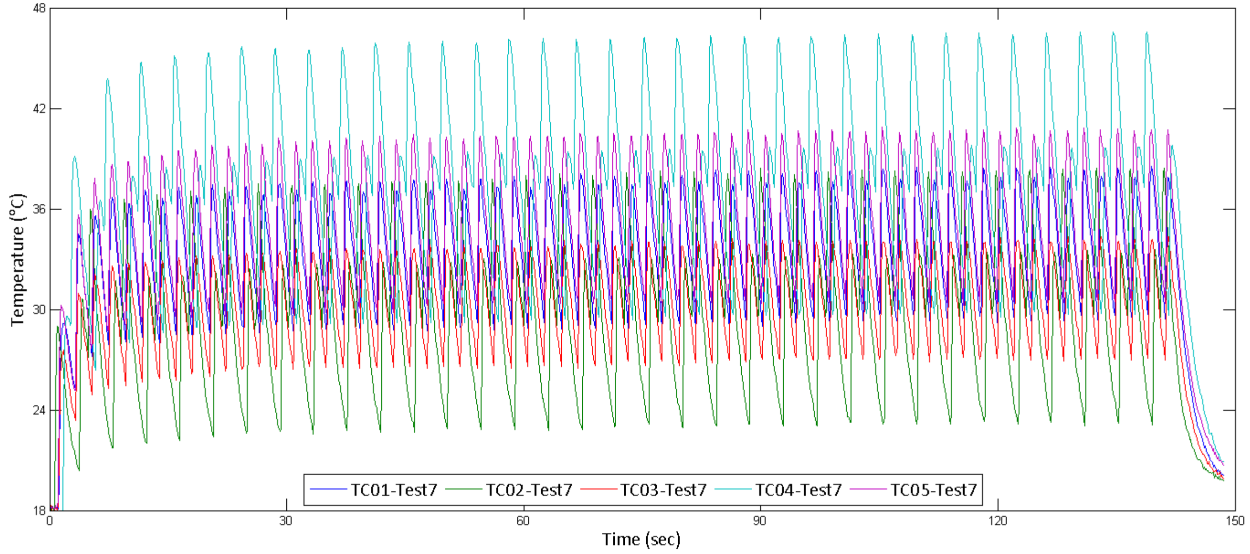

F.2 Measurements for the Center Block Test Mask

The measurement results for each test are presented below:

Test 1:

I = 214.3 mA, 10% chopper, with pre-absorbers; calculated incident beam power P_{LEX-D} = 6.20 W

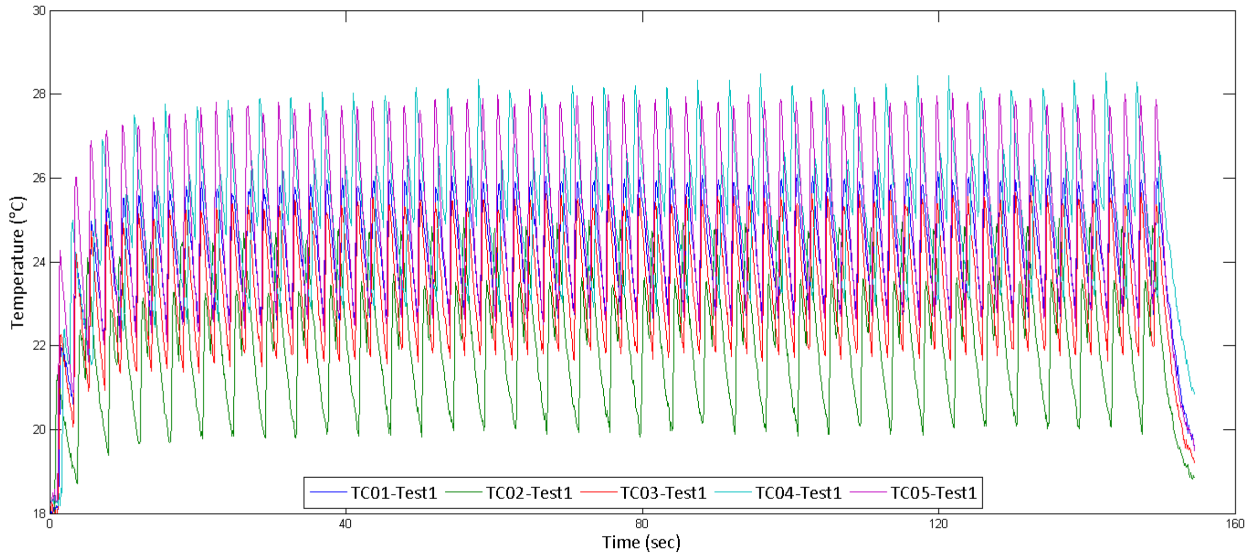

Test 2:

I = 210.6 mA, 10% chopper, without pre-absorbers; calculated incident beam power $P_{LEX\text{-}D}$ = 10.65 W

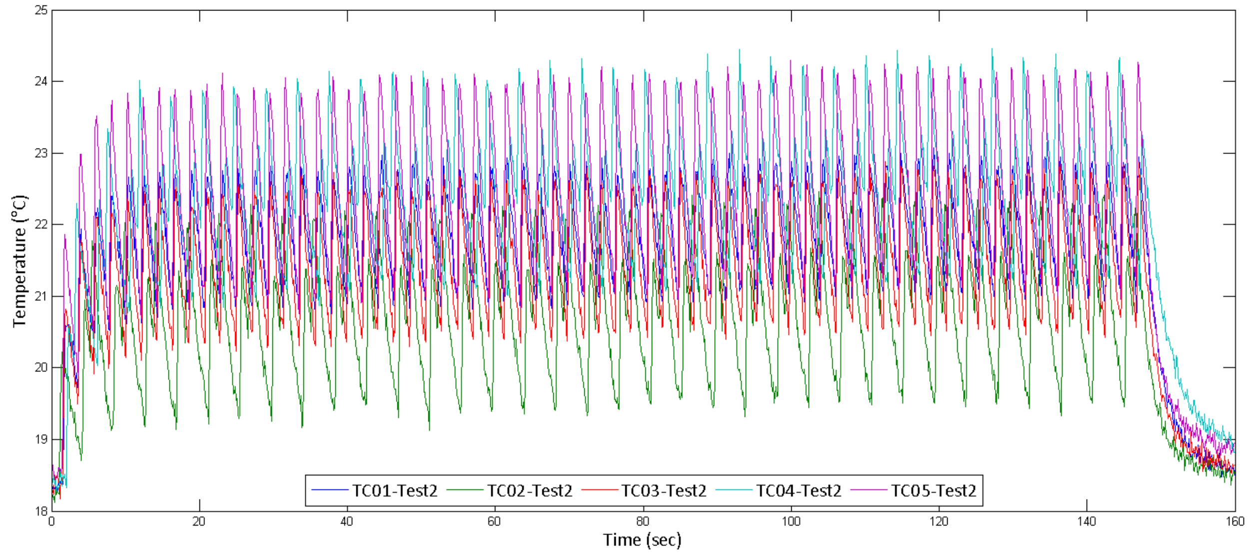

Test 3:

I = 182.6 mA, 25% chopper, with pre-absorbers; calculated incident beam power $P_{LEX\text{-}D}$ = 13.13 W

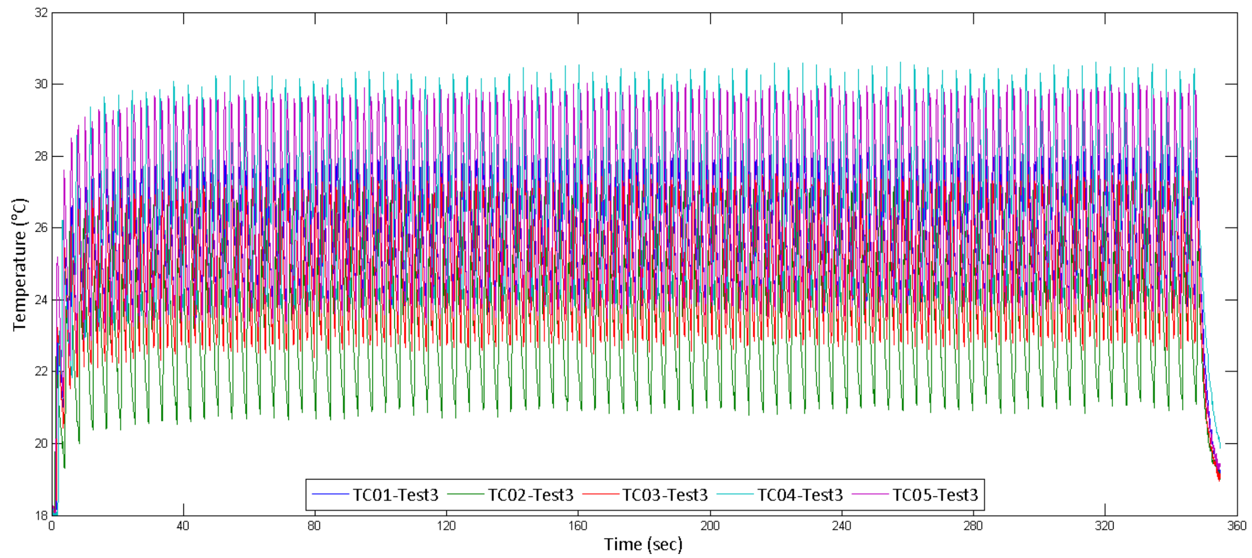

Test 4:

I = 188.8 mA, 25% chopper, with pre-absorbers; calculated incident beam power $P_{LEX\text{-}D}$ = 13.65 W

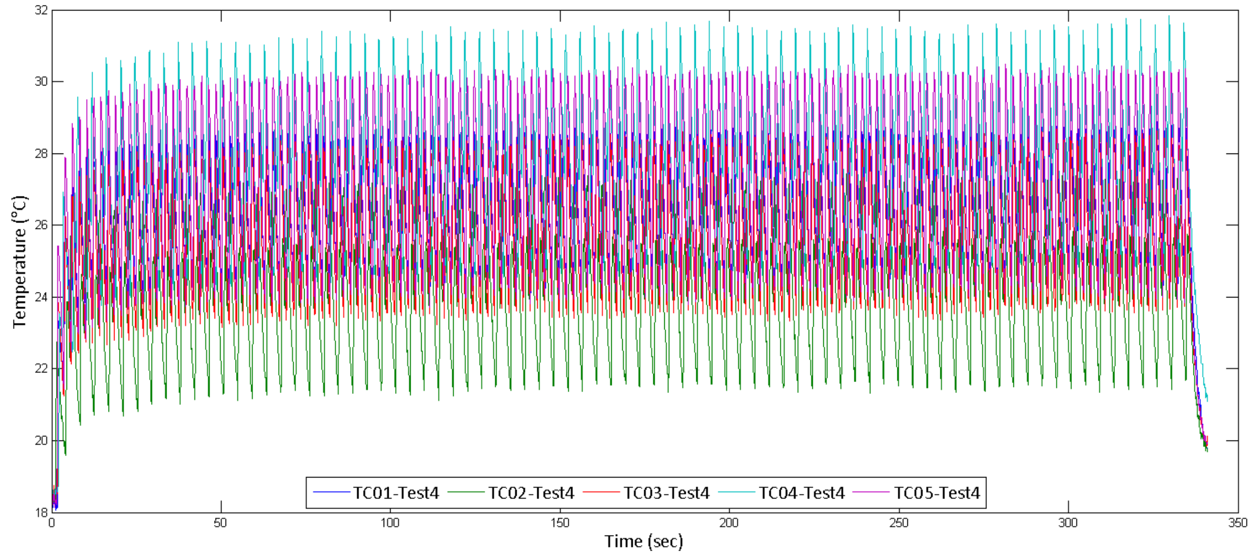

Test 5:

I = 206.2 mA, 25% chopper, with pre-absorbers; calculated incident beam power $P_{LEX\text{-}D}$ = 14.91 W

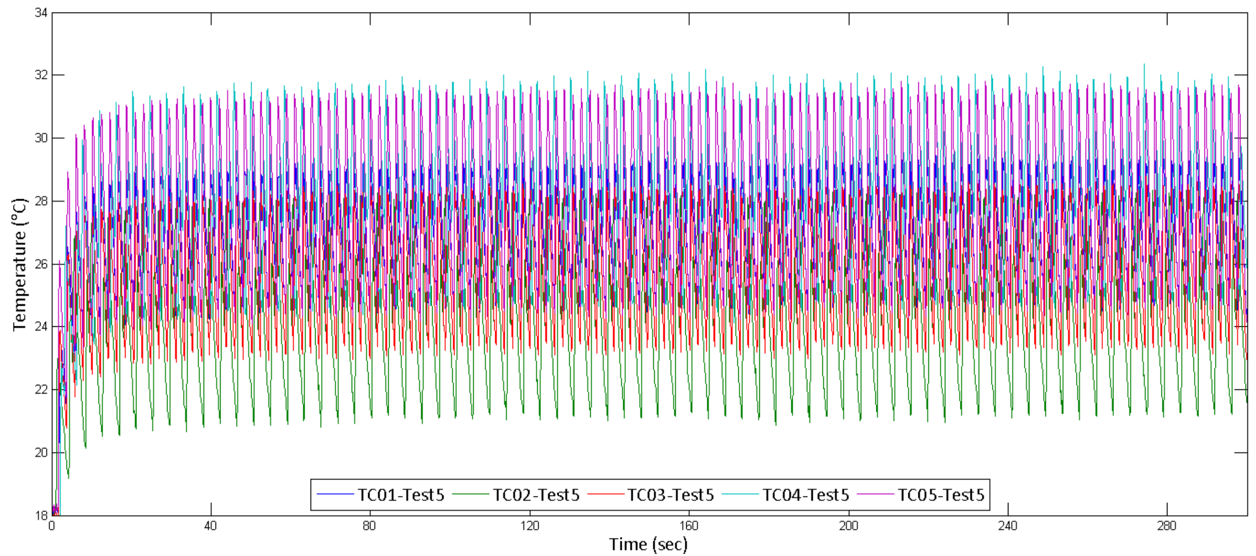

Test 6:

I = 238.4 mA, 25% chopper, with pre-absorbers; calculated incident beam power $P_{LEX\text{-}D}$ = 17.24 W

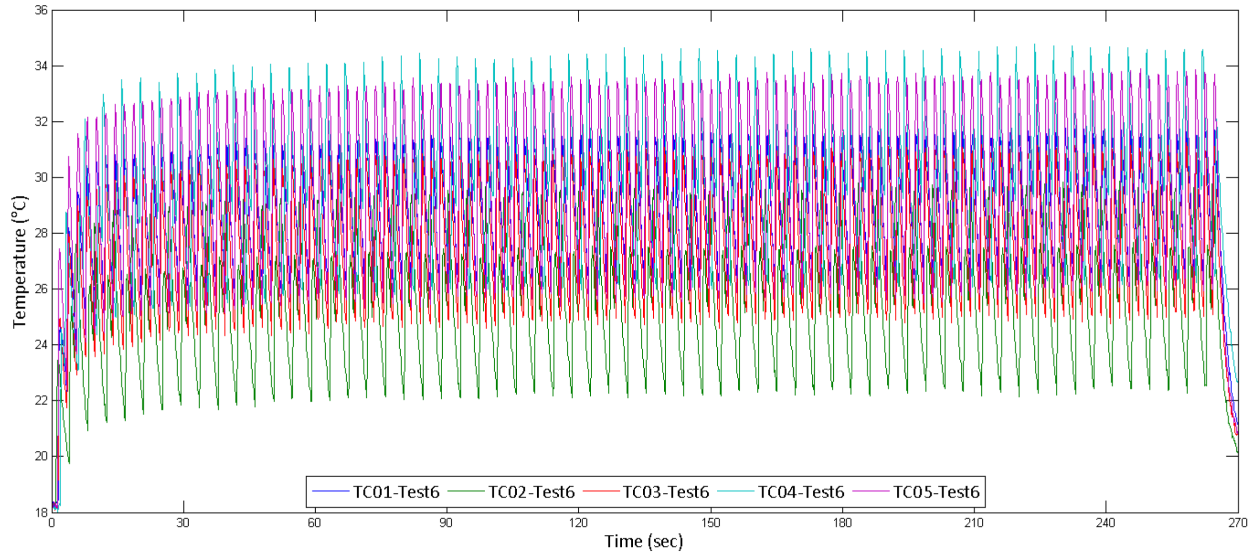

Test 7:

I = 207.7 mA, 25% chopper, without pre-absorbers; calculated incident beam power $P_{LEX\text{-}D}$ = 26.25 W

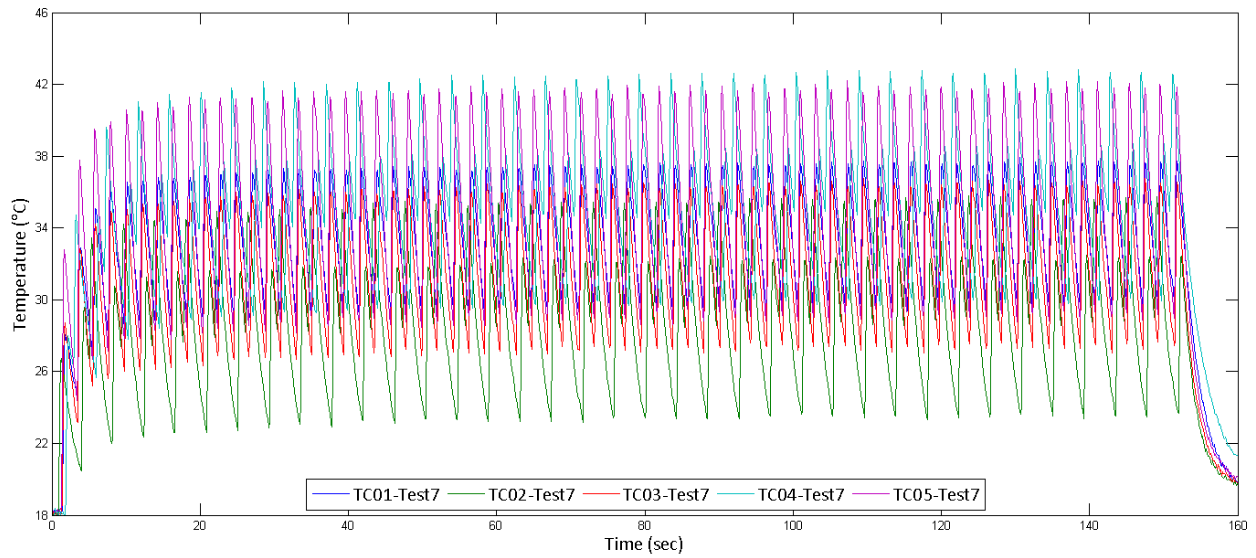

BIBLIOGRAPHY

[1] J. S. Greeneich, “X-ray lithography: Part I. Design criteria for optimizing resist energy absorption; Part II. Pattern replication with polymer masks,” *IEEE Trans. Electron Devices*, vol. 22, no. 7, pp. 434–439, Jul. 1975.

[2] E. Spiller and R. Feder, “X-Ray Lithography,” in *X-Ray Optics*, vol. 22, H.-J. Queisser, Ed. Berlin, Heidelberg: Springer Berlin Heidelberg, 1977.

[3] E. W. Becker, W. Ehrfeld, D. Münchmeyer, H. Betz, A. Heuberger, S. Pongratz, W. Glashauser, H. J. Michel, and R. v. Siemens, “Production of separation-nozzle systems for uranium enrichment by a combination of X-ray lithography and galvanoplastics,” *Naturwissenschaften*, vol. 69, no. 11, pp. 520–523, Nov. 1982.

[4] E. Spiller, D. E. Eastman, R. Feder, W. D. Grobman, W. Gudat, and J. Topalian, “Application of synchrotron radiation to x-ray lithography,” *J. Appl. Phys.*, vol. 47, no. 12, pp. 5450–5459, 1976.

[5] U. Wallrabe, *MEMS: A Practical Guide to Design, Analysis, and Applications*. Berlin, Heidelberg: Springer Berlin Heidelberg, 2006.

[6] E. W. Becker, W. Ehrfeld, P. Hagmann, A. Maner, and D. Münchmeyer, “Fabrication of microstructures with high aspect ratios and great structural heights by synchrotron radiation lithography, galvanoforming, and plastic moulding (LIGA process),” *Microelectron. Eng.*, vol. 4, no. 1, pp. 35–56, May 1986.

[7] T. Mappes, S. Achenbach, and J. Mohr, “X-ray lithography for devices with high aspect ratio polymer submicron structures,” *Microelectron. Eng.*, vol. 84, no. 5–8, pp. 1235–1239, May 2007.

[8] H. H. Gatzen, V. Saile, and J. Leuthold, *Micro and Nano Fabrication*. Berlin, Heidelberg: Springer-Verlag Berlin Heidelberg, 2015.

[9] T. R. Christenson and H. Guckel, “X-Ray Lithography for Micromechanics,” *Proceedings of SPIE*, vol. 2639, pp. 134–145, 2005.

[10] D. R. Hines, N. P. Siwak, L. A. Mosher, R. Ghodssi, M. Materials, and P. Handbook, *MEMS Materials and Processes Handbook*, vol. 1. Boston, MA: Springer US, 2011.

[11] T. Christenson, “X-Ray Based Fabrication,” in *MEMS: Design and Fabrication*, M. Gad-el-Hak, Ed. Boca Raton, FL: CRC Press, 2006, pp. 1–53.

[12] J. Mohr, W. Ehrfeld, and D. Münchmeyer, “Analyse der Defektursachen und der Genauigkeit der Strukturübertragung bei der Röngentiefenlithographie mit Synchrotronstrahlung,”

Kernforschungszentrum Karlsruhe, vol. 4414, pp. 1–96, 1988.(in German)

[13] S. Achenbach, F. Pantenburg, and J. Mohr, “Optimierung der Prozeßbedingungen zur Herstellung von Mikrostrukturen durch ultratiefe Röntgenlithographie (UDXRL),” 2000. (in German)

[14] V. Saile, *LIGA and Its Applications*. John Wiley & Sons, 2009.

[15] A. El-Kholi, P. Bley, J. Göttert, and J. Mohr, “Examination of the solubility and the molecular weight distribution of PMMA in view of an optimised resist system in deep etch x-ray lithography,” *Microelectron. Eng.*, vol. 21, no. 1–4, pp. 271–274, Apr. 1993.

[16] V. Nazmov, E. Reznikova, J. Mohr, A. Snigirev, I. Snigireva, S. Achenbach, and V. Saile, “Fabrication and preliminary testing of X-ray lenses in thick SU-8 resist layers,” *Microsyst. Technol.*, vol. 10, no. 10, pp. 716–721, 2004.

[17] F. J. Pantenburg, “Instrumentation for Microfabrication with Deep X-ray Lithography,” in *AIP Conference Proceedings*, 2007, vol. 879, pp. 1456–1461.

[18] F. Pérennès and F. J. Pantenburg, “Adhesion improvement in the deep X-ray lithography process using a central beam-stop,” *Nucl. Instruments Methods Phys. Res. Sect. B Beam Interact. with Mater. Atoms*, vol. 174, pp. 317–323, 2001.

[19] F. J. Pantenburg and J. Mohr, “Influence of secondary effects on the structure quality in deep X-ray lithography,” *Nucl. Instruments Methods Phys. Res. Sect. B Beam Interact. with Mater. Atoms*, vol. 97, no. 94, pp. 551–556, 1995.

[20] B. Maid, “Anpassung der spektralen Verteilung der Synchrotronstrahlung für die Röntgentiefenlithografie.” Kernforschungszentrum Karlsruhe, 1989. (in German)

[21] K. H. Gil, S. S. Lee, and Y. Youm, “Equations of exposure time and X-ray mask absorber thickness in the LIGA process,” *Microsyst. Technol.*, vol. 7, no. 1, pp. 1–5, Mar. 2001.

[22] B. L. Henke, E. M. Gullikson, and J. C. Davis, “X-Ray Interactions: Photoabsorption, Scattering, Transmission, and Reflection at E = 50-30,000 eV, Z = 1-92,” *At. Data Nucl. Data Tables*, vol. 54, no. 2, pp. 181–342, Jul. 1993.

[23] C. K. Malek, K. H. Jackson, W. D. Bonivert, and J. Hruby, “Masks for high aspect ratio x-ray lithography,” *J. Micromechanics Microengineering*, vol. 6, no. 2, pp. 228–235, Jun. 1996.

[24] S. K. Griffiths and A. Ting, “The influence of X-ray fluorescence on LIGA sidewall tolerances,” *Microsyst. Technol.*, vol. 8, no. 2–3, pp. 120–128, 2002.

[25] W. Schomburg, P. Bley, H. Hein, and J. Mohr, “Masken für die Röntgentiefenlithographie,” *VDI*

Berichte, vol. 870, pp. 133–154, 1990. (in German)

[26] D. L. Laird, “Practical considerations in x-ray mask mounting methodology,” *J. Vac. Sci. Technol. B Microelectron. Nanom. Struct.*, vol. 11, no. 1993, p. 2953, 1993.

[27] D. Laird and R. Engelstad, “Predicting out-of-plane distortions during X-ray mask fabrication,” *Microelectron. Eng.*, vol. 30, no. 1–4, pp. 223–226, Jan. 1996.

[28] S. K. Griffiths, “Fundamental limitations of LIGA x-ray lithography: sidewall offset, slope and minimum feature size,” *J. Micromechanics Microengineering*, vol. 14, no. 7, pp. 999–1011, Jul. 2004.

[29] L. Wang, Y. M. Desta, R. K. Fettig, J. Goettert, H. Hein, P. Jakobs, and J. Schulz, “High resolution x-ray mask fabrication by a 100 keV electron-beam lithography system,” *J. Micromechanics Microengineering*, vol. 14, no. 5, pp. 722–726, 2004.

[30] W. Dai and R. Nassar, “A three-dimensional numerical method for thermal analysis in X-ray lithography,” *Int. J. Numer. Methods Heat Fluid Flow*, vol. 8, no. 4, pp. 409–423, Jun. 1998.

[31] A. Chiba and K. Okada, “Dynamic in-plane thermal distortion analysis of an x-ray mask membrane for synchrotron radiation lithography,” *J. Vac. Sci. Technol. B Microelectron. Nanom. Struct.*, vol. 9, no. 6, p. 3275-3279, Nov. 1991.

[32] V. Nazmov, E. Reznikova, and J. Mohr, “Investigation of the radiation-induced thermal flexure of an x-ray lithography mask during a tilted exposure,” *J. Vac. Sci. Technol. B Microelectron. Nanom. Struct.*, vol. 29, no. 1, p. 011007, 2011.

[33] S. Achenbach, F. J. Pantenburg, and J. Mohr, “Numerical simulation of thermal distortions in deep and ultra deep X-ray lithography,” *Microsyst. Technol.*, vol. 9, no. 3, pp. 220–224, Jan. 2003.

[34] K. Yamazaki, “Evaluation of temperature rise and thermal distortions of x-ray mask for synchrotron radiation lithography,” *J. Vac. Sci. Technol. B Microelectron. Nanom. Struct.*, vol. 12, no. 6, p. 4028-4032, Nov. 1994.

[35] Y. Utsumi, T. Kishimoto, T. Hattori, and H. Hara, “Large area and wide dimensions X-ray lithography using energy variable synchrotron radiation,” *Microsyst. Technol.*, vol. 13, no. 5–6, pp. 417–423, 2007.

[36] Y. Vladimirsky, J. Maldonado, R. Fair, R. Acosta, O. Vladimirsky, R. Viswanathan, H. Voelker, F. Cerrina, G. M. Wells, M. Hansen, and R. Nachman, “Thermal effects in x-ray masks during synchrotron storage ring irradiation,” *J. Vac. Sci. Technol. B Microelectron. Nanom. Struct.*, vol. 7, no. 6. p. 1657, 1989.

[37] A. Ting, “Temperature rise of the silicon mask-PMMA resist assembly during LIGA exposure,” Technical Report SAND2004-4446, Sandia National Laboratory, 2004.

[38] I. A. Shareef, J. R. Maldonado, Y. Vladimirsky, and D. L. Katcoff, “Thermoelastic behavior of X-ray lithography masks during irradiation,” *IBM J. Res. Dev.*, vol. 34, no. 5, pp. 718–735, Sep. 1990.

[39] D. J. Resnick, S. V. Pendharkar, W. J. Dauksher, K. D. Cummings, M. F. Laudon, B. Romanowicz, P. Renaud, and R. L. Engelstad, “Thermal characteristics of an X-ray mask during pattern transfer,” *Microelectron. Eng.*, vol. 41–42, pp. 287–290, Mar. 1998.

[40] G. Feiertag, M. Schmidt, and A. Schmidt, “Thermoelastic deformations of masks for deep X-ray lithography,” *Microelectron. Eng.*, vol. 27, pp. 513–516, 1995.

[41] K. Marumoto, S. Aya, H. Yabe, T. Okada, and H. Sumitani, “Theoretical Analysis on Mechanical Deformation of Membrane-Based Photomask Blanks,” *Jpn. J. Appl. Phys.*, vol. 51, p. 46505, Apr. 2012.

[42] M. Karnezos, “Effects of stress on the stability of x-ray masks,” *J. Vac. Sci. Technol. B Microelectron. Nanom. Struct.*, vol. 4, no. 1986, p. 226-229, 1986.

[43] M. Laudon, A. H. Fisher, R. Engelstad, F. Cerrina, K. Cummings, W. Dauksher, D. Resnick, W. Johnson, and D. Puisto, “Prediction of in-plane distortions due to mask fabrication processes,” *Microelectron. Eng.*, vol. 35, no. 1–4, pp. 549–552, Feb. 1997.

[44] M. S. De Jong, L. O. Dallin, and R. M. Silzer, “Canadian Light Source status,” *J. Synchrotron Radiat.*, vol. 11, no. 2, pp. 214–214, Mar. 2004.

[45] S. Achenbach, V. Subramanian, D. Klymyshyn, and G. Wells, “Synchrotron laboratory for micro and nano devices: facility concept and design,” *Microsyst. Technol.*, vol. 16, no. 8–9, pp. 1293–1298, May 2010.

[46] V. Subramanian, S. Achenbach, D. Klymyshyn, G. Wells, W. Dolton, V. Nagarkal, B. Yates, C. Mullin, and M. Augustin, “In situ diagnostic capabilities for beam position and beam intensity monitoring at SyLMAND,” *Microsyst. Technol.*, vol. 16, no. 8–9, pp. 1547–1551, May 2010.

[47] A. Chiba, M. Futagami, K. Okada, and T. Kato, “Effect of Helium Gas Pressure on X-Ray Mask Heating during Synchrotron Radiation Exposure,” *Jpn. J. Appl. Phys.*, vol. 34, no. Part 1, No. 1, pp. 75–80, Jan. 1995.

[48] G. Aigeldinger, “Implementation of an Ultra Deep X-ray Lithography (UDXRL) System at CAMD,” Universität Freiburg im Breisgau, 2001.

[49] *Operating manual X-Ray Scanner DEX04*. JENOPTIK Laser, Optik, Systeme GmbH, 2007.

[50] R. Lawes, “Manufacturing costs for microsystems/MEMS using high aspect ratio microfabrication techniques,” *Microsyst. Technol.*, vol. 13, no. 1, pp. 85–95, 2007.

[51] H.-G. Woo and H. Li, *Advanced Functional Materials*. Berlin, Heidelberg: Springer Berlin Heidelberg, 2011.

[52] C.J.M. van Rijn, Ed., “Nano and Micro Engineered Membrane Technology,” in *Membrane Science and Technology*, vol. 10, Elsevier, pp. 335–346, 2004.

[53] M. E. Grady, P. H. Geubelle, and N. R. Sottos, “Interfacial adhesion of photodefinable polyimide films on passivated silicon,” *Thin Solid Films*, vol. 552, pp. 116–123, Feb. 2014.

[54] W. C. Wilson and G. M. Atkinson, “Review of Polyimides Used in the Manufacturing of Micro Systems,” Technical Report, NASA/TM-2007-214870, 2007.

[55] K. Kurabayashi, M. Asheghi, M. Touzelbaev, and K. E. Goodson, “Measurement of the thermal conductivity anisotropy in polyimide films,” *J. Microelectromechanical Syst.*, vol. 8, no. 2, pp. 180–191, Jun. 1999.

[56] G. Strobl, *The physics of polymers: Concepts for understanding their structures and behavior*. New York, NY: Springer Berlin Heidelberg, 2007.

[57] D.-J. Liaw, K.-L. Wang, Y.-C. Huang, K.-R. Lee, J.-Y. Lai, and C.-S. Ha, “Advanced polyimide materials: Syntheses, physical properties and applications,” *Prog. Polym. Sci.*, vol. 37, no. 7, pp. 907–974, Jul. 2012.

[58] L. M. Nicholson, K. S. Whitley, T. S. Gates, and J. A. Hinkley, “Influence of molecular weight on the mechanical performance of a thermoplastic glassy polyimide,” *J. Mater. Sci.*, vol. 35, no. 24, pp. 6111–6121, 2000.

[59] H. Mitsui, R. Kumazawa, T. Tanii, T. Chugun, Y. Ohsawa, T. Ozaki, and K. Takayama, “Synchrotron radiation damage test of insulating materials in the TRISTAN MR,” *Proc. Int. Conf. Part. Accel.*, vol. 52, pp. 31–44, 1993.

[60] F.-Y. Tsai, Y.-H. Kuo, and D. R. Harding, “Properties and structure of vapor-deposited polyimide upon electron-beam irradiation,” *J. Appl. Phys.*, vol. 99, no. 6, p. 64910, 2006.

[61] S. Achenbach, “Private communication.” .

[62] A. A. Harchenko, D. I. Brinkevich, S. D. Brinkevich, M. G. Lukashevich, and V. B. Odzhaev, “Radiation-induced modification of polymer surfaces,” *J. Surf. Investig. X-ray, Synchrotron*

Neutron Tech., vol. 9, no. 2, pp. 371–376, 2015.

[63] D. C. Flanders and H. Smith, "Polyimide membrane x-ray lithography masks—Fabrication and distortion measurements," *J. Vac. Sci. Technol.*, vol. 15, no. 3, p. 995, May 1978.

[64] T. Wada, S. Sakurai, and K. Kawabuchi, "Fabrication of polyimide x-ray masks with high dimensional stability," *J. Vac. Sci. Technol.*, vol. 19, no. 4, p. 1208, 1981.

[65] S. Kinuta, Y. Saita, M. Kobayashi, M. Boerner, V. Saile, and S. Hosaka, "Polyimide-based X-ray masks with advanced performance of pattern accuracy and thermal stability," *Microsyst. Technol.*, vol. 16, no. 8–9, pp. 1299–1302, May 2010.

[66] S. Achenbach, M. Boerner, S. Kinuta, W. Bacher, J. Mohr, V. Saile, and Y. Saotome, "Structure quality in deep X-ray lithography applying commercial polyimide-based masks," *Microsyst. Technol.*, vol. 13, no. 3–4, pp. 349–353, Jun. 2006.

[67] S. James and W. Alexander, *Materials Science and Engineering Handbook*, 3rd ed. Boca Raton, FL: CRC Press, 2001.

[68] Fujifilm Electronic Materials, "Durimide 7500 Technical Information." Fuji Films Electronic Materials Inc., 2012.

[69] A. A. Taylor, M. J. Cordill, L. Bowles, J. Schalko, and G. Dehm, "An elevated temperature study of a Ti adhesion layer on polyimide.," *Thin Solid Films*, vol. 531, no. C, pp. 354–361, Mar. 2013.

[70] J. Kouba, Z.-G. Ling, L. Wang, Y. M. Desta, and J. Goettert, "Fabrication of large-area x-rays masks for UDXRL on beryllium using thin film UV lithography and x-ray backside exposure," in *Micromachining and Microfabrication Process Technology*, vol. 5342, pp. 173–181, 2004.

[71] G. E. A. D. I. B. Ari and J. A. Di Bari, "Electrodeposition of nickel," in *Modern Electroplating*, 5th ed., Hoboken, N.J.: John Wiley and Sons, pp. 79–114, 2011.

[72] D. M. Allen and H. J. a Almond, "Characterisation of aqueous ferric chloride etchants used in industrial photochemical machining," *J. Mater. Process. Technol.*, vol. 149, no. 1–3, pp. 238–245, 2004.

[73] J. H. Lienhard IV and J. H. Lienhard V, *A Heat Transfer Textbook*, 4th ed. Cambridge, MA: Phlogiston Press, 2011.

[74] J. R. Howell, M. P. Menguc, and R. Siegel, *Thermal Radiation Heat Transfer*, 5th ed. Boca Raton, FL: CRC Press, 2010.

[75] A. Chiba, M. Futagami, and K. Okada, "Wafer Temperature Measurement and X-Ray Mask

Temperature Evaluation in Synchrotron Radiation Lithography," *Jpn. J. Appl. Phys.*, vol. 32, no. Part 1, No. 2, pp. 753–757, Feb. 1993.

[76] M. R. Eslami, *Finite Elements Methods in Mechanics*, vol. 216, no. 4. Springer International Publishing Switzerland, 2014.

[77] M. R. Eslami, R. B. Hetnarski, J. Ignaczak, N. Noda, N. Sumi, and Y. Tanigawa, *Theory of Elasticity and Thermal Stresses*, vol. 197. Dordrecht: Springer Netherlands, 2013.

[78] M. A. Hopcroft, W. D. Nix, and T. W. Kenny, "What is the Young's Modulus of Silicon?," *J. Microelectromechanical Syst.*, vol. 19, no. 2, pp. 229–238, Apr. 2010.

[79] H. Petersen, "The properties of helium: density, specific heats, viscosity, and thermal conductivity at pressures from 1 to 100 bar and from room temperature to about 1800 K," Danish Atomic Energy Commission, RPRT, 1970.

[80] L. M. Jiji, *Heat Convection*. New York, NY: Springer-Verlag Berlin Heidelberg, 2006.

[81] R. Barber and D. Emerson, "A numerical investigation of low Reynolds number gaseous slip flow at the entrance of circular and parallel plate micro-channels," in *Proc. ECCOMAS Computational Fluid Dynamics Conference*, Swansea, UK, September 4-7, 2001.

[82] R. W. Fox, P. J. Pritchard, and A. T. Mcdonald, *Introduction to fluid mechanics*, 6th ed. Hoboken, NJ: Wiley, 2004.

[83] ANSYS Inc., "ANSYS FLUENT theory guide," ANSYS Inc., Canonsburg, PA, 2013.